A NOVEL METHOD FOR DETECTING ECCENTRICITY IN LINE START PERMANENT MAGNET SYNCHRONOUS MOTORS

BY

IBRAHEM MAHMOUD HUSSEIN

A Thesis Presented to the
DEANSHIP OF GRADUATE STUDIES

KING FAHD UNIVERSITY OF PETROLEUM & MINERALS
DHAHRAN, SAUDI ARABIA

In Partial Fulfillment of the
Requirements for the Degree of

MASTER OF SCIENCE
In

ELECTRICAL ENGINEERING

JANUARY 2017

KING FAHD UNIVERSITY OF PETROLEUM & MINERALS
DHAHRAN- 31261, SAUDI ARABIA

DEANSHIP OF GRADUATE STUDIES

This thesis, written by **Ibrahem Mahmoud Hussein** under the direction his thesis advisor and approved by his thesis committee, has been presented and accepted by the Dean of Graduate Studies, in partial fulfillment of the requirements for the degree of **MASTER OF SCIENCE IN ELECTRICAL ENGINEERING.**

Dr. Zakariya Al-Hamouz
(Advisor)

Dr. Ali Al-Shaikhi
Department Chairman

Dr. Mohammed Abido
(Member)

Dr. Salam A. Zummo
Dean of Graduate Studies

Dr. Mohammed AlMuhaini
(Member)

24/1/17
Date

© IBRAHEM MAHMOUD HUSSEIN

2017

Dedicated

To

My Parents Another Time

And More Than Any Time

ACKNOWLEDGMENTS

All praise and glory to Allah the most merciful, the most beneficent, who gave me the health, strength, and courage to complete my Master's degree.

I would like to express my deep appreciation to my advisor Prof. Zakariya Al-Hamouz for giving me the opportunity to become one of his students. I thank him for his efficient and constant support, help, motivation, and immense knowledge. His precious advice and thorough guidance played a critical role in the completion of this thesis.

I also would like to extend my appreciation to my dissertation committee members Prof. Mohammed Abido and Dr. Mohammed AlMuhaini for their insightful comments, support, and profitable questions which incented me to enhance my work.

I would like to thank our research group members supervised by Prof. Zakariya Al-Hamouz, they include Mr. Abdul-Aziz Melhim for his guidance in performing the FEM simulation, Luqman Marraba, and Khalid Baradiah, to whom I would like to extend my appreciation for their support and assistance.

I am thankful to the King Fahd University of Petroleum and Minerals (KFUPM) for providing me with the research facilities, precious resources, financial support, and an environment conducive to intellectual growth for my master research.

I would like to thank many other people from KFUPM who have made my years unforgettable and cherished. They include Dr. Shadi Al-Omari, Bashar Khatib, Ahmad

Shaheen, Mohammed Qannan, and Salem Jaradat. I would like to thank these individuals for their friendship and motivation.

Finally, I would like to thank those with whom I have a much deeper relationship. Among them are my parents Mahmoud and Nada Hussein, who brought me up and supported me throughout my education. I also wish to thank my siblings in Palestine and Jordan for sincerely caring about my well-being and for their love and affection.

TABLE OF CONTENTS

LIST OF TABLES

LIST OF FIGURES

LIST OF ABBREVIATIONS

ANNs : Artificial Neural Networks

FEA : Finite Element Analysis

FEM : Finite Element Method

FFNN : Feedforward neural network

ICCG : incomplete Cholesky conjugate gradient

IVS : Input variable selection

LSPMS : Line Start Permanent Magnet Synchronous

MCSA : Motor Current Signature Analysis

MMF : Magnetomotive Force

MSE : Mean square error

MWFM : Modified Winding Function Method

NMSE : Normalized mean square error

PCA : Principle component analysis

PCs : Principle components

PM : Permanent Magnets

PMSM : Permanent Magnet Synchronous Motor

RMS : Root mean square error

SE : Static Eccentricity

WFM : Winding Function Method

NOMENCLATURE

C : Covariance matrix

F : Activation function

$g(\phi)$: Airgap function

$g^{-1}(\phi)$: Inverse airgap function

g_0 : Airgap length

H : Magnetic field intensity

i_A : Current in coil A

i_d : Direct current

$i_{r,abc}$: Rotor circuit currents per each phase

$i_{r,qd0}$: Rotor circuit currents in qd0 reference frame

$i_{s,abc}$: Stator circuit currents per each phase

$i_{s,qd0}$: Stator circuit currents in qd0 reference frame

i_q : Quadrature current

J : Motor inertia

K_s : Park transformation matrix

K_r : Clark transformation matrix

l : Motor stack length

l_{ls} : Stator winding leakage inductance

l_{lr} : Rotor winding leakage inductance

L_{rr} : Rotor winding self-inductance

L_{rs} : Rotor to stator mutual inductance

L_s	:	Stator winding self-inductance
L_{sr}	:	Stator to rotor mutual inductance
$L_{r,qd0}$	:	Rotor winding self-inductance in qd0 reference frame
$L_{rs,qd0}$	:	Rotor to stator mutual inductance in qd0 reference frame
$L_{s,qd0}$	:	Stator winding self-inductance in qd0 reference frame
$L_{sr,qd0}$	:	Stator to rotor mutual inductance in qd0 reference frame
N	:	Number of samples or operating conditions
N_s	:	Number of stator winding turns
N_r	:	Number of rotor winding turns
N_e	:	Number of equivalent winding turns
$N(\phi)$	:	The winding function
$n(\phi)$	:	The turn function
O	:	Motor center of symmetry
O'	:	Motor center of rotation
p	:	The permeance in flux path
P	:	Number of poles
P_p	:	Number of pole pairs
RSSQ	:	The root sum of squares level
R_s	:	Radius of stator inner race
r	:	Average radius of the motor airgap
S	:	Total number of correct predicted output by neural network
T_{damp}	:	Damping torque

T_{em}	:	The developed electromechanical torque
T_{mech}	:	Input load torque
$V_{r,abc}$	:	Rotor circuit terminal voltages
$V_{r,qd0}$	:	Rotor circuit terminal voltages in qd0 reference frame
$V_{s,abc}$	:	Stator terminal voltages
$V_{s,qd0}$	:	Stator circuit terminal voltages in qd0 reference frame
w	:	The window matrix
ω	:	Angular speed
ω_r	:	Rotor angular speed
X	:	The input variable
X_{En}	:	The energy row vector
X_i	:	The row data of stator current
X_k	:	The kurtosis row vector
X_{mean}	:	The mean row vector
X_{RSSQ}	:	The root sum of squares level row vector
X_{RMS}	:	The root mean square row vector
X_V	:	The variance row vector
X_{SV}	:	The statistical feature vector
X_{pc}	:	The 1st principle component vector
y	:	The desired output in training process
y'	:	The predicted output in training process
$\lambda_{r,abc}$	:	Flux linkage of rotor windings

$\lambda_{r,qd0}$	:	Flux linkage of rotor windings in qd0 reference frame
$\lambda_{s,abc}$	:	Flux linkage of stator windings
$\lambda_{s,qd0}$	:	Flux linkage of stator windings in qd0 reference frame
λ_m	:	Peak magnetic flux of the permanent magnets
$\lambda_{r,pm}$	:	Rotor permanent magnets flux components
$\lambda_{s,pm}$	:	Stator permanent magnets flux components
λ_d	:	Direct axis flux linkage
λ_q	:	Quadrature axis flux linkage
δ_s	:	Degree of static eccentricity
δ_s'	:	Degree of static eccentricity estimated by neural network
ϕ	:	Spatial reference angle form (as) stator winding axis
θ_0	:	Angle of static eccentricity vector

ABSTRACT

Full Name : IBRAHEM MAHMOUD HUSSEIN
Thesis Title : A NOVEL METHOD FOR DETECTING ECCENTRICITY IN LINE START PERMANENT MAGNET SYNCHRONOUS MOTORS
Major Field : Electrical Engineering
Date of Degree : January 2017

Electric motor failure is an important issue addressed by many researchers. The major role of electrical motors in industrial, commercial, and residential sectors raises the importance of investigating their behavior under different operating conditions. A recently developed and manufactured motor, which is commonly used in industrial applications, is the line start permanent magnet synchronous (LSPMS) motor. This motor has a self-starting capability, the ability to reach a synchronous speed, and a premium efficiency. LSPMS motors have been widely studied under normal operating conditions. However, under different kinds of faults such as eccentricity, broken bars, demagnetization, etc., investigations are still premature. Eccentricity faults are attributed to many reasons such as overloading, overstress in thermal and pressure circumstances, rotor misalignments, and bearing faults, which will result in motor shaft vibration and acoustic noise, which could completely damage the motor. This work is devoted to developing a mathematical model of the LSPMS motor under healthy and static eccentricity fault conditions. Besides, this thesis will propose a detection technique for static eccentricity fault condition based on motor current signature analysis and the artificial neural network (ANN).

The developed mathematical concept is based on the coupled magnetic circuit approach and the modified winding function method; the model will be simulated using MATLAB^{TM}

under healthy and different static eccentricity fault conditions. Finite element analysis will be conducted to verify the developed mathematical model results using JMAG^{TM}. Results show that the effects of static eccentricity on the stator current depend on the degree of static eccentricity and the angle of static eccentricity vector, which will affect the motor synchronization time and the time variation of stator current. Besides, the finite element method (FEM) results confirm the developed mathematical model results under the healthy and static eccentricity conditions. Furthermore, the neural network based detection method is able to detect a static eccentricity fault under different operating conditions with an accuracy between 96.87% and 98.75 %, with under 10% and 20% error between the actual and predicted degree of static eccentricity using ANN.

ملخص الرسالة

الاسم الكامل :ابراهيم محمود حسين

عنوان الرسالة :طريقة جديدة للكشف عن الاختلاف المركزي في المحركات التزامنية ذات المغناطيس الدائم

التخصص :الهندسة الكهربائية

تاريخ الدرجة العلمية: كانون الثاني 2017

ان الاعطال في المحركات الكهربائية هي قضية مهمة وقد تم تناولها من قبل العديد من الباحثين. فالدور المهم التي تلعبه المحركات الكهربائية في القطاعات الصناعية والتجارية والسكنية تزيد من أهيمه دراستها تحت الظروف المختلفة للتشغيل. أحد المحركات حديثي التصنيع والتطوير هو المحرك التزامني دائم المغناطيسية الذي يعمل من مصدر الجهد مباشرة. يتمتع هذا المحرك بقدرته الذاتية على الحركة عند التشغيل، وعلى مقدرته للوصول للسرعة التزامنية، ويتمتع ايضا بكفاءة استثنائية. لقد تم دراسة هذه المحركات تحت الظروف الطبيعية للتشغيل. غير ان دراستها تحت ظروف مثل الاختلاف المركزي (Eccentricity), والقضبان التالفة, و فقدان المغناطيسية لا تزل غير مكتملة. ان اسباب حدوث الاختلاف المركزي متعددة، مثل الحمل او الضغط الزائد على المحرك، او حدوث خلل في حوامل المحرك والتي تؤدي الى انحناءات في الجزء الدوار. وهذا يؤدي الى اهتزاز المحرك، وصدور اصوات مثل الضجيج، وممكن ان يؤدي الى تلف المحرك تماما. لقد كرست هذه الاطروحة لتطوير نموذج رياضي لهذا المحرك تحت الظروف الطبيعية وفي حالة الاختلاف المركزي الثابت. أن استخدام طرق التشخيص والكشف عن هذا الخلل يخفف من حدته. هذا الاطروحة سوف تقترح طريقة للكشف عن هذا الخلل باستخدام بصمات التيار الذي يقوم المحرك باستخدامه والشبكة العصبية الاصطناعية (الذكاء الصناعي). ان النموذج الرياضي المطور للاختلاف المركزي الثابت يعتمد على مبدأ الدوائر المغناطيسية وعلى طريقة (MWFM). ستتم محاكات النموذج باستخدام برنامج (MATLAB^{TM}). لعملية التحقق من النموذج الرياضي المقترح، فقد تم استخدام طريقة العناصر المنتهية باستخدام برنامج (JMAG^{TM}). تشير النتائج الى ان الانحراف المعياري الثابت يؤثر على قيمة تيار المحرك خلال الزمن ويعتمد هذا التأثير على درجة الانحراف المعياري الثابت، وقيمة الزاوية الخاصة به. لقد تم التحقق من نتائج النموذج الرياضي باستخدام طريقة العناصر المنتهية تحت الظروف الطبيعية للتشغيل واثناء حدوث العطل. بالإضافة الى ذلك، فان طريقة الشبكة العصبية قادرة على كشف حدوث الانحراف المعياري الثابت تحت الظروف المختلفة بدقة تراوحت ما بين 96.87 بالمئة الى 98.75 بالمئة بنسبة خطأ ما بين 10 بالمئة الى 20 بالمئة بين القيمة الحقيقية لانحراف المعياري الثابت والقيمة التقديرية باستخدام الشبكة العصبية.

CHAPTER ONE

INTRODUCTION

1.1 Overview

Electrical motors are the actuators of our lives. Their application is central to many of our daily activities and they are primarily used at industrial, commercial, and residential levels. Statistics show that electrical motors consume about two-thirds of the total industrial power consumption in each society [1], with the majority of the developing countries moving toward similar industrialization. Therefore, there will soon be an increase in the demand for more efficient and robust electric motors.

Induction motors constitute by far the largest portion of electrical motors in the market. However, more efficient motors are beginning to appear as other alternatives. A recently manufactured motor, which is used in industrial practices, is the Line-Start Permanent Magnet Synchronous (LSPMS) motor [2]. This motor has many desirable features which open the door for greater penetration in the market. This motor enjoys a much higher efficiency than the induction motor for the same power rating. Induction motors suffer from low power factors due to their inductive behavior, which will be proportional to the losses in turn. In contrast, LSPMS motors operate with a higher power factor than the induction motor, which will thus increase efficiency and reduce the total losses.

Regarding the motor torque of the LSPMS motor, the permanent magnet motors are superior to other motors in term of their total output torque and power density. Another special attribute of the LSPMS motor is the lower operating rotor temperature, which is about 30% lower than induction motors. The more recent motor has a higher rotor temperature due to the rotor’s winding losses, whereas the LSPMS motor has a high reduction in rotor losses as it operates at a synchronous speed [3].

In general, the LSPMS motor has a complex design. Therefore, special concerns should be made for proper operation in order to maintain continuity in the system. Furthermore, any failure during motor operation can lead to considerable consequences, such as shutting down a plant or production line. Early detection of such failures could prevent complete damage of the motor. This will provide an aid to protect the motor and isolate the fault. Most of the online monitoring and fault diagnostic techniques were applied to the induction motors. Regarding faults, the LSPMS motor is among a number of motors that have not been sufficiently explored [4].

1.2 General Background

Electrical motors consist of many parts, which are mainly electrical and mechanical, such as stator and rotor winding, rotor bars or damper windings, bearings, and rotor magnets in the PMSM and LSPMS motors. Those parts are exposed to failure due to many reasons [5], for example:

1. Motor operation extending beyond the motor lifetime.
2. Wrong rated power, voltage or current.
3. Improper feeding source.
4. Mistakes during repair.
5. Non-ideal operational environment such as dust, vibrations, high temperature, etc.

1.2.1 Faults Classification in Electrical Motors

As previously mentioned, those faults are usually categorized to mechanical and electrical faults. Figure 1.1 classifies these faults per each category.

Among those faults, 40% of faults are related to bearing damage, 38% are stator related faults, 10 % are rotor related faults, and 12% are external and other faults [6]. Usually, electrical motors have some electrical and mechanical symmetry, such as the symmetric shape of the rotor and stator configurations. However, faults will affect motor operation, as well as the symmetry. There are many indices created by faults which indicate abnormal operation, such as [5]:

1. Mechanical vibrations.
2. Speed variations.
3. Line currents variations.
4. Acoustic noise.
5. Irregular air gap shape.
6. Increment in motor temperature.

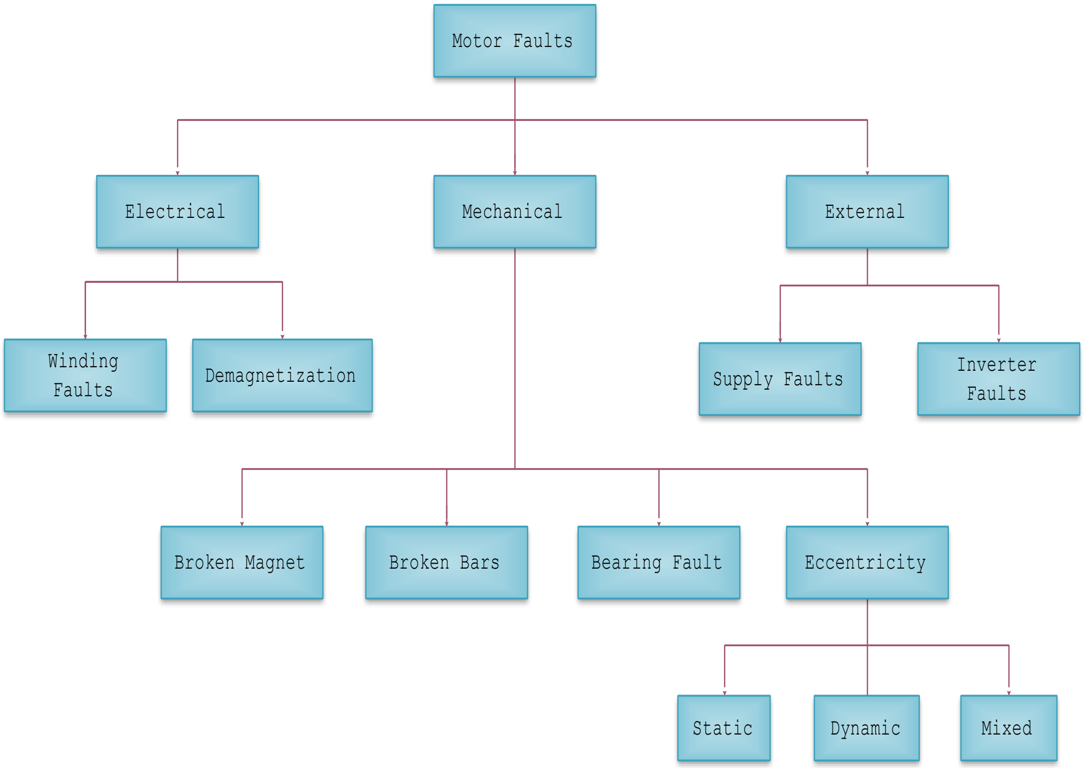

Figure 1.1: Fault classifications in electrical motors.

1.2.2 Fault Diagnostic Techniques

Motor faults usually have a specific pattern to recognize the fault occurrence, such as Line current frequency symptoms, duration, and amplitude variations. Those indices or patterns can reveal the fault type and its severity. Many algorithms have been developed and improved to enhance those indices, and many of them are used in the industrial market. For example, eccentricity faults in induction motors can be detected by frequency analysis of stator current. This process is called motor current signature analysis (MCSA) [7].

Fault diagnostic techniques can be classified into four main categories, as shown in Figure 1.2 [5].

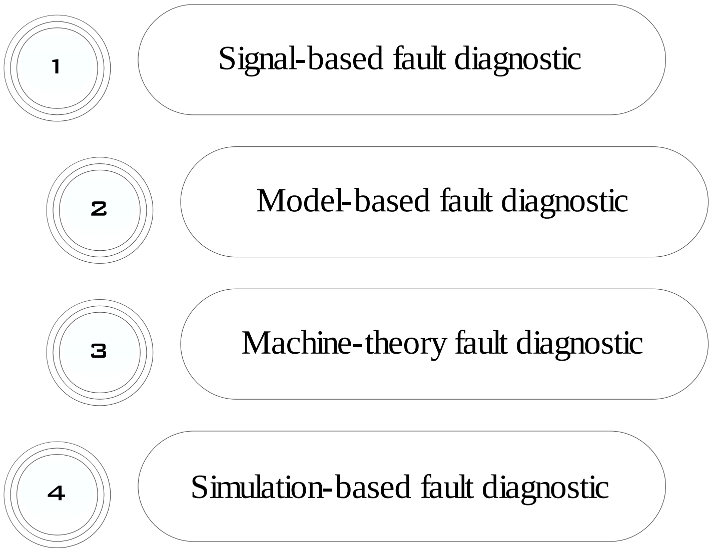

Figure 1.2: Fault diagnostic techniques

Signal–based fault analysis includes MCSA, mechanical vibration signal analysis, temperature measurement, acoustic noise analysis, and instantaneous output power variation analysis. Model-based fault analysis incorporates artificial intelligence methods, such as using a neural network for detection purposes. In the machine theory–based analysis, it is implemented using the winding function method (WFM), the modified winding function method (MWFM), and magnetic equivalent circuits. Finally, simulation-based analysis depends on simulating the actual model geometry, such as finite element analysis (FEA). The diagnosis process is expected to provide early information about the fault occurrence. This will assist the process of fault isolation, which in turn reduces its severity. In addition, this information will be helpful in the process of preventive maintenance for future planning.

The mechanism of fault diagnosis can be summarized in Figure 1.3. The fault detection scheme is performed based on time or frequency domain analysis. The fault decision stage is encountered to identify any failure during normal operation; at this stage, the fault severity is specified. Next, a feedback signal will be delivered to the motor controller to decide the motor state.

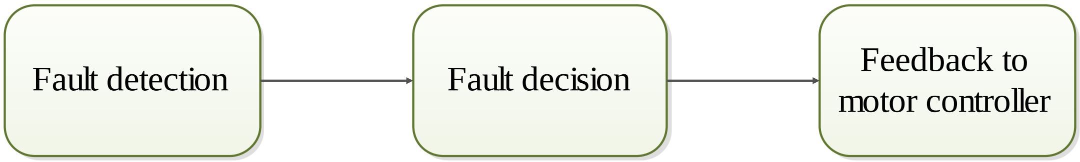

Figure 1.3: Fault diagnostic Stages

1.3 Thesis Motivation

As mentioned earlier, no reported work has been done on the modeling of static eccentricity fault conditions in LSPMS motors. Thus, the motivation behind investigating this fault became essential and can be summarized in the following points:

- LSPMS motors experience different kinds of faults, including static eccentricity, which can result in complete damage to this motor.
- The proposed mathematical model under faulty conditions will assist the process of online fault detection in a faster manner. FEA requires extensive simulation time, a detailed geometric model, and computational analysis.
- The proposed detection scheme, which is based on the neural network, will provide a robust detection tool independent of motor construction, and less sensitive to any change in the motor parameters.

1.4 Thesis Objectives

The main objective of this thesis work is to investigate the operation of the LSPMS motor in healthy and under static eccentricity fault conditions. In addition, this thesis will propose a diagnostic tool for the online monitoring of motor operations. The specific objectives are:

1. Derive a mathematical model for healthy and static eccentricity fault conditions in the LSPMS motor.
2. Building a SIMULINK^{TM} model to investigate the performance of the LSPMS motor under different loading conditions for both healthy and faulty cases.
3. Perform a finite element simulation of healthy and faulty motors under different loading conditions.
4. Propose a diagnostic tool for online early warning of LSPMS motors under static eccentricity fault conditions.

1.5 Thesis Organization

Besides the introduction, this thesis comprises another five chapters. Chapter two introduces a comprehensive literature review, which covers the faults in electrical motors and emphasizes the eccentricity fault and its diagnostic methods. The MWFM and the mathematical modeling of the LSPMS motor are covered in chapter three under both healthy and faulty conditions. Chapter four depicts the analysis and simulation of the LSPMS motor using JMAG^{TM} FEM software. In addition, a discussion and comparison with the developed mathematical model are conducted. The proposed detection scheme of static eccentricity is shown in chapter five. Finally, chapter six presents the conclusions and recommendations regarding future works.

CHAPTER TWO

LITERATURE REVIEW

2.1 LSPMS Motor under Healthy Condition

Under normal operating conditions, a great deal of research work has investigated the LSPMS motor in terms of modeling, efficiency, and energy consumption [3]. The researcher also presents the challenges faced by this motor, such as the breaking torque and construction cost [8]. However, this motor has many desirable features. It was shown that this motor enjoys a higher efficiency than induction motors, which in turn reflected on the energy and money saving benefits [9],[2].

H. Behbahanifard et al. [10] introduced a comprehensive survey of the work done on the modeling trends of healthy LSPMS motor, which includes the initial start and synchronization process, cogging torque, and the armature reaction during the starting process, which results in permanent magnet demagnetization.

Solmaz Kahourzade et al. [11] focused on modeling with more emphasis on the dynamic and steady state behavior of the motor. They proposed an optimization algorithm in regards to the rotor bar's resistance to the smooth line starting capability and increased motor efficiency. Experimental results were used to verify the simulation results of the proposed model. This paper compared the LSPMS motor (3-phase, 4-pole, 2kW) with a similar rating induction motor. It was found that the LSPMS motor had higher efficiency and can withstand overload conditions more than the induction motors. Besides, the starting current for the LSPMS motor is lower than the induction motor at the same load condition. On the same manner, a high performance LSPMS motor model was developed from an existing induction motor model [2]. The verification of this new model was performed using a finite element analysis, and a significant improvement was gained in power factor and efficiency.

Xiaozhuo Xu et al. [12] introduced a novel LSPMS motor rotor structure. The analysis was conducted by building a finite element model to simulate the motor performance. The simulation results were verified by experimental findings. They designed a new magnet topology to get improved electromagnetic torque characteristic at starting. They also provide the lowest input voltage needed to start the motor. In addition, the influence of winding turns, airgap variation, and height of permanent magnets were investigated. As the winding turns per phase were increased, the motor torque and starting current was reduced. The airgap length reduces the power factor of the motor as the gap length increased. The investigated magnets topology of the rotor in [11], which is in a V-shape, differs from the rotor structure in [12].

Dan Stoia et al. [13] propose an analytical method to analyze a LSPMS motor based on a magnetic equivalent circuit and a dynamical qd0 reference frame model. This paper provides the needed equations for proper design of the LSPMS motors. The operating point of the permanent magnet was determined analytically, considering the armature reaction effect. Besides, the synchronous and asynchronous operating conditions were considered to develop the electromagnetic torque expression of the motor. Besides, this paper depends on the magnetic equivalent circuit approach to developing the motor characteristic equations. However, reference [11] and [12] analyzed the performance of the LSPMS motor based on the FEM results.

The authors in [14] and [15] performed a single phase analysis on the LSPMS motor along with finite element analysis and experimental verification. In [14], an accurate prediction of starting torque is made using the average expected electromagnetic torque and the envelope of the pulsating torque. In [15], a unified analysis of an interior permanent magnet motor, which leads to the determination of steady state, transient, and dynamic performances, is presented.

2.2 Faults in Electrical Motors

This section will introduce a brief review about the faults mentioned in chapter one. Eccentricity faults will be covered in section 2.3.

2.2.1 Bearing Fault

The bearing fault is responsible for about 40% of total electrical motor failures. Usually, motors operate under non-ideal conditions such as vibration and dust contaminations. Figure 2.1 indicates the geometry of a typical bearing cross-sectional area. Bearings, in general, consist of inner and outer races surrounding the balls. With the aid of non-ideal conditions, bearing defects can be spread and result in significant failure in the bearing races. This will generate mechanical vibrations in addition to acoustic noise [16].

Moreover, vibrations can be characterized as a slight movement of the rotor in the airgap, which results in a non-uniform airgap shape. In other words, this will generate instantaneous eccentricity, as will be discussed later.

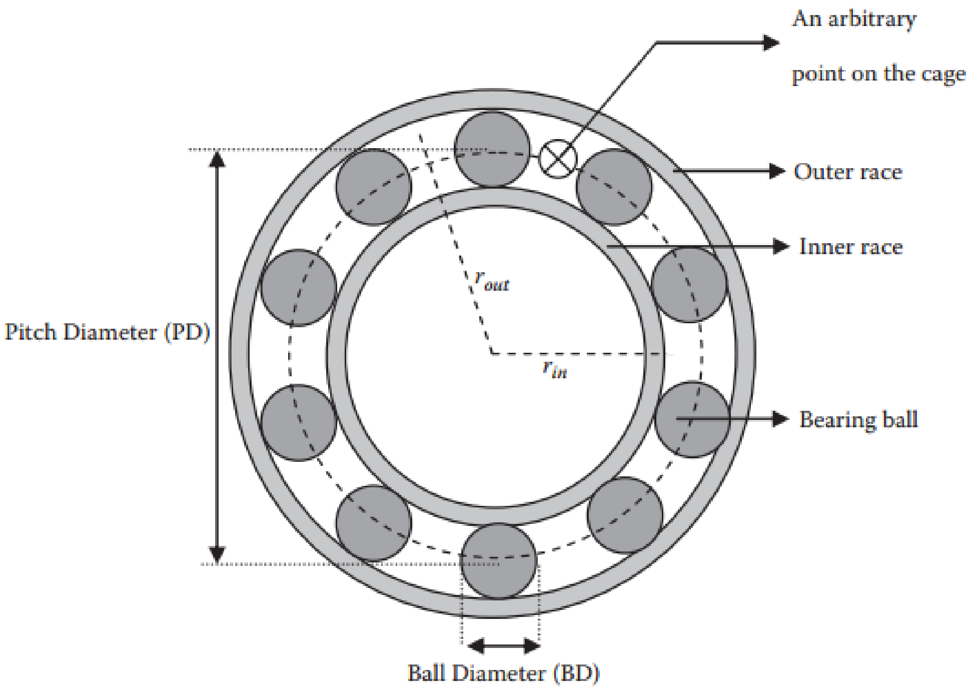

Figure 2.1: Bearing geometry [5]**.**

2.2.2 Winding Faults

Stator faults are responsible for about 30% to 40% of the total electrical motor faults. These faults are either from stator or rotor winding, as well as lamination defects. Inter-turn faults could happen through the stator winding and will result in considerable effects on machine performance and the output torque [5].

2.2.3 Broken Rotor Bars

Induction motors have bars installed in the rotor. Broken rotor bars are responsible for about 5% of the total faults. Figure 2.2 (a) indicates healthy rotor bars geometry. The rotor consists of bars shortened by end rings to allow a circulating current, which will result in the force applied to the rotor bars.

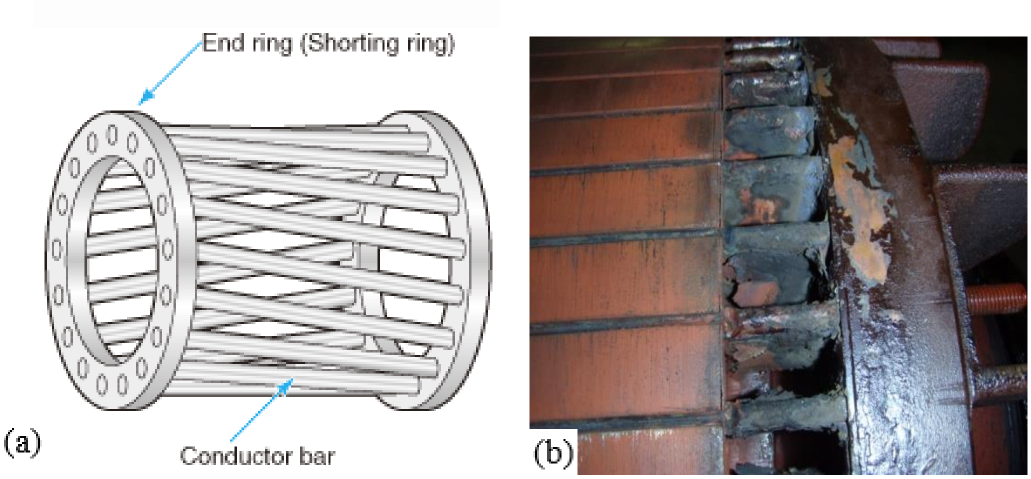

Figure 2.2: (a) Healthy rotor bars, (b) Broken rotor bars [17]

On the other hand, Figure 2.2 (b) indicates broken rotor bars. The rotor broken bar fault will result in unbalanced current flow through the rotor bars. Unbalanced current will result in pulsating torque and reduce the average torque of the motor.

2.2.4 Demagnetization Fault

Due to the construction of synchronous motors, more faults are likely to occur, such as damper winding faults, rotor winding faults, and demagnetization in both the LSPMS motor and PMSM.

Synchronous motors have damper windings, which are similar to the bars installed in the rotor of induction motors. However, the rotor has also contained field circuit which pulls the motor into synchronism in a steady state. The motor will start like an induction motor; when the speed reaches a near synchronous speed, the field circuit, which is excited by direct current (DC) source, is turned on and this will lock up the stator rotating magnetic field with the rotor magnetic field [18].

In PMSM, the field circuit is replaced with a permanent magnet, but without damper winding. In this case, the motor needs a drive circuit for starting purposes. However, in LSPMS motors, this issue is solved. A modified version of PMSM with installed rotor bars will enable the motor to have the self-start capability in the same way as induction motors. Moreover, the permanent magnets will help the motor to be synchronized when the rotor speed is near the synchronous speed [19].

For LSPMS motors and PMSMs, demagnetization faults are mainly due to the armature reaction effect or broken magnets. As discussed before, during starting the motor, the stator rotating magnetic field, together with the rotor bars, will assist the self-starting capability. However, the stator flux will oppose the magnetic remanence of the permanent magnet installed in the rotor. With this phenomenon, repeated each time the motor starts, the remanence of the permanent magnet will be decreased. This fault can result in partial or complete failure of magnets [20].

2.3 Eccentricity Faults in Electrical Motors

Eccentricity related faults are responsible for about 5% to 15 % of the total faults. This fault happens when there is a non-uniform distance between stator inner race and rotor outer race, which in turn will result in an unbalance magnetic field in the airgap. The unbalanced magnetic flux will lead to having a non-uniform flux linking both the stator and rotor circuits. This will affect mainly the motor inductances due to the non-uniform air gap distance. Moreover, the synchronization process and time variation of the stator current will be affected. There will be an injection of harmonics in the stator line current [21].

There are three types of eccentricity that can occur in electrical motors: the first type is static eccentricity, and the second one is dynamic eccentricity. The combination of both static and dynamic eccentricities is called mixed eccentricity, which implements the third type.

2.3.1 Static Eccentricity Fault

Static eccentricity occurs when the rotor is at a constant offset from the stator symmetry axis and rotates about the new center of rotation, which has a specific offset from stator center. Thus, the minimum air gap distance is constant. However, the motor rotor is rotating at another center rather than the symmetry center. [22]

Figure 2.3 presents a comparison between the rotor position in the healthy and faulty motor. The rotor position is shifted by specified distance from the origin center of stator and rotor. According to [23], static eccentricity can happen due to one of the following reasons:

1. Wrong placement of rotor or stator in the manufacturing process.
2. Incorrect bearing position and housing imperfection.
3. Bearing deterioration.
4. Shaft deflection and rotor overweight.

This will result in the deterioration of rotor, stator core, and stator winding. In addition, bearing failure, vibration, noise, and bending of the rotor shaft will happen.

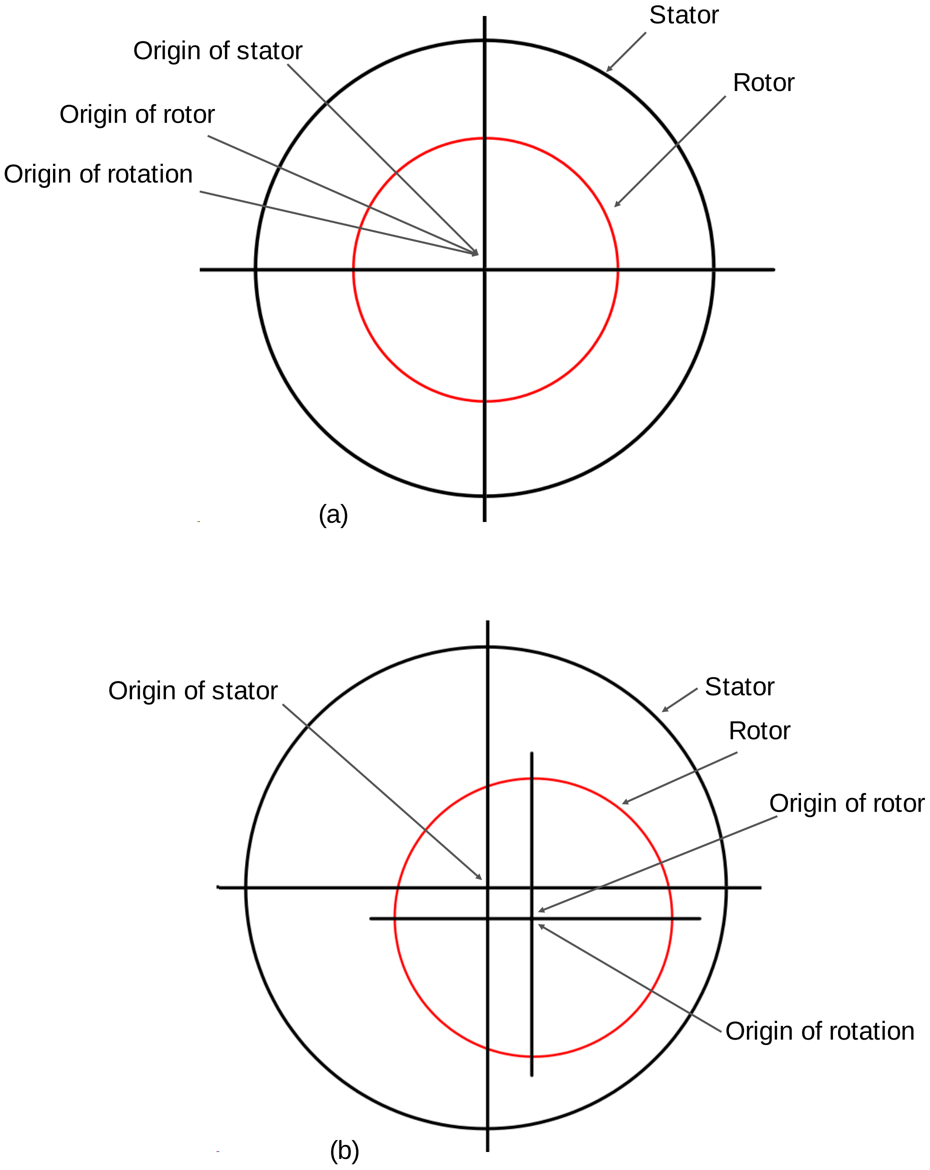

Figure 2.3: Comparison of the motor geometry under (a) healthy and (b) static eccentricity fault.

2.3.2 Dynamic and Mixed Eccentricity Faults

In a dynamic eccentricity fault, the minimum air gap distance revolves with the rotor rotational axis. Thus, the rotational axis of dynamic eccentricity is the center of stator.

However, the rotor itself is shifted from its symmetrical axis. This will result in a variable distance in the airgap [24]. Figure 2.4 describes this process.

The combination of static and dynamic eccentricity results in mixed eccentricity. The rotational axis is neither in the stator center nor along specific offset, rather, it is positioned between the rotor offset and stator center

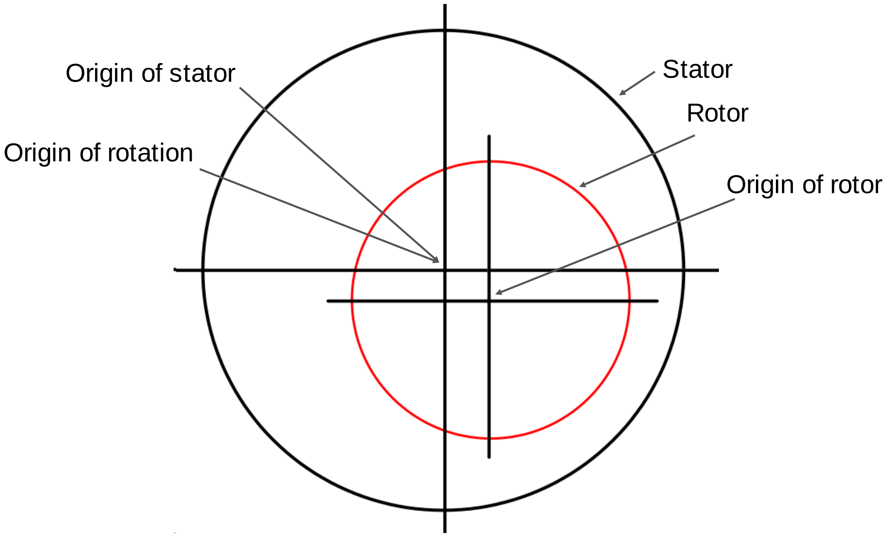

Figure 2.4: Motor geometry under dynamical eccentricity.

2.4 Diagnostic Techniques of Eccentricity Fault

The analysis of electric motors depends on obtaining the electromagnetic field distribution at every point through the motor construction and especially in the air gap. The exact electromagnetic distribution can be obtained by using electromagnetic equations, for example, FEM, which usually arrives with the solution of either Laplace or passion equations. On the other hand, the coupled magnetic circuit approach can be used to represent the motor model by a set of differential equations relating to the motor resistance and inductance matrices [25].

Various methods were presented in the literature for modeling and simulating eccentricity faults. They are based on the finite element analysis method or coupled magnetic circuit approach and the MWFM. As mentioned before, FEM is considered one of the most accurate methods to simulate the motor behavior [26]–[29]. However, it requires a knowledge of detailed motor parameters in addition to the internal construction of the motor to represent the geometry model. This method is a time-consuming process, even for a powerful computer, and will not provide as simple analytical modeling expressions as the later method [30]. On the other hand, the MWFM can be used to calculate the motor inductances under the static eccentricity fault to represent the non-uniform airgap [31]. Moreover, the results obtained from the MWFM are verified using the finite element method for validation purposes.

The MWFM depends on the winding configuration and the positional relationship of the stator and rotor coils along with the physical motor dimensions. It is based on the Ampere and Gauss laws that drive the various motor inductances, which include the effect of space harmonics [32]. The MWFM is widely introduced to simulate and model electrical motors both in healthy and under internal motor fault conditions in both synchronous and induction machines. It is utilized for the first time in [33] for internal winding fault analysis and consequently in [34], [35] for rotor faults.

2.4.1 Winding Function Method in Induction Motors

LSPMS motors behave like induction motors in the starting process and operate in a steady state as the synchronous motors. Therefore, it is important to review the methods of eccentricity modeling, both in induction and synchronous motors.

In [36], Hamdani et al. introduced an analytical evaluation method for calculating induction motor inductances under dynamic eccentricity using the modified winding function and finite element methods. They introduced an analytical expression for self and mutual inductances under this fault. The results obtained by the analytical method were compared to these results, which were determined by the finite element method, with a satisfactory match found between them. It was found that the amplitude of the motor inductances increased under the fault condition and the self and mutual inductance of stator became function of rotor position. In the same manner as depicted in [37], the analysis to static and dynamic eccentricity are performed. The equations of inductance are developed based on MWFM. Moreover, this study is extended in [38] to include the skew effect. Consequently, the author of [39] presented the technique of the modified winding function method for modeling the dynamic eccentricity fault in induction motors. The stator current signature was used to detect the fault, and the followed methodology is used to derive an analytical expression for the stator current. This current signature can be used to get the frequency components of the dynamic eccentricity fault.

Subhasis Nandi et al. [40] modeled the mixed eccentricity in three phase induction motors based on the modified winding function method along with the finite element analysis to compute the motor inductances. Frequency analysis of stator current is utilized as a detection scheme. The simulation results show all the expected low and high frequency harmonics presented under mixed eccentricity fault conditions. The same methodology was followed in [41] by performing a dynamical simulation to the induction motor under the mixed eccentricity fault. The results show the current signature as well as the frequency spectra under healthy and faulty conditions. A FEM simulation is performed to confirm simulation results. In addition, the results investigate the inductance characteristic in the case of static and dynamic eccentricities. In [42], the authors present a close form expression for calculating the inductance matrices in induction motors under eccentricity conditions. In addition, a new technique based on the winding function method is proposed to model the eccentricity. This paper uses additional Fourier terms in the inverse airgap function to enhance the simulation results. Also, frequency analysis was used to detect the fault condition.

Hamid A.Toliyat et al. [21] introduced the modified winding function method to present a new model of the induction motor under airgap eccentricity. The authors developed the mathematical model based on the magnetically coupled circuit approach, and represent the eccentricity by modifying the inductance matrices of the motor. In the same manner, Long Wu et al. [43] used the same principle in separating the load oscillation and rotor fault effects in the stator current based on MWFM.

In [44], the authors developed a diagnostic technique to isolate the eccentricity fault in a close-loop control system for doubly-fed induction motor. The inductance matrices were derived under healthy, static and dynamic eccentricity conditions based on the modified winding function method. The same principle was used in [45] to perform a dynamic simulation of a dynamic eccentricity fault in induction motors. This paper started from developing the healthy mathematical model, modeling the dynamic eccentricity and simulate the motor performance. The simulation results were compared with an experimental setup and were found to be in fine agreement with each other.

Regarding the axial eccentricity, the authors of [46] propose a method to derive the induction motor inductance in analytical fashion under rotor misalignment fault. The proposed method has been compared with MWFM. The results are confirmed experimentally. Moreover, reference [47], [48] investigate a squirrel cage induction motor inductance calculation under an axial eccentricity fault; the radial eccentricity case is also taken into consideration. The stator and rotor skewing effect is also considered. The authors propose a geometrical method for inductance calculation using 2D-MWFM. In the same manner, reference [49] presents an inductance evaluation of a squirrel-cage induction machine based on MWFM for curved dynamic eccentricity. The same concept was followed in [50], where a 2D-MWFM has been used to simulate an eccentricity fault in the case of static eccentricity with and without axial alignment. This paper provides an analytical expression for calculating machine inductances in compact form.

In [51], airgap eccentricity in a three phase induction motor was investigated using a complex apparent power signature analysis. Eccentricity modeling was performed using MWFM, and a fault detection scheme was implemented based on the motor apparent power signature. The author supports the simulation result by using an experimental test setup to compare it with the simulated one.

In [52], Ahmad et al. presents the induction motor dynamical model under stator and rotor faults based on winding function method. The simulation process is performed in steady state and transient period. The analysis is confirmed by frequency analysis of stator current.

Finally, the winding function method is also used for unbalancing the supply conditions in the induction motors using MATLAB®. Motor dynamics such as speed, torque, and phase current are investigated for fault diagnosis and detection [53].

2.4.2 Winding Function Method in Synchronous Motors

Eccentricity analysis in synchronous machines is similar to the induction machines. However, synchronous machines have many types, topologies, and designs. For example, there are the salient and non-salient pole machines, they may contain a DC power source for field excitation or having a permanent magnet attached to their rotors as in the case of LSPMS motor and PMSM.

The authors in [54] present a new index for detecting the dynamic eccentricity based on the modified winding function method in the round rotor synchronous motors. This index is based on processing the developed torque using the time series data mining (TSDM) method. The authors also investigate the load variation in [55] under eccentricity conditions. The authors showed that the load variation has no impact on the amplitude of stator current harmonics since the motor is running at a constant speed. The same approach was used in [56] to present a novel method for modeling dynamic eccentricity in salient-pole synchronous motors. The coupled magnetic circuit approach has been used for simulating this fault. The main key for this simulation is to determine the machine inductances under healthy and faulty cases. The simulation results were verified by experimental findings and were found to be close to each other.

In [22] [23], [24], the diagnostic methods of line start permanent magnet synchronous motors have been investigated by using finite element analysis. Experimental results are provided to support the simulation results. The methodology taken is to analyze both the induction and the synchronous motors' frequency pattern of eccentricity fault. The authors found that static eccentricity fault frequency index for the LSPMS motor follows the same pattern of PMSM. Modeling of the fault condition is performed using finite element method to describe the transient behavior under different loading conditions. On other words, they are focusing on fault detection scheme using MCSA and frequency indices. However, the proposed indices are highly sensitive to any change in motor parameters. Consequently, the authors in [27] presented a work done on static, dynamic and mixed eccentricity fault diagnosis for PMSMs. This paper suggests a novel method for fault detection using stator current frequency patterns. Experimental results are obtained and verified using the finite element method. However, the authors state that the frequency patterns for stator current in the case of static, dynamic, and mixed eccentricity are influenced by motor input parameters such as load, as found in [22]. Besides, the detecting of static, dynamic, and mixed eccentricity in low power rating PMSMs was investigated in [57]. The fault detection process is based on MCSA and the fault condition is modeled using the winding function method.

The winding function method was used in [58] for calculating the mutual inductance between the stator and rotor in the LSPMS motor. The authors present the rotor as portions; each part has a high permeability and is separated by one layer of low permeable material. The finite element method is used to confirm the simulation results. Moreover, reference [59] presents an accurate model for calculating machine inductances for multiphase synchronous machine based on WFM. An important extension of this theory is introduced to permanent magnet motors. Model validation was performed using a finite element method. In the same manner, the authors in [30] presented a comparison between the winding function method, and FEM was conducted in terms of inductance calculation in synchronous machines. It has been shown that they have approximately the same results, but with different computation times. FEA requires more time than the WFM for calculating the machine parameters.

Jongman Hong et al. [60] presented a detection method for airgap eccentricity in permanent magnet synchronous motors based on the d-axis inductance. The authors claim that MCSA cannot distinguish eccentricity faults under variable load conditions with load torque oscillations. The authors noticed that the direct axis inductance decreased with an increment of eccentricity fault severity. This is due to changes in the degree of magnetic saturation; thus, the authors nominate the direct axis inductance to be the fault index. Model validation was performed by using the finite element method. Reference [61] is related to [60] by mean of determining the value of direct-axis inductance, this process involves estimating the direct-axis flux linkage.

Reference [62] presents a detailed model of PMSM using a magnetic equivalent circuit under eccentricity fault conditions. Results show that the incremental inductance due to eccentricity approaches a constant value when the core is operating in the linear region. In [63], the authors consider the effect of saturation rather than the liner operating point, as investigated in [62].

In [64], a model of bearing fault damage in PMSM is presented and simulated using MATLAB^{TM}. The analysis was performed in a dq reference frame. This paper proposed a method to accommodate the pulsating torque in the original healthy model by changing the torque equation. Frequency pattern of this fault was taken from the vibration model and used as a diagnostic method.

2.5 Detection of Eccentricity based on ANNs

The detection of motor faults is very important during motor operation. This will prevent the motor from being completely damaged, while also assisting preventive maintenance. Artificial neural networks (ANNs) can be utilized to detect and identify different types of motor faults. It is an efficient method for fault detection while avoiding the need for a mathematical model [65]. It is important to notice that no reported work has been done on detecting static eccentricity in LSPMS motors using ANNs. However, a brief review will be introduced regarding eccentricity detection in the induction and synchronous motors.

In [66], a detection of rotor eccentricity faults for a closed loop drive system in induction motors is performed using ANNs. This paper uses three-layer multilayers perceptron (MLP) with the back propagation method to adjust neural network weights. The amplitude of space current and voltage harmonic is measured for data acquisition and processing. The speed, and therefore, the mechanical load, will change widely in variable speed applications, and the amplitudes of the fault signals will vary accordingly. Thus, ANNs will be used to learn this complex relationship. Results show fine agreements between experimental and ANNs.

Bashir Ebrahimi et al. [26] presents a diagnostic method of static eccentricity based on FEM and ANNs. The diagnostic index is the amplitude of the harmonic components with a particular frequency pattern. To verify the ability of the proposed index, the correlation was determined between each eccentricity level and its harmonic index. This study is extended in [27] to include the effect of dynamic and mixed eccentricity.

According to [67], [68], a detection method of induction motor faults based on ANNs is presented using motor current signature analysis. The signal harmonics are obtained from the power spectra density, and used as discriminative features for the neural network to detect the faults. A comprehensive list of failures is considered, such as eccentricity, broken bars, and winding faults. An experimental setup is used for data acquisition.

2.6 Literature Review Summary:

This section summarizes the modeling directions of electrical motors under healthy and eccentricity fault conditions. Table 2.1 classify the diagnostic methods of eccentricity faults for the LSPMS motors, induction motors, and the synchronous motors. It was found that the diagnosis of static eccentricity in LSPMS motors is performed using FEM. The authors in [22] and [23] proposed a frequency index for static eccentricity fault detection. However, this frequency index is sensitive to any change in the motor parameters, such as the material types. Besides, Sedky [24] investigated the effects of static, dynamic, and mixed eccentricity on the motor phase current, speed, and torque characteristics. The author showed that the static eccentricity has no effect on the no load case with a damping effect under the loaded condition. On the other hand, the diagnosis directions of eccentricity fault in induction and synchronous motors are the FEM, MWFM, and the experimental method. Therefore, it can be concluded that the mathematical modeling of a static eccentricity fault in LSPMS motor is not found in the literature, and all the diagnostic methods are based on the FEM. However, the theory based approaches can be applied to the LSPMS motor under the eccentricity fault, which is the target of this thesis. Other techniques were used, such as the magnetic equivalent circuit approach, or measuring direct-axis inductance. However, these methods will lead to complex modeling expressions and costly instruments for measurement purposes.

Table 2.1: Literature review summary

Motor type	**Modeling directions under eccentricity fault**	**References**
LSPMS motors	FEM	[22], [23], [24]
Induction motor	M/WFM, FEM, and experimental	[21], [36], [40] [37] [38] [53] [43], [45], [44], [46],[47], [48] [49], [51], [50],[39], [42],[52]
Synchronous motors	M/WFM, FEM, and experimental	[54], [55], [56], [58], [59], [30]
	Other techniques	[27], [60], [61], [57], [62], [63], [64]
Induction and synchronous motors	Fault diagnostic using ANNs	[26], [27], [65], [66], [67], [68]

CHAPTER THREE

THE DEVELOPED MATHMATICAL MODEL OF THE LSPMS MOTOR

3.1 Introduction

In the LSPMS motor, the stator consists of three phase windings, which are displaced by 120 electrical degrees with N_s equivalent winding turns and phase resistance r_s. The rotor is equipped with permanent magnets (PM) and rotor bars. The rotor bars are shortened on both ends by end rings. This configuration is called a squirrel-cage rotor. As discussed before, this motor will start like an induction motor due to the rotor cage, and attains the synchronous speed due to magnets embedded in the rotor core.

The mathematical model of the LSPMS motor will be developed firstly in a healthy condition; then, the derivation will be extended under static eccentricity fault condition.

3.2 Mathematical Model Description

The following assumptions will be assumed through the derivation of the dynamic motor model of the LSPMS motor.

1. The stator windings distribution is sinusoidal.
2. An equivalent three-phase windings distribution of the rotor circuit.
3. Eddy current and hysteresis losses are neglected.
4. The magnetic operating point is assumed to have a fixed value.

Figure 3.1 shows the LSPMS motor with three phase windings for the stator and the rotor, the rotor cage, and the magnets. Besides, the stator and rotor winding axis, as well as the quadrature and direct axis of the magnets are shown.

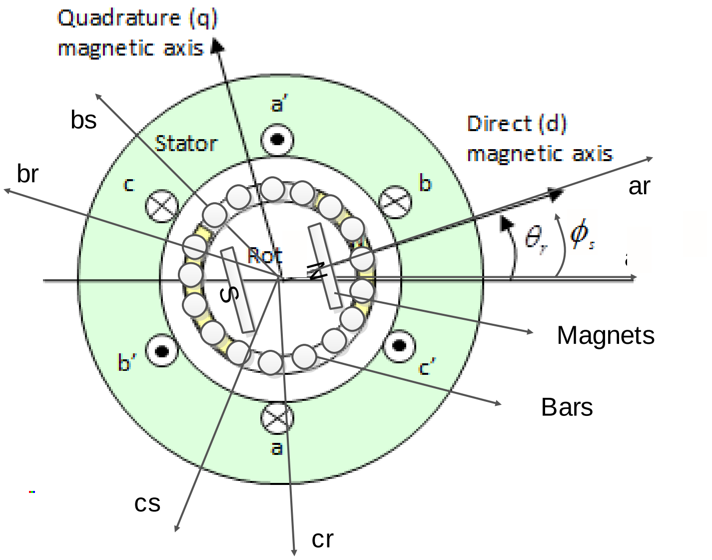

Figure 3.1: Stator and rotor circuits of LSPMS motor.

3.2.1 Stator and Rotor Voltage Equations

For the LSPMS motor shown in Figure 3.1, coupled magnetic circuit approach can be used to obtain the stator and rotor voltage equations:

$$\begin{bmatrix} V_{s,abc} \\ V_{r,abc} \end{bmatrix} = \begin{bmatrix} r_{s,abc} & 0 \\ 0 & r_{r,abc} \end{bmatrix} \begin{bmatrix} i_{s,abc} \\ i_{r,abc} \end{bmatrix} + \frac{d}{dt} \begin{bmatrix} \lambda_{s,abc} \\ \lambda_{r,abc} \end{bmatrix} \qquad (3.1)$$

Where $V_{s,abc}, i_{s,abc}, r_{s,abc}, \lambda_{s,abc}, V_{r,abc}, i_{r,abc}, r_{r,abc}, \lambda_{r,abc}$ are the stator and rotor phase voltages, currents, resistances, and flux linkages, respectively. They can be defined as the following:

$$V_{s,abc} = [\, V_{sa} \;\; V_{sb} \;\; V_{sc} \,]^T, \qquad i_{s,abc} = [\, i_{sa} \;\; i_{sb} \;\; i_{sc} \,]^T$$

$$V_{r,abc} = [\, V_{ra} \;\; V_{rb} \;\; V_{rc} \,]^T, \qquad i_{r,abc} = [\, i_{ra} \;\; i_{rb} \;\; i_{rc} \,]^T$$

$$\lambda_{s,abc} = [\, \lambda_{sa} \;\; \lambda_{sb} \;\; \lambda_{sc} \,]^T, \qquad \lambda_{r,abc} = [\, \lambda_{ra} \;\; \lambda_{rb} \;\; \lambda_{rc} \,]^T$$

$$r_{s,abc} = \begin{bmatrix} r_s & 0 & 0 \\ 0 & r_s & 0 \\ 0 & 0 & r_s \end{bmatrix} \;,\;\; r_{r,abc} = \begin{bmatrix} r_r & 0 & 0 \\ 0 & r_r & 0 \\ 0 & 0 & r_r \end{bmatrix}$$

The flux linkage equations for stator and rotor are given by:

$$\begin{bmatrix} \lambda_{s,abc} \\ \lambda_{r,abc} \end{bmatrix} = \begin{bmatrix} L_s & L_{sr} \\ L_{rs} & L_r \end{bmatrix} \begin{bmatrix} i_{s,abc} \\ i_{r,abc} \end{bmatrix} + \begin{bmatrix} \lambda_{s,pm} \\ \lambda_{r,pm} \end{bmatrix} \tag{3.2}$$

And,

$$\lambda_{pm} = \lambda_m \begin{bmatrix} \sin(\theta_r) \\ \sin(\theta_r - \frac{2\pi}{3}) \\ \sin(\theta_r + \frac{2\pi}{3}) \end{bmatrix} \tag{3.3}$$

Where L_S, L_r are the self-inductance of stator and rotor windings, L_{sr}, L_{rs} are the mutual inductance between stator and rotor, and rotor to stator, respectively. λ_{pm} are the permanent magnet flux components for stator $\lambda_{s,pm}$ and rotor $\lambda_{r,pm}$ with peak flux λ_m. θ_r as the angle of the permanent magnet flux with respect to the winding axis (as). This angle will be zero for the rotor components.

3.3 Transformation to qd0 Reference Frame

Dynamic qd0 modeling is used to study the motor during transient and steady state operation. In addition, this will result in time invariant inductance in equation (3.2). The Park's transformation is a well-known three-phase to qd0 transformation in synchronous machines [69]. The transformation equation is defined as:

$$S_{qd0} = \mathrm{K}(\theta)\, S_{\mathrm{abc}} \tag{3.4}$$

Where $S_{qd0}, K, S_{abc}, \theta$ are the output transformed variables, the transformation matrix, and the input variables, θ is the transformation angle. This transformation should be applied to transform the voltage and flux equations into the qd0 reference frame. The transformation axis will be attached to the rotor with $\omega = \omega_r$ or $\theta = \theta_r$ as presented in Figure 3.2.

The Park's transformation matrix K_s is given as:

$$K_s = \frac{2}{3}\begin{bmatrix} \cos(\theta_r) & \cos(\theta_r - \frac{2\,\pi}{3}) & \cos(\theta_r + \frac{2\,\pi}{3}) \\ \sin(\theta_r) & \sin(\theta_r - \frac{2\,\pi}{3}) & \sin(\theta_r + \frac{2\,\pi}{3}) \\ \frac{1}{2} & \frac{1}{2} & \frac{1}{2} \end{bmatrix} \tag{3.5}$$

The inverse of the transformation matrix can be obtained as:

$$(K_s)^{-1} = \begin{bmatrix} \cos(\theta_r) & \sin(\theta_r) & 1 \\ \cos(\theta_r - \frac{2\,\pi}{3}) & \sin\left(\theta_r - \frac{2\,\pi}{3}\right) & 1 \\ \cos(\theta_r + \frac{2\,\pi}{3}) & \sin(\theta_r + \frac{2\,\pi}{3}) & 1 \end{bmatrix} \tag{3.6}$$

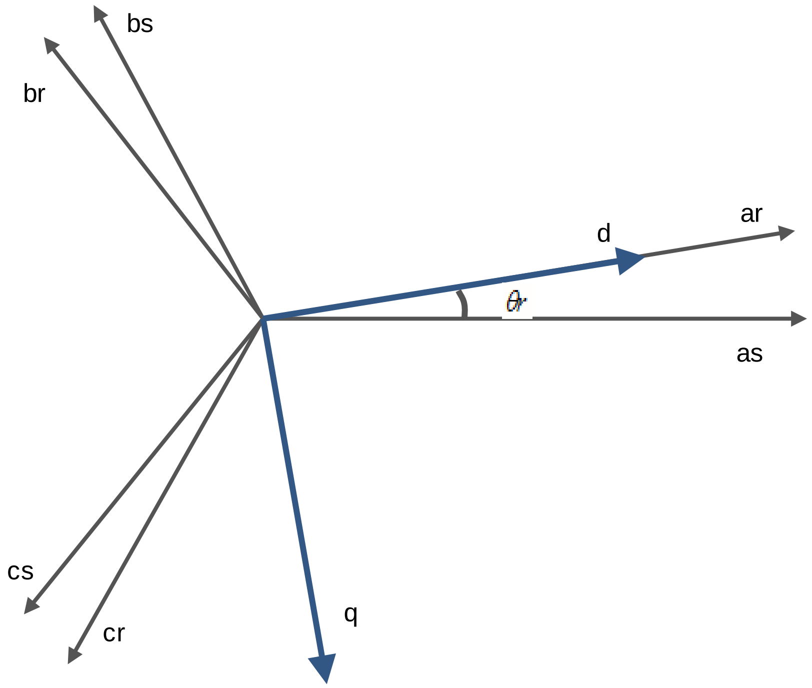

Figure 3.2: The qd reference frame attached to rotor.

Another important transformation, which can be used to transform the rotor variables to the qd0 reference frame, is Clark's transformation K_r. This transformation can be obtained by setting the transformation angle in equation (3.5) to zero [70].

3.3.1 Stator and Rotor Voltage Equations in qd0 Reference Frame

Following the last discussion in the previous section, the stator and rotor voltage equations will be transformed into a qd0 rotating reference. Performing the transformation to the stator voltage equations presented in equation (3.1) yields:

$$K_s V_s = K_s r_s i_s + K_s \frac{d}{dt} \lambda_{s,abc}$$

$$V_{s,qd0} = K_s r_s K_s^{-1} i_{s,qd0} + K_s \frac{d}{dt} \lambda_{s,abc} \tag{3.7}$$

The first term of the right-hand side can be written as:

$$K_s \frac{d}{dt} \left[\left(K_s^{-1} \lambda_{s,qd0}\right)\right] = K_s \frac{d}{dt} \left[\, K_s^{-1}\, \right] \lambda_{s,qd0} + K_s K_s^{-1} \frac{d}{dt} \lambda_{s,qd0} \tag{3.8}$$

Where:

$$\frac{d}{dt}\left(K_s^{-1}\right) = \omega_r \begin{bmatrix} -\sin(\theta_r) & \cos(\theta_r) & 0 \\ -\sin\left(\theta_r - \frac{2\pi}{3}\right) & \cos\left(\theta_r - \frac{2\pi}{3}\right) & 0 \\ -\sin\left(\theta_r + \frac{2\pi}{3}\right) & \cos\left(\theta_r + \frac{2\pi}{3}\right) & 0 \end{bmatrix} \tag{3.9}$$

But

$$K_s \frac{d}{dt} K_s^{-1} = \omega_r \begin{bmatrix} 0 & 1 & 0 \\ -1 & 0 & 0 \\ 0 & 0 & 0 \end{bmatrix} \tag{3.10}$$

So

$$V_{s,qd0} = r_s i_{s,qd0} + \omega_r \begin{bmatrix} 0 & 1 & 0 \\ -1 & 0 & 0 \\ 0 & 0 & 0 \end{bmatrix} \lambda_{s,qd0} + \frac{d}{dt} \lambda_{s,qd0} \tag{3.11}$$

Where $V_{s,qd0}$ are the stator voltage equations transformed into qd0 reference frame. In the same way, the rotor voltage equations obtained in equation (3.1) can be transformed to the qd0 reference frame as:

$$\begin{gathered} K_r V_{r,abc} = K_r r_r i_{r,abc} + K_r \frac{d}{dt} \lambda_{r.abc} \\ V_{r,qd0} = K_r r_r K_r^{-1} i_{r,qd0} + K_r \frac{d}{dt} \lambda_{r,abc} \end{gathered} \tag{3.12}$$

Again, for the first term of the right-hand side, it can be written as:

$$K_r \frac{d}{dt} \left[\left(K_r^{-1} \lambda_{r,qd0} \right) \right] = K_r \frac{d}{dt} \left[K_r^{-1} \right] \lambda_{r,qd0} + K_r K_r^{-1} \frac{d}{dt} \lambda_{r,qd0} \tag{3.13}$$

But

$$\begin{gathered} \frac{d}{dt} (K_r^{-1}) = 0 \\ K_r K_r^{-1} = \mathrm{I} \end{gathered} \tag{3.14}$$

So,

$$V_{r,qd0} = 0 = r_{\mathrm{r}} i_{r,qd0} + \frac{d}{dt} \lambda_{r,qd0} \tag{3.15}$$

3.3.2 Flux Linkage Equations in qd0 Reference Frame:

Recall that the flux linkage equations are given in equation (3.2). Applying the transformation to the rotating reference frame and substituting the values of the current in qd0 reference frame yields:

$$\begin{bmatrix} \lambda_{s,qd0} \\ \lambda_{r,qd0} \end{bmatrix} = \begin{bmatrix} K_s L_s K_s^{-1} & K_s L_{sr} K_r^{-1} \\ K_r L_{sr} K_s^{-1} & K_r L_r K_r^{-1} \end{bmatrix} \begin{bmatrix} i_{s,qd0} \\ i_{r,qd0} \end{bmatrix} + \begin{bmatrix} K_s \lambda_{s,pm} \\ K_r \lambda_{r,pm} \end{bmatrix} \tag{3.16}$$

The transformation of λ_{pm} to the rotor reference frame is considered by setting $\theta_m = \theta_r$ as the stator components and $\theta_m = 0$ as the rotor components, which yields:

$$\lambda_{s,m} = K_s \lambda_{s,pm} = \lambda_m \begin{bmatrix} 0 \\ 1 \\ 0 \end{bmatrix} \tag{3.17}$$

For the rotor components, the flux becomes:

$$\lambda_{r,m} = K_r \lambda_{r,pm} = \lambda_m \begin{bmatrix} 0 \\ 1 \\ 0 \end{bmatrix} \tag{3.18}$$

Which means that the permanent magnet flux components are shown only on the d-axis for both stator and rotor, which is donated by $\lambda_{s,m}$, and $\lambda_{r,m}$. The flux linkage equations become:

$$\begin{bmatrix}\lambda_{s,qd0}\\ \lambda_{r,qd0}\end{bmatrix}=\begin{bmatrix}K_sL_sK_s^{-1} & K_sL_{sr}K_r^{-1}\\ K_rL_{sr}K_s^{-1} & K_rL_rK_r^{-1}\end{bmatrix}\begin{bmatrix}i_{s,qd0}\\ i_{r,qd0}\end{bmatrix}+\begin{bmatrix}\lambda_{s,m}\\ \lambda_{r,m}\end{bmatrix} \tag{3.19}$$

The detailed calculation of the inductance terms shown in equation (3.19) will be presented in section 3.5 based on the MWFM, and it will lead to the following inductance expressions:

$$L_{s,qd0}=K_sL_sK_s^{-1}=\begin{bmatrix}L_{ls}+\frac{3}{2}L_{ss,q} & 0 & 0\\ 0 & L_{ls}+\frac{3}{2}L_{ss,d} & 0\\ 0 & 0 & L_{ls}\end{bmatrix} \tag{3.20}$$

$$L_{sr,qd0}=K_sL_{sr}K_r^{-1}=\begin{bmatrix}\frac{3}{2}L_{sr,q} & 0 & 0\\ 0 & \frac{3}{2}L_{sr,d} & 0\\ 0 & 0 & 0\end{bmatrix} \tag{3.21}$$

$$L_{rs,qd0}=L_{sr,qd0}^{T} \tag{3.22}$$

$$L_{r,qd0}=K_rL_rK_r^{-1}=\begin{bmatrix}L_{lr}+\frac{3}{2}L_{rr,q} & 0 & 0\\ 0 & L_{lr}+\frac{3}{2}L_{rr,d} & 0\\ 0 & 0 & L_{lr}\end{bmatrix} \tag{3.23}$$

Where $L_{ss,q}, L_{ss,d}, L_{rr,q}, L_{rr,d}, L_{sr,q}, L_{sr,d}$ are the self-inductance of stator and rotor windings, and the mutual inductance between stator and rotor in the direction of quadrature and direct axis, respectively. L_{ls}, L_{lr} are the per phase leakage inductance of stator and rotor windings. Defining the following magnetizing inductances for a symmetric winding distribution and by referring the inductances into the stator side, yields:

$$L_{mq} = \frac{3}{2} L_{ss,q} = \frac{3}{2} \frac{N_s}{N_r} L_{rr,q} = \frac{3}{2} \frac{N_s}{N_r} L_{sr,q}$$

$$L_{md} = \frac{3}{2} L_{ss,d} = \frac{3}{2} \frac{N_s}{N_r} L_{rr,d} = \frac{3}{2} \frac{N_s}{N_r} L_{sr,d} \tag{3.24}$$

Where N_s, N_r are the number of stator and rotor turns, respectively. The complete flux linkage equations of stator and rotor can be written in compact form as:

$$\begin{bmatrix} \lambda_{sq} \\ \lambda_{sd} \\ \lambda_{s0} \\ \lambda_{rq} \\ \lambda_{rd} \\ \lambda_{r0} \end{bmatrix} = \begin{bmatrix} L_{ls} + L_{mq} & 0 & 0 & L_{mq} & 0 & 0 \\ 0 & L_{ls} + L_{md} & 0 & 0 & L_{md} & 0 \\ 0 & 0 & L_{ls} & 0 & 0 & 0 \\ L_{mq} & 0 & 0 & L_{lr} + L_{mq} & 0 & 0 \\ 0 & L_{md} & 0 & 0 & L_{lr} + L_{md} & 0 \\ 0 & 0 & 0 & 0 & 0 & L_{lr} \end{bmatrix} \begin{bmatrix} i_{sq} \\ i_{sd} \\ i_{s0} \\ i_{rq} \\ i_{rd} \\ i_{r0} \end{bmatrix} + \begin{bmatrix} 0 \\ \lambda_m \\ 0 \\ 0 \\ \lambda_m \\ 0 \end{bmatrix} \tag{25}$$

Where $\lambda_m = i_m \, L_{md}$ which is the magnetization current multiplied with the mutual d-axis inductance.

3.3.3 Equation of Motion and Electromagnetic Torque

The electromechanical torque developed by the motor can be obtained from the input power being transferred into the airgap [69], which is given by:

$$T_{em} = \frac{3}{2} \frac{P}{2} \left(\lambda_d i_q - \lambda_q i_d \right) \tag{3.26}$$

In addition, the rotor motion equation is governed by:

$$\omega_r(t) = \frac{P}{2J} \int \left(T_{em} + T_{mech} - T_{damp} \right) dt \tag{3.27}$$

Where P is the number of poles, J is the motor inertia, T_{mech} is the input mechanical load, T_{damp} is the damping torque, and ω_r is the rotor angular velocity.

3.3.4 Healthy Model Summary

The summary of the healthy model equations is introduced in the synchronous reference frame for stator and rotor voltage and flux equations. In the following equations, the prime notation indicates rotor variables being referred to the stator side by a proper turn ratio which can be defined as:

$$\lambda'_{rqd} = \frac{N_s}{N_r}\lambda_{rqd} \tag{3.28}$$

$$i'_{rqd} = \frac{N_r}{N_s}i_{rqd} \tag{3.29}$$

$$l'_{lr} = \left[\frac{N_s}{N_r}\right]^2 l_{lr} \tag{3.30}$$

The voltage and flux equations becomes:

$$V_{s,qd0} = r_s i_{s,qd0} + \omega_r \begin{bmatrix} 0 & 1 & 0 \\ -1 & 0 & 0 \\ 0 & 0 & 0 \end{bmatrix} \lambda_{s,qd0} + \frac{d}{dt}\lambda_{s,qd0} \tag{3.31}$$

$$V'_{r,qd0} = 0 = r'_r i_{r},'_{qd0} + \frac{d}{dt}\lambda'_{r,qd0} \tag{3.32}$$

$$\begin{bmatrix}\lambda_{sq}\\ \lambda_{sd}\\ \lambda_{s0}\\ \lambda'_{rq}\\ \lambda'_{rd}\\ \lambda'_{r0}\end{bmatrix}=\begin{bmatrix}L_{ls}+L_{mq} & 0 & 0 & L_{mq} & 0 & 0\\ 0 & L_{ls}+L_{md} & 0 & 0 & L_{md} & 0\\ 0 & 0 & L_{ls} & 0 & 0 & 0\\ L_{mq} & 0 & 0 & L'_{lr}+L_{mq} & 0 & 0\\ 0 & L_{md} & 0 & 0 & L'_{lr}+L_{md} & 0\\ 0 & 0 & 0 & 0 & 0 & L'_{lr}\end{bmatrix}\begin{bmatrix}i_{sq}\\ i_{sd}\\ i_{s0}\\ i'_{rq}\\ i'_{rd}\\ i'_{r0}\end{bmatrix}+\begin{bmatrix}0\\ \lambda_m\\ 0\\ 0\\ \lambda'_m\\ 0\end{bmatrix} \tag{3.33}$$

3.4 Mathematical Model of LSPMS motor under Static Eccentricity Condition

Successful modeling of static eccentricity depends on the calculation of the motor inductances. The fault condition will be modeled using MWFM. The next subsections will demonstrate the mathematical representation of the modified winding function theory. In addition, the evaluation methods for calculating the motor inductances will be introduced. During the development of the analytical model, the assumptions made during the healthy model derivation are valid here.

3.4.1 Modified Winding Function Method

The MWFM is widely discussed in literature, with references [5], [25], and [31] introducing this method in more detail. However, a brief review of this method is introduced here. Consider the partial motor geometry shown in Figure 3.3, which consists of two concentric cylinders with a length of l and outer rotor radius r. Assume that two sets of winding A and B are attached to the inner stator race with negligible turn thickness.

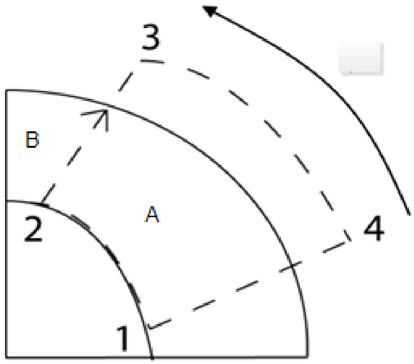

Figure 3.3: Ampere loop through the motor geometry

Applying ampere law to the loop 12341, which encloses the stator winding A:

$$\int_L H.dl = \int_s J.ds \tag{3.34}$$

Where H is the magnetic field intensity, and dl is the differential length defined to be along the flux lines terminating at two points of the closed path. J and ds are the current density and the differential surface enclosed by the path 12341, respectively. If $n(\phi)$ is defined as the turn function of the stator winding A, which carries a uniform current i_A; then equation (3.34) can be written as:

$$\int H.dl = n(\phi)\, i_A \tag{3.35}$$

The MWFM assumes that the axial component of the magnetic field is negligible, the radial component is constant along the airgap, and the permeability of the iron is infinite. Therefore, the above equation can be written in terms of the magnetomotive force F as:

$$F_{41}(0) + F_{23}(\phi) = n(\phi)\, i_A \tag{3.36}$$

$$\begin{aligned} F_{41}(0) &= -H(r,0)\, g(0) \\ F_{23}(\phi) &= H(r,\phi)\, g(\phi) \end{aligned} \tag{3.37}$$

Where $g(\phi)$ is the airgap length. Another additional equation is needed; it is obtained from Gauss' Theorem, which states that the net flux leaving any closed surface is equal to zero, or:

$$\int \mu_0\, H\, .\, dA = 0 \tag{3.38}$$

Where, $B = \mu_0 H$ is the magnetic field density, and dA is the differential cross sectional area. Taking the integration over the total length l around a cylindrical volume, equation (3.38) can be written as:

$$\int_0^{2\pi} \int_0^{l} \mu_0\, H(\phi, r) r\, .\, dl\, .\, d\phi = 0 \tag{3.39}$$

Hence r and l are constants, this equation can be written as:

$$\int_0^{2\pi} H(\phi, r)\, .\, d\phi = 0 \tag{3.40}$$

Substitute the value of $H(\phi, r)$ in equation (3.40), which yields:

$$\int_0^{2\pi} \frac{F(\phi)}{g(\phi)}\, d\phi = 0 \tag{3.41}$$

Using equation (3.36), dividing by $g(\phi)$ and taking the integration from 0 to 2π, yields:

$$\int \left(\frac{F_{41}(0)}{g(\phi)} + \frac{F_{23}(\phi)}{g(\phi)}\right) . d\phi = \int_0^{2\pi} \frac{n(\phi)}{g(\phi)}\, i_A \,. d\phi \tag{3.42}$$

The second term on the left-hand side is equal to zero, hence equation (3.42) can be written as:

$$F_{41}(0) = \frac{1}{2\pi < g^{-1}(\phi) >} \int_0^{2\pi} n(\phi)\, g^{-1}(\phi)\, i_A \,. d\phi \tag{3.43}$$

Solving for $F_{23}(\phi)$ using equation (3.36), yields:

$$F_{23}(\phi) = \left[n(\phi) - \frac{1}{2\pi < g^{-1}(\phi) >} \int_0^{2\pi} n(\phi)\, g^{-1}(\phi) \;. d\phi \right] i_A \tag{3.44}$$

The expression in equation (3.44) gives the MMF at any point in the airgap of the motor. This expression leads to the modified winding function $N(\phi)$ of the motor which can be written as the follows:

$$N(\phi) = n(\phi) - \frac{1}{2\pi < g^{-1}(\phi) >} \int_0^{2\pi} n(\phi)\, g^{-1}(\phi) \;. d\phi \tag{3.45}$$

3.4.2 Inductance Calculation using MWFM

Two sets of windings, A and B, are assumed in the previous discussion. The mutual inductance of winding B with respect to winding A is the flux linking winding B due to the current flow in winding A and vice versa. Using equation (3.35), the magnetomotive force F caused by i_A of winding A can be written as:

$$F_A(\phi) = N_A(\phi)\, i_A \tag{3.46}$$

From elementary magnetic circuits, airgap flux Φ is related to the MMF by:

$$\Phi = F\, \mathcal{P} \tag{3.47}$$

Where $\mathcal{P}$ is the permeance of the flux path, the differential flux $d\psi$ across the gap through a differential volume of length $g(\phi)$ and cross-sectional area $rld\phi$ from rotor to the stator is:

$$\boldsymbol{d\psi = F_A(\phi)\frac{\mu_0 rl}{g(\phi)}} \tag{3.48}$$

The flux linking winding B due to the current flow in winding A can be determined by multiplying the right-hand side of equation (3.48) with the turn function of winding B which is $n_B(\phi)$, and integrating over 2π which yields:

$$\psi = \mu_0 rl \int_0^{2\pi} F_A(\phi)\, n_B(\phi)\, g^{-1}(\phi).\, d\phi \tag{3.49}$$

Substituting for the value of $F_A(\phi)$ in equation (3.49), and dividing the equation by i_A results in L_{BA}, which is the mutual inductance linking winding B due to the current flow in winding A.

$$L_{BA} = \mu_0 rl \int_0^{2\pi} N_A(\phi)\, n_B(\phi) g^{-1}(\phi).\, d\phi \tag{3.50}$$

The self-inductance can be calculated by considering the turn function of winding A instead of winding B, which results in L_{AA}.

$$L_{AA} = \mu_0 r l \int_0^{2\pi} N_A(\phi)\, n_A(\phi) g^{-1}(\phi).\, d\phi \tag{3.51}$$

3.4.3 Static Eccentricity Modeling

Static eccentricity indicates that the center of rotation of the rotor is not the same as the symmetry center of stator. Eccentricity, in general, will affect the motor inductances. Thus, the previously presented inductance matrices in a healthy condition are not valid for the model under the static eccentricity fault condition. In this thesis, the coupled magnetic circuit approach can be used to represent the model of the LSPMS motor under the static eccentricity fault condition. Besides, the MWFM can be used to estimate the motor inductances.

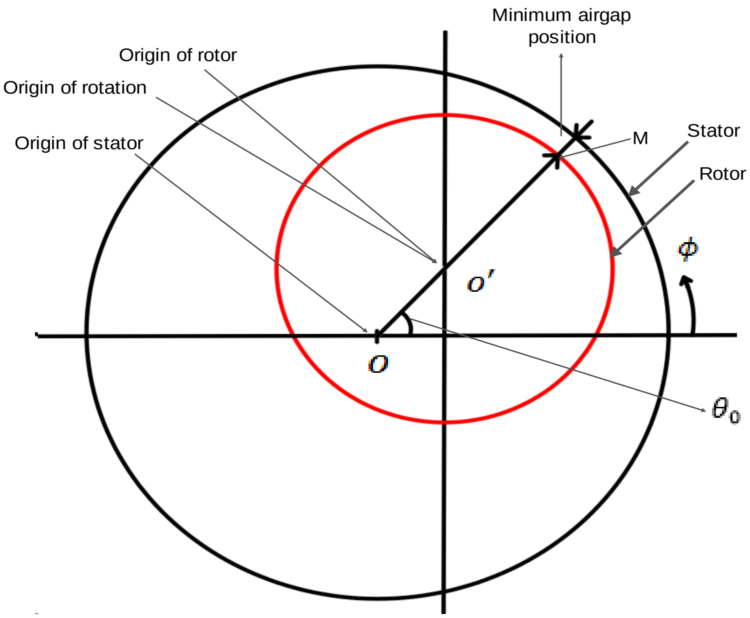

Figure 3.4: Motor geometry with static eccentricity.

Eccentricity is a mechanical related fault; the occurrence of static eccentricity will change the motor rotational axis symmetry. Therefore, considering the non-uniform airgap distribution is necessary. According to [71], the airgap permeance is inversely proportional to the airgap length, as shown in equation (3.52). Thus, the airgap permeance can be neglected for points far from the rotor poles.

$$P(\phi) = \mu_0 \frac{r_{av}(\phi)}{g(\phi)} \tag{3.52}$$

Where $\mu_0, r_{av}(\phi)$, $g(\phi)$, and ϕ are the permeability in space, the average radius of airgap, the airgap function, and the base angle for measurement, respectively. Figure 3.4 presents the motor geometry with static eccentricity. The rotor center of rotation o' is offset from the center of stator o to represent an eccentric rotor. Vector $\overrightarrow{OO'}$ is called the static eccentricity vector. The degree of static eccentricity δ_s is defined as the ratio of the static eccentricity vector $|\overrightarrow{OO'}|$ to the symmetrical airgap length g_0 [22], which yields:

$$\delta_s = \frac{|\overrightarrow{OO'}|}{\mathrm{g}_0} \tag{3.53}$$

This vector is fixed in space under static eccentricity and its position is described by angle θ_0. This angle describes the stationary position of the minimum airgap along the inner stator surface. For an arbitrary point M located on the rotor outer race, the distance between this point and rotor center is equal to rotor radius, [36], or:

$$OM = \delta_s g cos(\phi - \theta_0) + \sqrt{R_r^2 - \delta_s^2 g_0^2 \sin^2(\phi - \theta_0)} \tag{3.54}$$

Where R_r is the rotor outer radius. For a stator inner radius of R_s, the airgap function can be obtained as:

$$g(\phi) = R_s - OM \tag{3.55}$$

Since the rotor radius is much larger than the airgap length, the second term in equation (3.54) can be represented by R_r. Therefore, equation (3.55) can be written as [72]:

$$g(\phi) = \mathrm{g}_0[1 - \delta_s \cos(\phi - \theta_0)] \tag{3.56}$$

Figure 3.5 shows the case when considering the angle of SE vector equal to zero, the center of rotation is offset from the center of the stator by a distance of $g_0 * \delta_s$. The distance between the stator inner race and rotor outer race at the minimum distance is equal to $g_0(\delta_s - 1)$ and the maximum airgap distance will be equal to $g_0(\delta_s + 1)$.

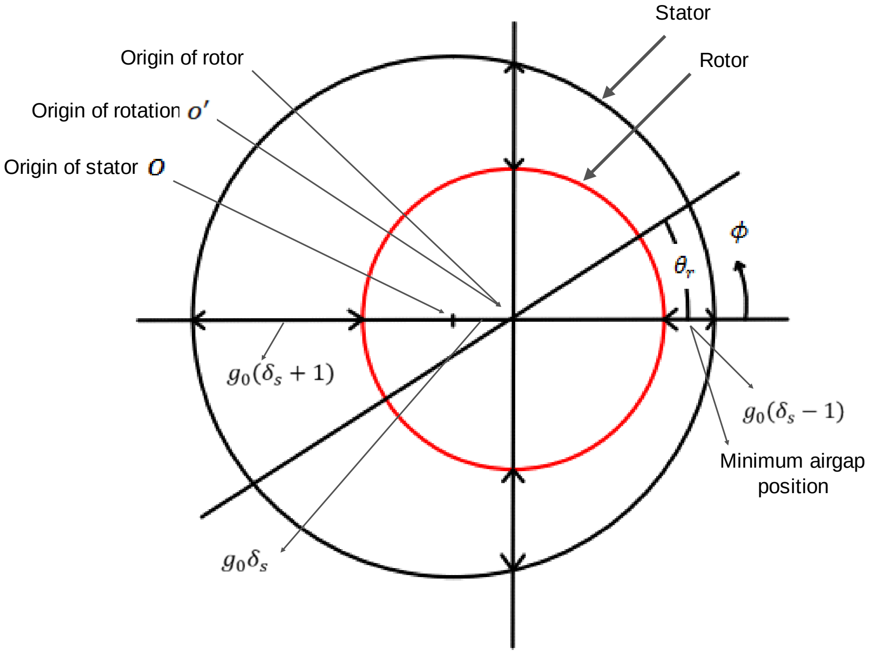

Figure 3.5: Motor geometry with static eccentricity for $\boldsymbol{\theta_0 = 0}$.

For the calculation of the inductances in the MWFM, the inverse of the airgap function is needed. It is represented in equation (3.57) as:

$$g^{-1}(\phi) = \frac{1}{\mathrm{g}_0[1 - \delta_s \cos(\phi - \theta_0)]} \tag{3.57}$$

The above equation can be expressed in Fourier series form as:

$$g^{-1}(\phi) = A_0 + \sum_{n}^{\infty} A_n \, Cos\, n(\phi - \theta_0) \qquad n = 1{,}2.. \tag{3.58}$$

Where:

$$A_0 = \frac{1}{\mathrm{g}_0\sqrt{1 - \delta_s^2}} \;\; ; \;\; A_n = \frac{2}{\mathrm{g}_0\sqrt{1 - \delta_s^2}} \left[\frac{1 - \sqrt{1 - \delta_s^2}}{\delta_s^2}\right]^n \tag{3.59}$$

The inverse function for the first term can be written as:

$$\begin{aligned} g^{-1}(\phi) &= \frac{1}{\mathrm{g}_0\sqrt{1 - \delta_s^2}} + 2\,\frac{1 - \sqrt{1 - \delta_s^2}}{\mathrm{g}_0\delta_s^2\,\sqrt{1 - \delta_s^2}} \cos(\phi - \theta_0) \\ &= \mathrm{A}_0 + \mathrm{A}_1 \cos(\phi - \theta_0) \end{aligned} \tag{3.60}$$

3.5 Inductance Calculation under Static Eccentricity Condition

According to [25], the turn functions of the stator windings can be represented as:

$$n_{as}(\phi) = \frac{N_s}{2P_p}\,[\cos(\phi) - 1\,]$$

$$n_{bs}(\phi) = \frac{N_s}{2P_p}\,[\cos(\phi - 120^o) - 1\,] \tag{3.61}$$

$$n_{cs}(\phi) = \frac{N_s}{2P_p}\,[\cos(\phi + 120^o) - 1\,]$$

Where P_p presents the number pole pairs. In the same way, the rotor windings are assumed to have a sinusoidal distribution with initial angle θ_r. These turn functions are given as the following:

$$n_{ar}(\phi, \theta_r) = \frac{N_r}{2P_p}\,[\cos(\phi - \theta_r) - 1\,]$$

$$n_{br}(\phi, \theta_r) = \frac{N_r}{2P_p}\,[\cos(\phi - \theta_r - 120^o) - 1\,] \tag{3.62}$$

$$n_{cr}(\phi, \theta_r) = \frac{N_r}{2P_p}\,[\cos(\phi - \theta_r + 120^o) - 1\,]$$

To obtain the winding function, which is needed to calculate the new inductance matrices, equation (3.45) should be used. For example, the modified winding function of phase (as) can be obtained as the following:

$$N_{as}(\phi) = n_{as}(\phi) - < N_{as}(\phi) >$$

$$N_{as}(\phi) = n_{as}(\phi) - \int_0^{2\pi} \frac{n_{as}(\phi) g^{-1}(\phi)}{2\pi < g^{-1}(\phi) >}\,.d\phi \tag{3.63}$$

Where $< g^{-1}(\phi) >$ is the average value of the inverse airgap function which obtained as:

$$< g^{-1}(\phi) > = \frac{A_0}{g_0} \tag{3.64}$$

The integration side becomes:

$$\int_0^{2\pi} \frac{-n_{as}(\phi) g^{-1}(\phi)}{2\pi < g^{-1}(\phi) >} . d\phi = -\frac{g_0}{2\pi A_0} \int_0^{2\pi} \frac{N_s}{2} \left[\cos(\phi) - 1\right] . \left[\frac{A_0}{g_0} + \frac{A_1}{g_0}\cos(\phi)\right] d\phi$$

$$= -\frac{N_s\, g_0}{4\pi P_p A_0} \int_0^{2\pi} [\frac{A_1}{g_0}\cos^2(\phi) - \frac{A_0}{g_0}]\, d\phi$$

$$= -\frac{N_s\, g_0}{2\pi A_0} \left[\frac{A_1}{g_0} \int_0^{2\pi} \left[\frac{1}{2} + \frac{\cos(2\phi)}{2}\right] d\phi - \int_0^{2\pi} \frac{A_0}{g_0}\, d\phi \right] = -\frac{N_s\, g_0}{4\pi P_p A_0} \left[\frac{\pi A_1}{g_0} - \frac{2\pi A_0}{g_0}\right]$$

$$= \frac{N_s(2A_0 - A_1)}{4 P_p A_0}$$

$$N_{as}(\phi) = \frac{N_s}{2P_p} \left[\cos(\phi) - 1\right] + \frac{N_s(2A_0 - A_1)}{4P_p A_0} = \frac{N_s}{2P_p} \left[\cos(\phi) - \frac{A_1}{2A_0}\right] \tag{3.65}$$

In the same way, to find the modified winding function for the rest of stator windings. MATLAB^{TM} symbolic integration can be used for this purpose.

$$\begin{aligned} N_{bs}(\phi) &= \frac{N_s}{2P_p} \left[\cos(\phi - 120^0) + \frac{A_1}{4A_0}\right] \\ N_{cs}(\phi) &= \frac{N_s}{2P_p} \left[\cos(\phi + 120^0) + \frac{A_1}{4A_0}\right] \end{aligned} \tag{3.66}$$

Similarly, the rotor modified winding function for phase (ar) is given as:

$$N_{ar}(\phi) = n_{ar}(\phi, \theta_r) - \int_0^{2\pi} \frac{n_{ar}(\phi, \theta_r) g^{-1}(\phi)}{2\pi < g^{-1}(\phi) >} \, .d\phi \tag{3.67}$$

The integration side becomes:

$$= -\frac{g_0}{2\pi A_0} \int_0^{2\pi} \frac{N_r}{2P_p} \left[\cos(\phi - \theta_r) - 1\right] . \left[\frac{A_0}{g_0} + \frac{A_1}{g_0}\cos(\phi)\right] d\phi$$

$$N_{ar}(\phi, \theta_r) = \frac{N_r}{2P_p}\left[\cos(\phi - \theta_r) - \frac{A_1}{2A_0}\cos(\theta_r)\right] \tag{3.68}$$

In the same way, the modified winding functions for phase (br) and (cr) are:

$$\begin{gathered} N_{br}(\phi, \theta_r) = \frac{N_r}{2P_p}\left[\cos(\phi - \theta_r - 120^0) - \frac{A_1}{2A_0}\cos(\theta_r + 120^0)\right] \\ N_{cr}(\phi, \theta_r) = \frac{N_r}{2P_p}\left[\cos(\phi - \theta_r + 120^0) - \frac{A_1}{2A_0}\cos(\theta_r - 120^0)\right] \end{gathered} \tag{3.69}$$

The inductance matrices, as presented in equation (3.2), should be re-calculated for the healthy condition. For this purpose, MATLAB$^{\text{TM}}$ symbolic integration is used. Since the windings are on the stator and rotor circuits, the inductance matrix has a dimension of 3 by 3. In addition, the leakage inductance of stator l_{ls} and rotor l_{ls} windings are included. The following integrations are calculated based on equation (3.50) and (3.51) for both self and mutual inductance.

$$L_{ss}^{SE} = \mu_0 rl \begin{bmatrix} L_{ls} + \int_0^{2\pi} N_{as}(\phi)\, n_{as}(\phi) g^{-1}(\phi) d\phi & \int_0^{2\pi} N_{bs}(\phi)\, n_{as}(\phi) g^{-1}(\phi) d\phi & \int_0^{2\pi} N_{cs}(\phi)\, n_{as}(\phi) g^{-1}(\phi) d\phi \\ \int_0^{2\pi} N_{as}(\phi)\, n_{bs}(\phi) g^{-1}(\phi) d\phi & L_{ls} + \int_0^{2\pi} N_{bs}(\phi)\, n_{bs}(\phi) g^{-1}(\phi) d\phi & \int_0^{2\pi} N_{cs}(\phi)\, n_{bs}(\phi) g^{-1}(\phi) d\phi \\ \int_0^{2\pi} N_{as}(\phi)\, n_{cs}(\phi) g^{-1}(\phi) d\phi & \int_0^{2\pi} N_{bs}(\phi)\, n_{cs}(\phi) g^{-1}(\phi) d\phi & L_{ls} + \int_0^{2\pi} N_{cs}(\phi)\, n_{cs}(\phi) g^{-1}(\phi) d\phi \end{bmatrix} \tag{3.70}$$

In the same way, the rotor inductance matrix is obtained as follows:

$$L_{rr}^{SE} = \mu_0 rl \begin{bmatrix} L_{lr} + \int_0^{2\pi} N_{ar}(\phi)\, n_{ar}(\phi) g^{-1}(\phi) d\phi & \int_0^{2\pi} N_{br}(\phi)\, n_{ar}(\phi) g^{-1}(\phi) d\phi & \int_0^{2\pi} N_{cr}(\phi)\, n_{ar}(\phi) g^{-1}(\phi) d\phi \\ \int_0^{2\pi} N_{ar}(\phi)\, n_{br}(\phi) g^{-1}(\phi) d\phi & L_{lr} + \int_0^{2\pi} N_{br}(\phi)\, n_{br}(\phi) g^{-1}(\phi) d\phi & \int_0^{2\pi} N_{cr}(\phi)\, n_{br}(\phi) g^{-1}(\phi) d\phi \\ \int_0^{2\pi} N_{ar}(\phi)\, n_{cr}(\phi) g^{-1}(\phi) d\phi & \int_0^{2\pi} N_{br}(\phi)\, n_{cr}(\phi) g^{-1}(\phi) d\phi & L_{lr} + \int_0^{2\pi} N_{cr}(\phi)\, n_{cr}(\phi) g^{-1}(\phi) d\phi \end{bmatrix} \tag{3.71}$$

Consequently, the stator to rotor mutual inductance matrix is obtained as:

$$L_{sr}^{SE} = \mu_0 rl \begin{bmatrix} \int_0^{2\pi} N_{ar}(\phi, \theta_r)\, n_{as}(\phi) g^{-1}(\phi) d\phi & \int_0^{2\pi} N_{br}(\phi, \theta_r)\, n_{as}(\phi) g^{-1}(\phi) d\phi & \int_0^{2\pi} N_{cr}(\phi, \theta_r)\, n_{as}(\phi) g^{-1}(\phi) d\phi \\ \int_0^{2\pi} N_{ar}(\phi, \theta_r)\, n_{bs}(\phi) g^{-1}(\phi) d\phi & \int_0^{2\pi} N_{br}(\phi, \theta_r)\, n_{bs}(\phi) g^{-1}(\phi) d\phi & \int_0^{2\pi} N_{cr}(\phi, \theta_r)\, n_{bs}(\phi) g^{-1}(\phi) d\phi \\ \int_0^{2\pi} N_{ar}(\phi, \theta_r)\, n_{cs}(\phi) g^{-1}(\phi) d\phi & \int_0^{2\pi} N_{br}(\phi, \theta_r)\, n_{cs}(\phi) g^{-1}(\phi) d\phi & \int_0^{2\pi} N_{cr}(\phi, \theta_r)\, n_{cs}(\phi) g^{-1}(\phi) d\phi \end{bmatrix} \tag{3.72}$$

$$L_{rs}^{SE} = (L_{sr}^{SE})^T \tag{3.73}$$

The superscript (SE) indicates that the inductance matrix is under the faulty condition. The flux linkage equations under a static eccentricity condition will have the following form:

$$\begin{bmatrix} \lambda_{s,abc} \\ \lambda_{r,abc} \end{bmatrix} = \begin{bmatrix} L_{ss}^{SE} & L_{sr}^{SE} \\ L_{rs}^{SE} & L_{rr}^{SE} \end{bmatrix} \begin{bmatrix} i_{s,abc} \\ i_{r,abc} \end{bmatrix} + \begin{bmatrix} \lambda_{s,pm} \\ \lambda_{r,pm} \end{bmatrix} \tag{3.74}$$

3.6 Transformation to the Rotor Reference Frame:

As discussed before, equation (3.4) can be utilized to transform the flux linkages and currents of stator and rotor circuits in equation (3.74), which yields:

$$\begin{bmatrix} \lambda_{s,qd0} \\ \lambda_{r,qd0} \end{bmatrix} = \begin{bmatrix} K_s L_{ss}^{SE} K_s^{-1} & K_s L_{sr}^{SE} K_r^{-1} \\ K_r L_{sr}^{SE} K_s^{-1} & K_r L_{rr}^{SE} K_r^{-1} \end{bmatrix} \begin{bmatrix} i_{s,qd0} \\ i_{r,qd0} \end{bmatrix} + \begin{bmatrix} K_s \lambda_{s,pm} \\ K_r \lambda_{r,pm} \end{bmatrix} \tag{3.75}$$

The transformation of the self-inductance matrix, as presented in equation (3.70), is conducted as:

$$L_{s,qd}^{SE} = K_s \, L_{ss}^{SE} \, K_s^{-1} \tag{3.76}$$

$$= \begin{bmatrix} L_{ls} + \dfrac{3\pi A_0 \mu_0 N_e^2 lr}{8 g_0 P_p^2} - \dfrac{3\pi A_1^2 \mu_0 N_e^2 lr\, cos^2(\theta_r - \theta_0)}{16 A_0 g_0 P_p^2} & -\dfrac{3\pi A_1^2 \mu_0 N_e^2 lr\, sin(2(\theta_r - \theta_0))}{32 A_0 g_0 P_p^2} & 0 \\ -\dfrac{3\pi A_1^2 \mu_0 N_e^2 lr\, sin(2(\theta_r - \theta_0))}{32 A_0 g_0 P_p^2} & L_{ls} + \dfrac{3\pi \mu_0 N_e^2 lr (A_1^2 \sin^2(\theta_r - \theta_0) \; - \; 2A_0^2)}{16 A_0 g_{0\zeta} P_p^2} & 0 \\ 0 & 0 & L_{ls} \end{bmatrix} \tag{3.77}$$

Where N_e is the equivalent number of winding turns and ζ is the saliency ratio. The inductance terms in equation (3.77) can be rearranged to separate the fault contribution from the terms of the healthy inductances. The healthy inductances can be obtained by setting the degree of static eccentricity to a very small value near zero in equation (3.60).

Therefore, the rest terms will present the fault component indicated as L_e. Equation (3.77) can be written as:

$$L_{s,qd}^{SE} = \begin{bmatrix} L_{ls} + \frac{3}{2}(L_{ss} + L_e \cos^2(\theta_r - \theta_0)) & \frac{3}{2} L_e \cos(\theta_r - \theta_0) \sin(\theta_r - \theta_0) & 0 \\ \frac{3}{2} L_e \cos(\theta_r - \theta_0) \sin(\theta_r - \theta_0) & L_{ls} + \frac{3}{2}(L_{ss} + L_e \sin^2(\theta_r - \theta_0)) & 0 \\ 0 & 0 & L_{ls} \end{bmatrix} \tag{3.78}$$

Where:

$$L_e = -\frac{\pi \mu_0 l r A_1^2}{8 g_0 A_0} \left[\frac{N_e}{P_p}\right]^2 \tag{3.79}$$

$$L_{ss,q} = L_{rr,q} = \frac{\pi \mu_0 l r}{4 g_0} \left[\frac{N_e}{P_p}\right]^2 \;\; and \;\; L_{ss,d} = L_{rr,d} = \frac{\pi \mu_0 l r}{4 g_0 \zeta} \left[\frac{N_e}{P_p}\right]^2 \qquad (3.80$$

In the same way, $L_{sr,qd}^{SE}$, $L_{rs,qd}^{SE}$, and $L_{r,qd}^{SE}$ are calculated as:

$$L_{sr,qd}^{SE} = K_s \, L_{sr}^{SE} \, K_r^{-1} \tag{3.81}$$

$$= \begin{bmatrix} \frac{3\pi A_0 \mu_0 N_e^2 l r}{8 g_0 P_p^2} - \frac{3\pi A_1^2 \mu_0 N_e^2 l r \, cos^2(\theta_r - \theta_0)}{16 A_0 g_0 P_p^2} & -\frac{3\pi A_1^2 \mu_0 N_e^2 l r \, sin(2(\theta_r - \theta_0)}{32 A_0 g_0 P_p^2} & 0 \\ -\frac{3\pi A_1^2 \mu_0 N_e^2 l r \, sin(2(\theta_r - \theta_0)}{32 A_0 g_0 P_p^2} & \frac{3\pi \mu_0 N_e^2 l r (A_1^2 \sin^2(\theta_r - \theta_0) \; - \; 2A_0^2)}{16 A_0 g_0 \zeta P_p^2} & 0 \\ 0 & 0 & 0 \end{bmatrix} \tag{3.82}$$

$$= \begin{bmatrix} \frac{3}{2}(L_{sr} + L_e \cos^2(\theta_r - \theta_0)) & \frac{3}{2}L_e \cos(\theta - \theta_0)\sin(\theta_\mathrm{r} - \theta_0) & 0 \\ \frac{3}{2}L_e \cos(\theta_\mathrm{r} - \theta_0)\sin(\theta_\mathrm{r} - \theta_0) & \frac{3}{2}(L_{sr} + L_e \sin^2(\theta_r - \theta_0)) & 0 \\ 0 & 0 & 0 \end{bmatrix} \tag{3.83}$$

$$L_{rs,qd}^{SE} = \left(L_{sr,qd}^{SE}\right)^T \tag{3.84}$$

$$L_{r,qd}^{SE} = K_r\, L_{rr}^{SE}\, K_r^{-1} \tag{3.85}$$

$$= \begin{bmatrix} L_{lr} + \frac{3\pi A_0 \mu_0 N_e^2 lr}{8 g_0 P_p^2} - \frac{3\pi A_1^2 \mu_0 N_e^2 lr\, cos^2(\theta_r - \theta_0)}{16 A_0 g_0 P_p^2} & -\frac{3\pi A_1^2 \mu_0 N_e^2 lr\, sin(2(\theta_r - \theta_0)}{32 A_0 g_0 P_p^2} & 0 \\ -\frac{3\pi A_1^2 \mu_0 N_e^2 lr\, sin(2(\theta_r - \theta_0)}{32 A_0 g_0 P_p^2} & L_{lr} + \frac{3\pi \mu_0 N_e^2 lr(A_1^2 \sin^2(\theta_r - \theta_0) \; - \; 2A_0^2)}{16 A_0 g_0 \zeta P_p^2} & 0 \\ 0 & 0 & L_{lr} \end{bmatrix} \tag{3.86}$$

$$= \begin{bmatrix} L_{lr} + \frac{3}{2}(L_{rr} + L_e \cos^2(\theta_r - \theta_0)) & \frac{3}{2}L_e \cos(\theta_r - \theta_0)\sin(\theta_r - \theta_0) & 0 \\ \frac{3}{2}L_e \cos(\theta_r - \theta_0)\sin(\theta_r - \theta_0) & L_{lr} + \frac{3}{2}(L_{rr} + L_e \sin^2(\theta_r - \theta_0)) & 0 \\ 0 & 0 & L_{lr} \end{bmatrix} \tag{3.87}$$

Therefore, under a static eccentricity condition, the inductance matrices will have the following form:

$$\begin{bmatrix}\lambda_{sq}\\ \lambda_{sd}\\ \lambda_{s0}\\ \lambda'_{rq}\\ \lambda'_{rd}\\ \lambda'_{r0}\end{bmatrix}=\begin{bmatrix}L^{SE}_{s,qd0} & L^{SE}_{sr,qd0}\\ \\ {L^{SE}}_{rs,qd0} & L^{SE}_{r,qd0}\end{bmatrix}\begin{bmatrix}i_{sq}\\ i_{sd}\\ i_{s0}\\ i'_{rq}\\ i'_{rd}\\ i'_{r0}\end{bmatrix}+\begin{bmatrix}0\\ \lambda_m\\ 0\\ 0\\ \lambda'_m\\ 0\end{bmatrix} \tag{3.88}$$

3.7 Discussion and Conclusion

The mathematical modeling of the static eccentricity fault is presented in this chapter. The results obtained in (3.88) introduce mutual coupling between quadrature and direct axis fluxes under a static eccentricity condition. However, the transformation usually decreases the number of elements in the inductance matrices. In addition, the model includes the healthy condition, which results in decoupled flux equations. Therefore, this will be useful for faster calculation, and additionally reduces the modeling complexity. If a stationary reference frame is used to transform the inductance matrices, then the matrices become constants. However, this frame is not suitable for simulating the synchronous motors [70].

The control parameters A_0 and A_1 can be used to specify the degree of static eccentricity as well as to obtain the healthy model inductances. If the parameters A_1 and A_0 are set to zero and one, then this will lead to zero L_e and all the inductance matrices will represent the healthy case. In conclusion, the model of LSPMS motor under static eccentricity is governed by equation (3.26), (3.27), (3.31), (3.32), and (3.88).

CHAPTER FOUR

SIMULATION RESULTS OF THE PROPOSED MATHEMATICAL MODEL

4.1 Introduction

This chapter will present the simulation results of the mathematical model developed in chapter three using MATLAB^{TM}. In addition, a finite element analysis is performed to confirm the model accuracy.

4.2 Mathematical Model Simulation

Figure 4.1 presents the flow chart of modeling and simulation using MATLAB^{TM}. The simulation starts by determining the inductance matrices given in equation (3.78), (3.83), (3.84), and (3.87). Simulation is initialized for the 1-hp LSPMS motor with parameters, as shown in Table 4.1. Three phase sinusoidal voltages are applied to the motor terminals. By rearranging equation (3.11) and (3.15), the quadrature and direct fluxes are calculated after performing the integration. The calculated inductance matrices will be used to determine the current in qd0 reference frame using equation (3.88). From the fluxes and currents calculated, the electromagnetic torque, rotor angular position θ_r and speed ω_r are determined using equation (3.26) and (3.27). The performance of the LSPMS motor will be investigated under the normal operating loads. The selected degrees of static eccentricity (SE) based on equation (3.53) will be in the range of 13% to 40%. A small variation in the motor parameters under 10% SE is expected. This is due to intrinsic SE in the normal operation of the motor, which is estimated to be about 10% [23].

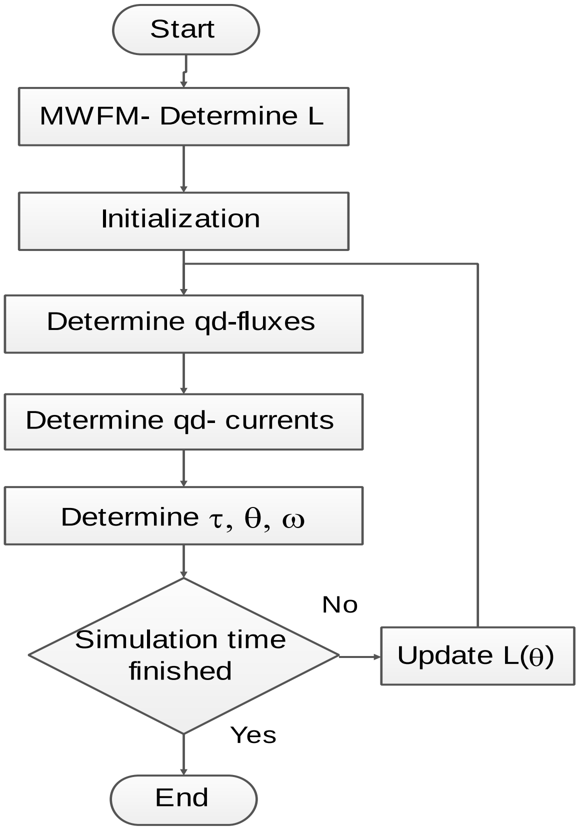

Figure 4.1: The flow chart of simulation process using MATLAB^{TM}.

Table 4.1: LSPMS motor specifications

Parameter	**Value**
Rated power (W)	750
Rated Voltage (V)	415
Stator phase resistance (Ohm)	19.15
Stator leakage inductance (mH)	0.001
Number of poles	4
Frequency (Hz)	50
Air-gap length (mm)	0.3
Outer/inner stator diameter (mm)	120/75
Number of stator/rotor slots	24/16
Axial length of stator core (mm)	72
Number of turns per slot	139
Height of stator yoke (mm)	45
Height of stator/rotor slots (mm)	13/9.5
Material of magnet	Recoma-24HE
Remanent of magnet (T)	1.02
Equivalent rotor resistance (ohm)	1.3295e-3
Inertia in equation of motion (kg/m^2)	0.00146

The MATLAB SIMULINK^{TM} of the developed mathematical model is shown in Figure 4.2, which includes the previously described steps in Figure 4.1.

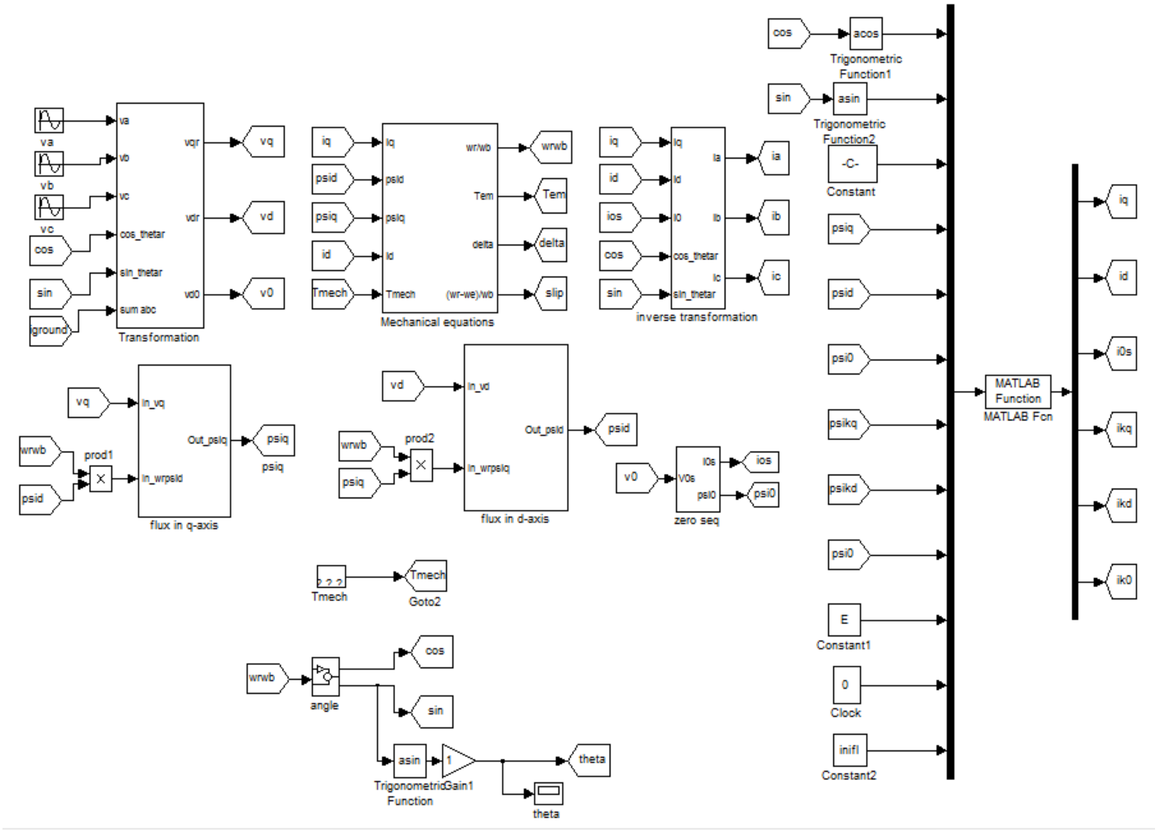

Figure 4.2: SIMULINK model of the developed mathematical model.

4.3 FEM Analysis

The finite element method is a numerically based approach used for computing the motor performance characteristics and parameters such as current, torque, speed, flux density, and inductances. This method will handle the complex motor geometry, consider the mixed set of materials involved in the motor parts, and in addition, monitor the non-linear behavior of these materials such as permanent magnets. In this method, the motor geometry will be divided into an enormous number of elements joined with nodes by using a proper discretization and mesh generation algorithms. A set of equations represents each element, and the entire set of equations and their solutions will implement the motor model.

JMAG^{TM} is an electromagnetic simulation program developed by the JSOL^{TM} corporation. JMAG^{TM} provide a 2D platform to construct the motor parts. The material properties can be assigned to each part in the motor model. The software uses the finite element method for simulating the motor behavior and the output response such as the line current, flux linkage, forces, and torque. JMAG^{TM} automatically constructs the most suitable mesh according to the type of each part and its position. Within each part, the field is approximated by unknown polynomial coefficients. The solution of these polynomials returns the solution of the problem.

JMAG^{TM} software includes JMAG EXPRESS^{TM}, JMAG SUPER EXPRESS^{TM}, and JMAG DESIGNER^{TM}. The level of problem complexity decides the software package to be used. JMAG EXPRESS^{TM} contains some common motor templates which can be used to generate basic characteristics. JMAG SUPER EXPRESS^{TM} further takes a predefined scenario for different types of analysis. JMAG DESIGNER^{TM} is considered to be the core program in the JMAG^{TM} software environment and will be used in this thesis. It allows a 2D and 3D electromechanical finite element analysis and design with numerous analysis tools such as parametric analysis, optimization, and scripting.

4.3.1 FEM Analysis using JMAG^{TM}

There are specific steps that should be followed in the FEM analysis using JMAG^{TM}, which are presented in Figure 4.3. First, the geometry model should be created. There are many ways to construct the geometry such as to build and import the model from AUTOCAD^{TM} or to build the geometry model in the JMAG^{TM} geometry editor.

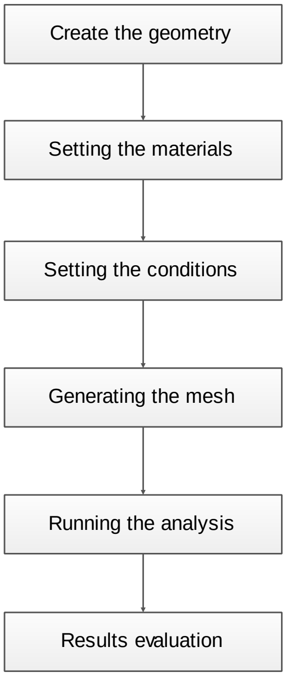

Figure 4.3: Basic FEM analysis flowchart.

The motor internal and external dimensions are obtained from the motor’s datasheet, which also includes the wiring diagrams and the motor dimensions as presented in the appendix. The model could be constructed in either a 2D or a 3D platform. However, a 2D simulation will save the time for an efficient simulation period. The next step is to set up the material type for each part in the model. For example, setting the magnet and the wires type. The third step is to set up the conditions and rules of the analysis, which includes the step time for the simulation, stator, and rotor circuit topologies, mesh type, rotation condition, and the motor static parameters. Finally, the analysis is performed, and results are obtained.

4.3.2 Create the Geometry Model

In this thesis, the geometric model is built and imported from AUTOCAD™, as shown in Figure 4.4. Consequently, the whole geometric model, as imported in JMAG™, is shown in Figure 4.5. A proper unit selection should be considered for accurate simulation. In our case, the selected units are millimeters for distance, Celsius for temperature, seconds for time, and Hertz for frequency.

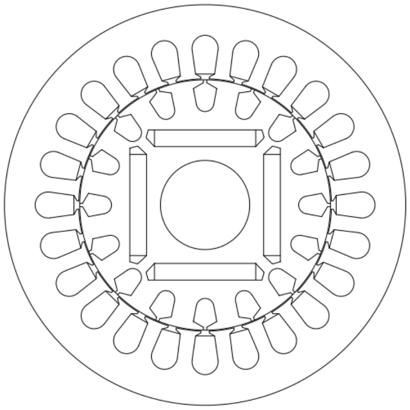

Figure 4.4: Geometry model in AUTOCAD™.

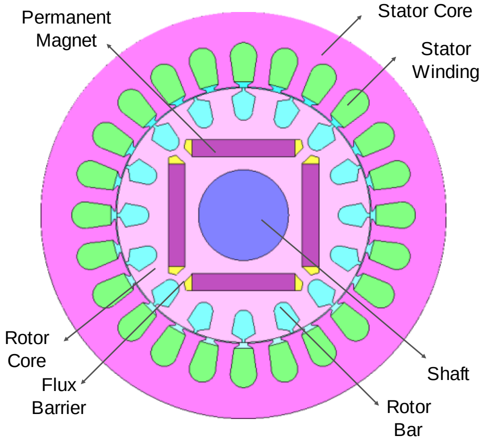

Figure 4.5: 2-D geometry model parts of LSPMS motor in JMAG™.

4.3.3 Setting the Materials

Once the geometry has been created and well assembled, the task is now to assign a material type to each part of the motor geometry. In the geometry model, each part is drawn separately. For example, the stator and rotor geometries can be edited alone without any connection. It is known that in the manufacturing process, the stator and rotor materials may differ from each other. Table 4.2 presents the materials assigned to each part, according to the motor datasheet.

Table 4.2: The Materials assigned to each motor part.

Component	**Material**
Stator Core	Stainless Steel
Stator lamination	50JN600 - Silicon Steel
Stator Coils	Copper
Rotor Magnets	Recoma-24HE
Rotor bars	Aluminum Al99.7
Rotor lamination	50JN600 - Silicon Steel
Shaft	Steel
Airgap	Air

The magnet materials have nonlinear behavior, and JMAG^{TM} databases can be used to define the magnetic material properties. Moreover, if the material properties are not available, then they can be defined as shown from the magnets datasheet in the appendix. Regarding the formulation of the coils, they are modeled in a single region, since the current flow in the coils is uniform.

4.3.4 Create the Circuit Model

Up to this point, the geometry model is created, and the materials are assigned. Each part should be linked to a circuit model to implement the electrical function. The stator coils are formed using the winding data shown in Table 4.3 and Table 4.4. Figure 4.6 represents the circuit implementation of a stator part in a star configuration. The line voltage is obtained from the nominal voltage provided in the motor datasheet.

Table 4.3: Stator winding parameters.

Parameter	**Value**
Slot connection	Series
Winding distribution	Sinusoidal
Layers	Monolayers chain
Slot pitch	1-6
Slot fill Factor	74.7%
wire	Round copper

Table 4.4: Stator parameters.

Stator phases		**Value**
A-phase	Number of Turns	139
	Resistance [Ohm]	19.1
B-phase	Number of Turns	139
	Resistance [Ohm]	19.1
C-phase	Number of Turns	139
	Resistance [Ohm]	19.1

Power Supply	Excitation	Three phase-AC
	Voltage [volt]	415
	Frequency [Hz]	50

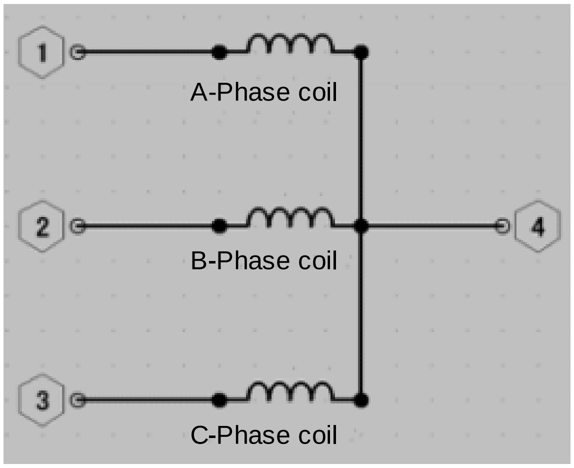

Figure 4.6: Stator winding circuit.

The rotor circuit is created using FEM conductors and resistors, as shown in Figure 4.7. The FEM conductors represent the bars inductance and the resistance. Table 4.5 indicates the rotor parameters used in this circuit.

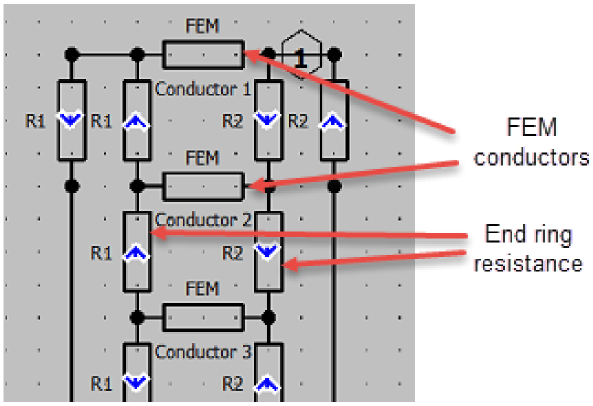

Figure 4.7: Part of rotor circuit representation.

Table 4.5: Rotor circuit parameters.

Parameter	Value
Number of slots	16
Leads type	Aluminum – AL.99.7
End ring size	60 mm^2

4.3.5 Setting the Conditions

In JMAG, eight conditions must be specified for successful simulation. They are explained in the appendix.

4.3.6 Mesh Generation

To simulate the model with the finite element method, JMAG^{TM} generates the most suitable mesh for each part of the model. JMAG^{TM} provides many types of meshes. For example, there is the automatic mesh type, which recognizes the model shape and automatically generates the most accurate mesh. This will include the geometry and the airgap region. On the other hand, the adaptive mesh that uses the analysis results to optimize the mesh selection and generation will be used, in this model, to generate the meshes for the whole model. The 2-D mesh model of the motor is created with 70,729 nodes and 133,803 elements. Figure 4.8 shows the resulting mesh model of LSPMS motor.

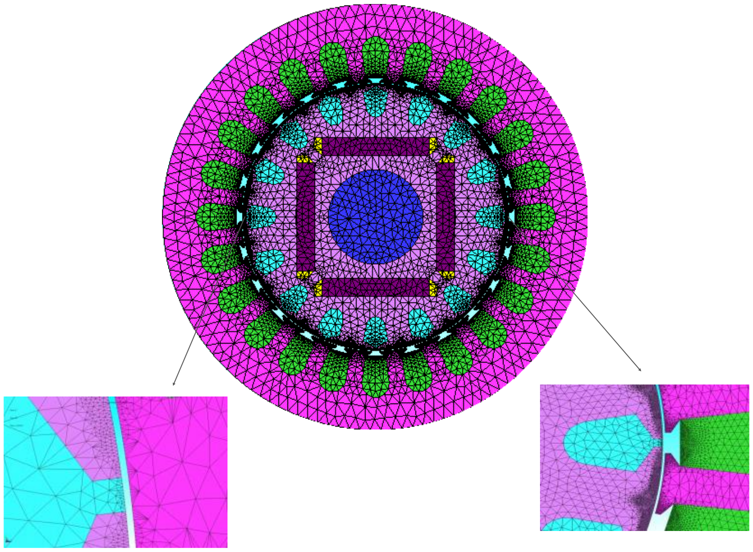

Figure 4.8: 2-D mesh model of LSPMS motor.

4.3.7 Solving the Model

FEM based analysis is performed for the three phase LSPMS motor (750 W, 415 V, Y-connected, four-pole) utilizing JMAG^{TM} designer software. The motor geometry specifications and electrical parameters are shown in Table 4.1. Figure 4.5 presents the geometry model of the motor. The model consists of all the geometrical parts, which include the laminated silicon steel core of the stator and rotor, stator copper windings, shaft, rotor casts aluminum bars, and the permanent magnet of type 24HE. The monolayer topology is used for stator winding distribution, and this will reduce the total harmonics in the line voltage and current. The transient iterative solver of JMAG^{TM}, based on an incomplete Cholesky conjugate gradient (ICCG) method, is used to solve the magnetic field distribution in the model, as well as the other motor performance characteristics such as stator current, speed, torque.

4.4 Comparison Between JMAG^{TM} and MATLAB^{TM} Results

The simulation results will be divided into two main parts. First, a comparison between the simulation results of the MATLAB^{TM} and JMAG^{TM} is presented under healthy conditions. The second part will contain the simulation results under static eccentricity fault conditions. This section will include a simulation and comparison of 21 cases using JMAG^{TM} and MATLAB^{TM}. They will cover a wide range of eccentricity degrees under different loading conditions. Also, the angle effect of the static eccentricity vector along the motor circumference has been studied. The simulation results will be compared in terms of stator current, speed, and torque characteristics.

4.4.1 Simulation Results under Healthy Condition

The simulation of the healthy LSPMS motor using JMAG^{TM} and MATLAB^{TM} shows that the maximum starting torque capability of this motor is 2.9 N.m. Figure 4.9 to Figure 4.11 present the simulated stator current, electromagnetic torque, and speed characteristics of the healthy motor under no load. Many observations should be noticed, such as the similarity of time variation between the JMAG^{TM} and MATLAB^{TM} results. The stator current shows very similar time variations in transient and steady state operation. Moreover, the torque and speed characteristics of the developed mathematical model follow the same behavior of the FEM simulation in a steady state, with the same trend in the transient region. For further comparison, Figure 4.12 to Figure 4.17 depict the same results under a load of 1.5 N.m and 2.1 N.m, respectively.

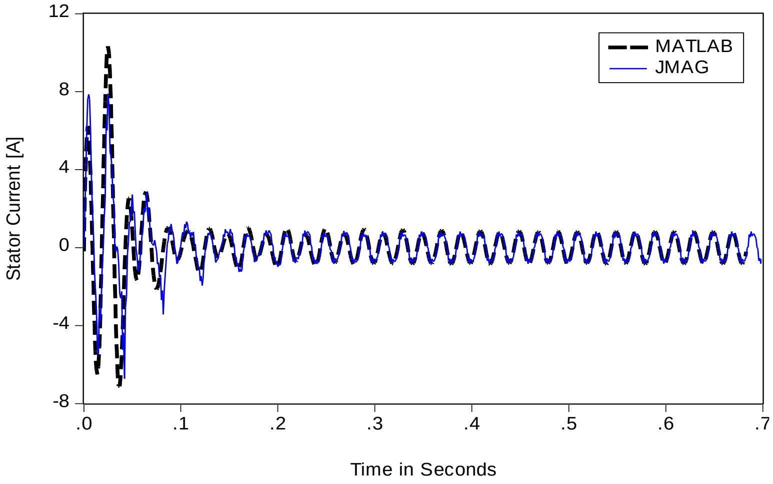

Figure 4.9: Stator Current under healthy condition (No load).

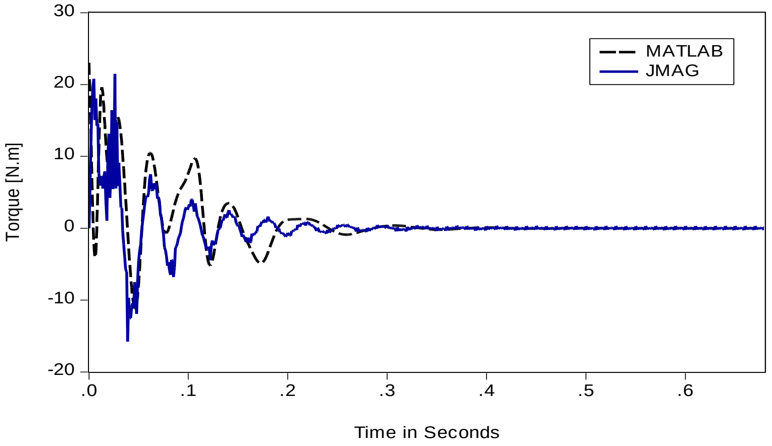

Figure 4.10: Torque characteristic under healthy condition (No load).

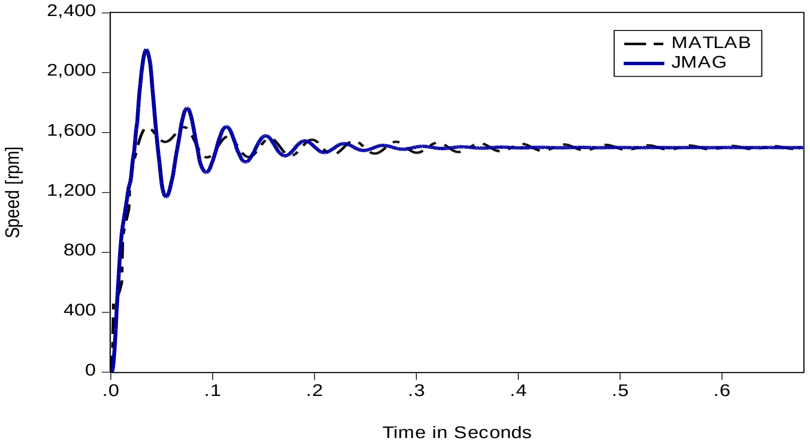

Figure 4.11: Speed characteristic under healthy condition (No load).

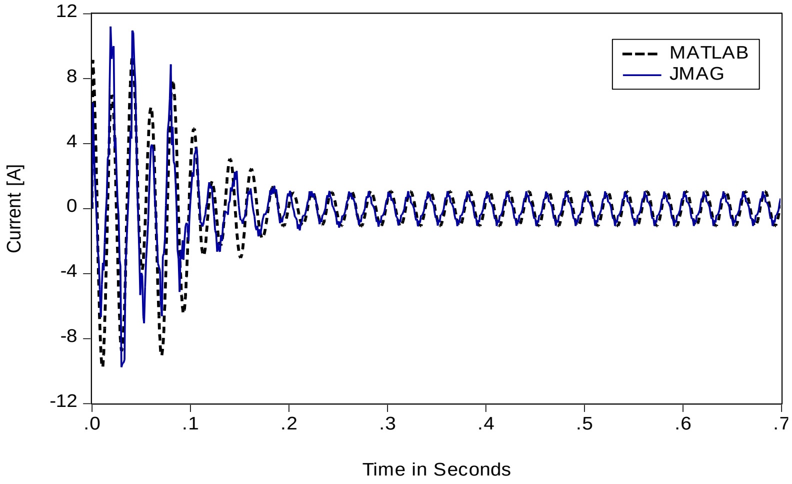

Figure 4.12: Stator current under healthy condition (1.5 N.m)

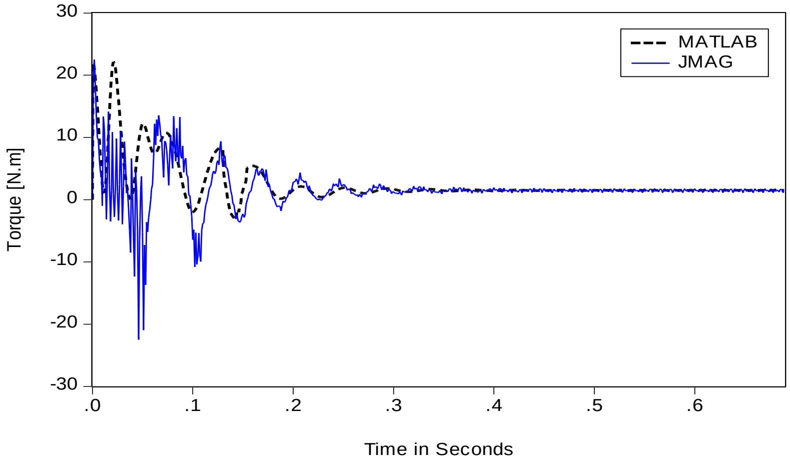

Figure 4.13: Torque characteristic under healthy condition (1.5 N.m)

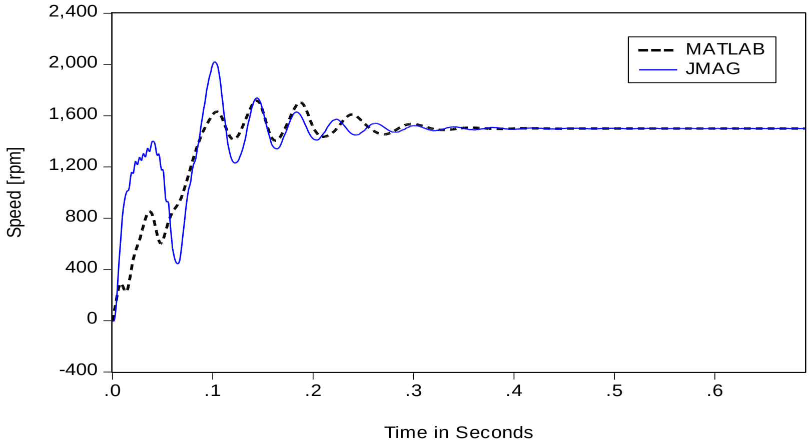

Figure 4.14: Speed characteristic under healthy condition (1.5 N.m)

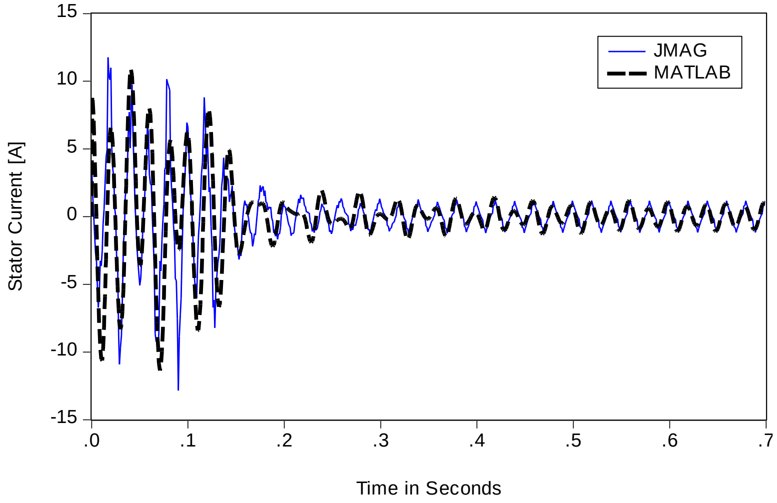

Figure 4.15: Stator Current under healthy condition (2.1 N.m)

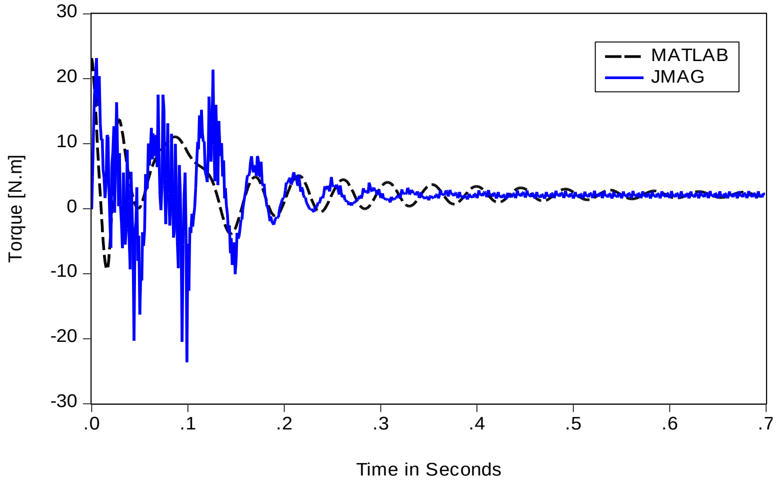

Figure 4.16: Electromagnetic torque under healthy condition (2.1 N.m)

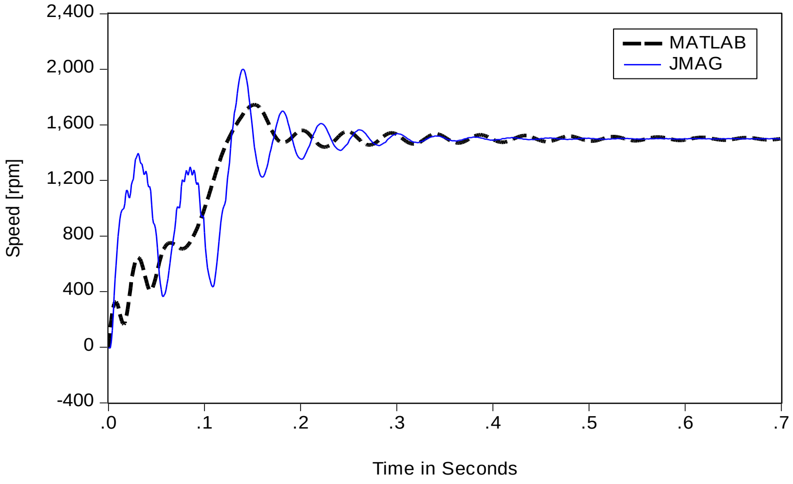

Figure 4.17: Speed under healthy condition (2.1 N.m)

It can be concluded that the results obtained from the developed mathematical model under the healthy conditions are in fine agreement with the FEM results. Besides, the stator current time variations in both results are close to each other. However, some deviations in the speed and torque characteristics have occurred. The reasons for this deviation will be discussed at the end of this chapter. To investigate the load effects on the performance of the LSPMS motor, Figure 4.18 to Figure 4.20 present the motor line current, speed, and torque under a load of 0 N.m, 1.5 N.m, 2 N.m, 2.5 N.m, and 2.9 N.m.

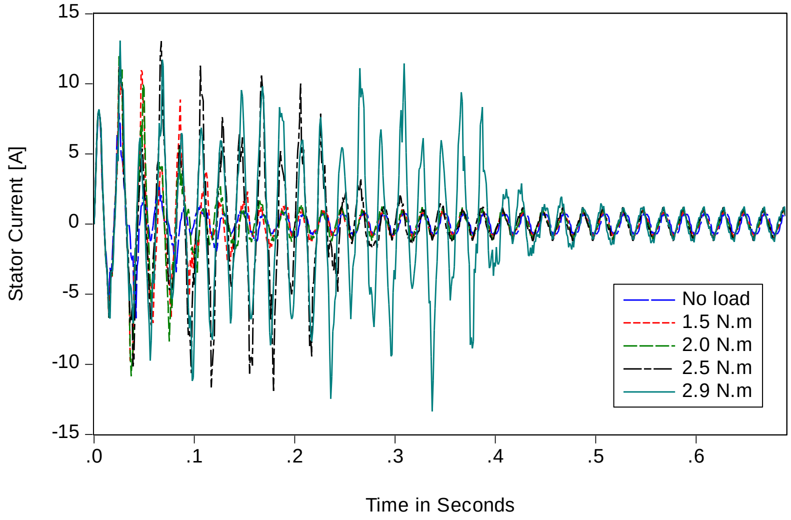

Figure 4.18: Stator current under different loading conditions

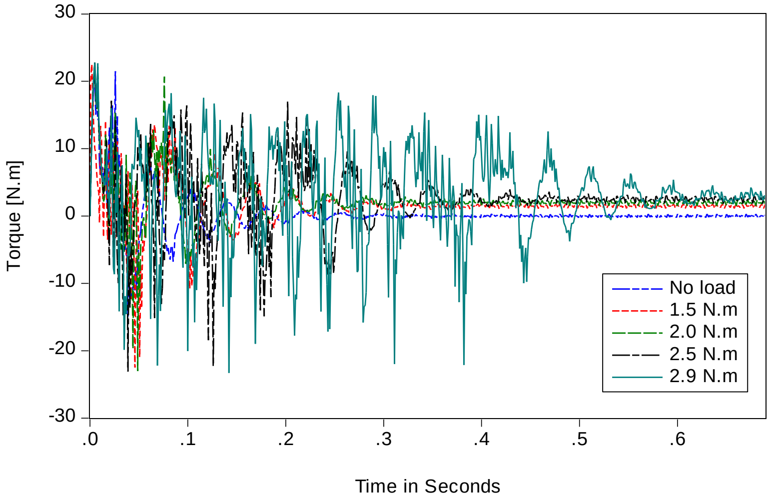

Figure 4.19: Electromagnetic torque under different loading conditions

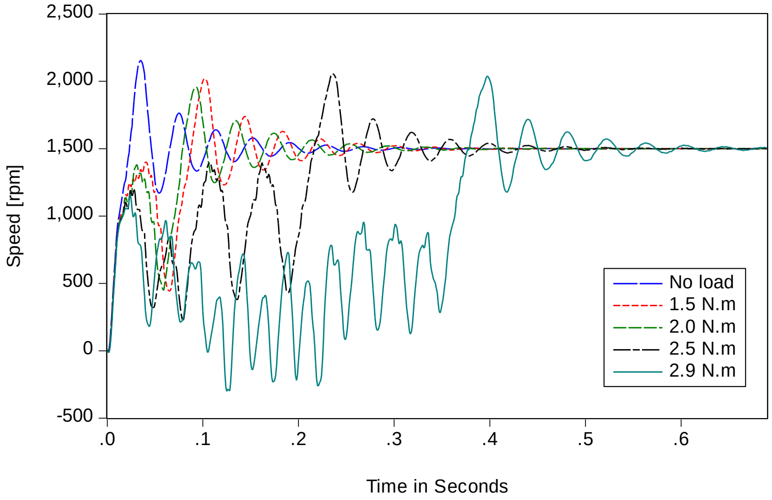

Figure 4.20: Speed under different loading conditions

It is obvious that the motor synchronization time significantly increases for higher loads. Furthermore, if the load value is higher than 2.9 N.m, the motor loses the ability to start.

4.4.2 Simulation Results under Static Eccentricity Fault Condition

This part will show the simulation results of the developed mathematical model and FEM under the static eccentricity (SE) fault condition using JMAG^{TM} and MATLAB^{TM}. In addition, the degree of static eccentricity at which the motor will lose the ability to start has been introduced. Finally, the effects of the minimum airgap positions are also presented. Figure 4.21 to Figure 4.23 depict the stator current, electromagnetic torque, and speed characteristics under 19 % static eccentricity and 2.1 N.m load. The similarity of time variations between MATLAB^{TM} and FEM results are clearly shown. Comparing these results with the healthy case in Figure 4.15 to Figure 4.17, the differences between each set of figures clarify the effects of SE on LSPMS motor.

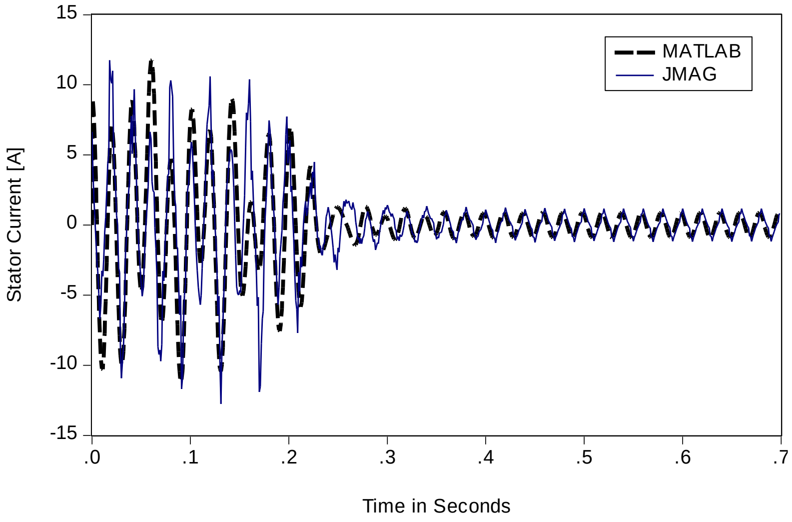

Figure 4.21: Stator Current under faulty condition (2.1 N.m-19% SE)

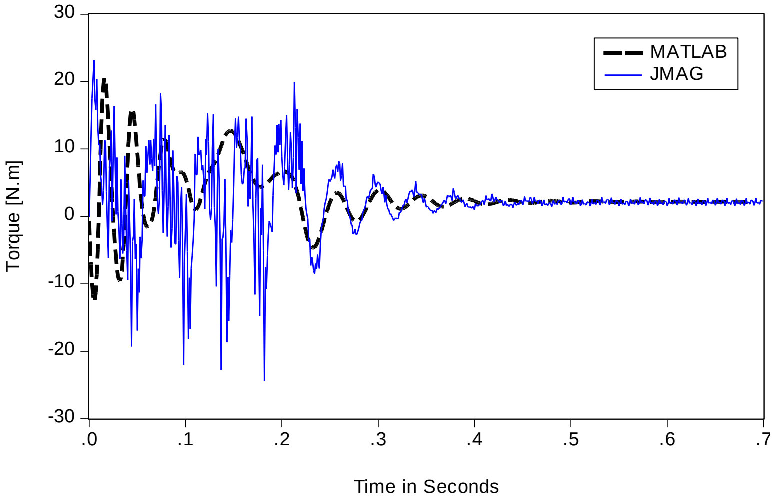

Figure 4.22: Electromagnetic torque under faulty condition (2.1 N.m-19% SE)

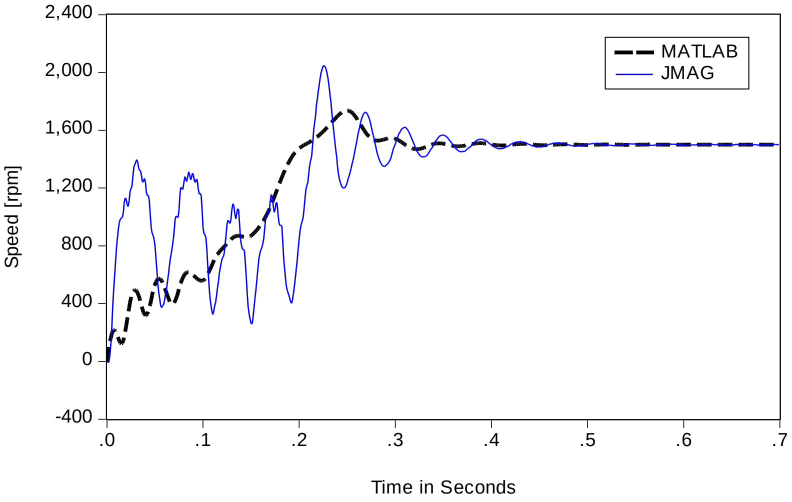

Figure 4.23: Speed under faulty condition (2.1 N.m-19% SE)

To show the effects of SE on the line current, Figure 4.24 shows a comparison between the healthy and faulty cases under 19% SE. Under this degree of SE, it takes a longer time to attain a steady state than a healthy condition under the same level of load. Also, higher current peaks are presented in the transient region.

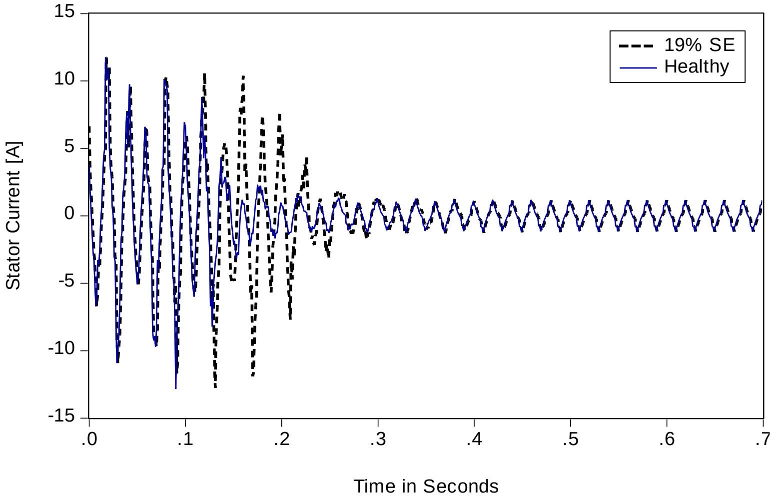

Figure 4.24: Stator current under healthy and faulty conditions (2.1 N.m-19% SE)

Under different levels of static eccentricity, the stator current, speed, and torque characteristics have different behaviors compared to the healthy state. For a load of 2.1 N.m, Figure 4.25, Figure 4.26, and Figure 4.27 depict the time variation of stator current, speed, and torque under the healthy condition (0 % SE), 13 % SE, 16 % SE, and 19 % SE. In this case, as the eccentricity level increases, the synchronization time is also increased. A slight difference is shown in the results between the healthy and 13% static eccentricity condition. However, more peaks, ripples, and longer synchronization time are observed for 16% and 19% static eccentricity before reaching the steady state region. The same observations are noticed for electromagnetic torque and speed characteristics.

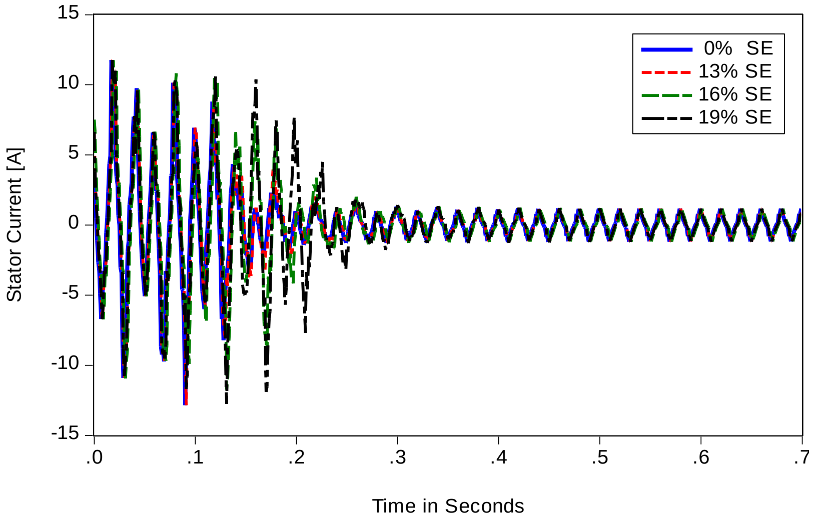

Figure 4.25: Stator Current under different values of SE (2.1 N.m)

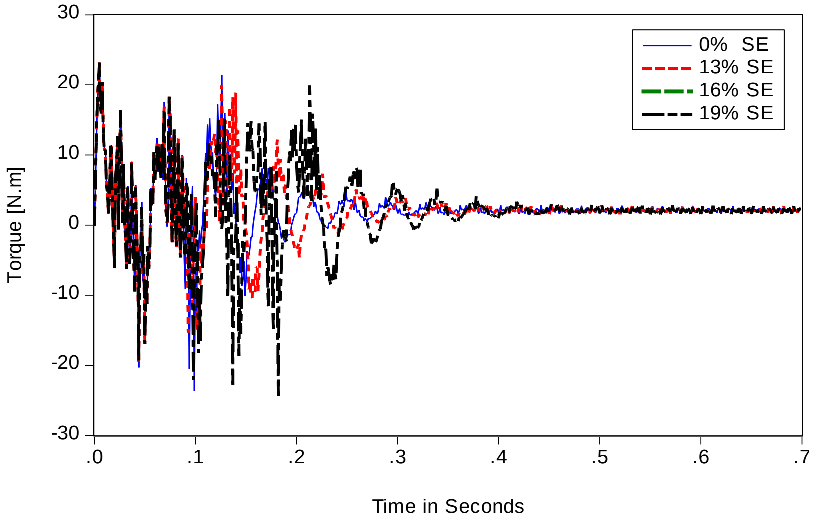

Figure 4.26: Electromagnetic torque under different values of SE (2.1 N.m)

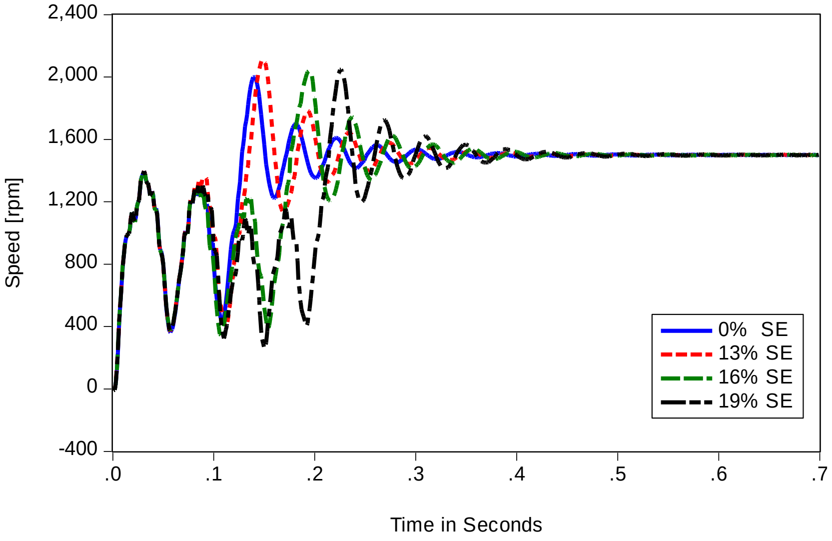

Figure 4.27: Speed under different values of SE (2.1 N.m)

The degree of static eccentricity at which the motor is going out of synchronism is important to be specified. Figure 4.28, Figure 4.29, and Figure 4.30 depict the line current, electromagnetic torque, and speed characteristics under maximum starting load and for different levels of SE. When the degree of SE reaches 17%, the motor loses the ability to start and the overall performance deteriorates.

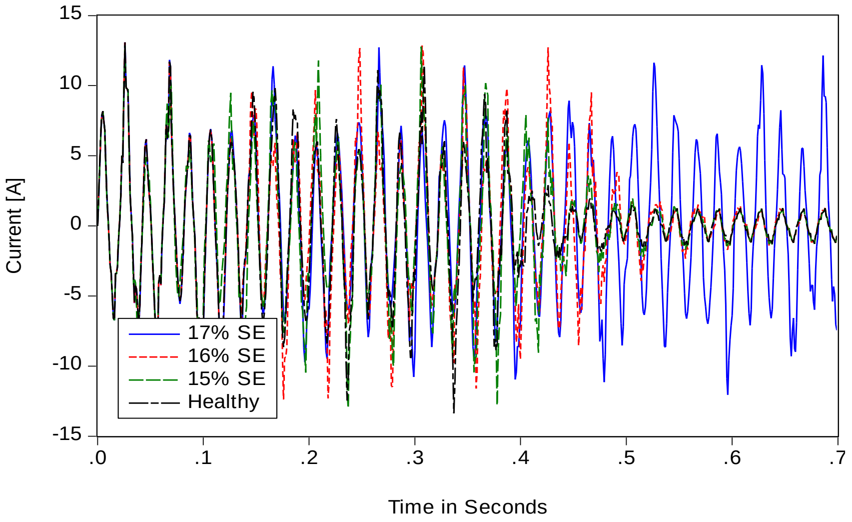

Figure 4.28: Stator Current under different degrees of SE (2.9 N.m).

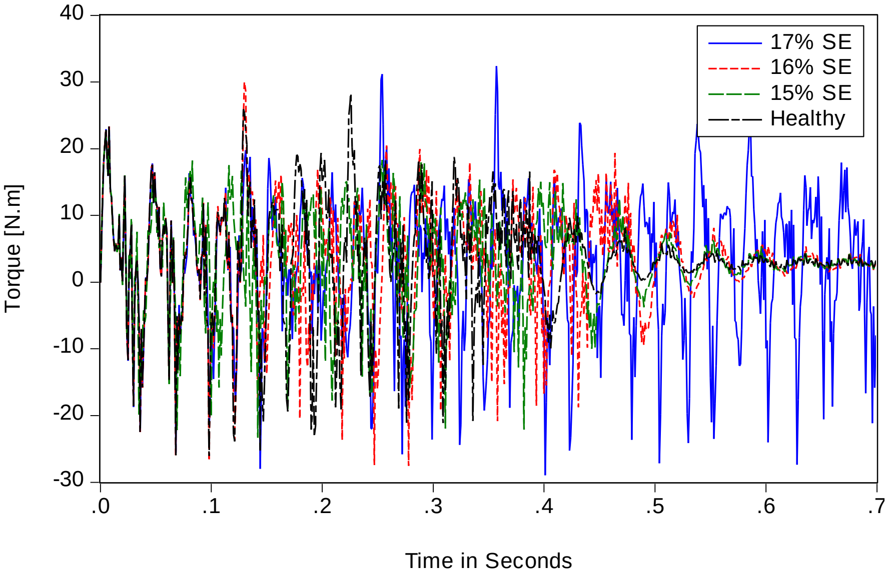

Figure 4.29: Electromagnetic torque under different degrees of SE (2.9 N.m).

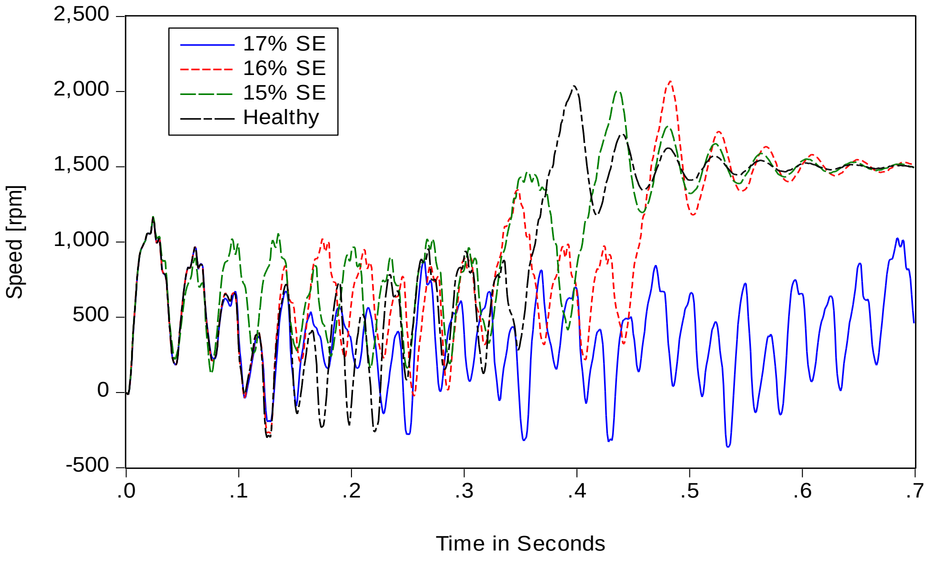

Figure 4.30: Speed current under different degrees of SE (2.9 N.m).

For further comparison between FEM and the developed mathematical model results, Table 4.6 presents the correlation and the normalized mean square error (NMSE) for 21 cases of different loading conditions and static eccentricity degrees. For each case, the correlation and NMSE are calculated to qualify the obtained results for stator current. It is useful to pay more attention to the stator current, which is an important indicator of fault occurrence. Fault diagnostic techniques, such as MCSA, are based on the stator current waveform, and this model has a direct application to MCSA as will be explained later in chapter five.

The correlation coefficient is a statistical measure of dependence between two variables, and is also an indicator of how two variables fluctuate together. A positive correlation indicates that both signals increase and decrease in parallel, while a negative value indicates an opposite behavior. The percentage of NMSE is calculated based on equation (4.89) while the correlation coefficient is calculated using Excel^{TM}. These indicators are depicted in Figure 4.31 as a percentage. The correlation has higher values at lighter loads with smaller values of NMSE. The correlation of the first case, which corresponds to the no load condition in Table 4.6, is 0.823 and the NMSE is 0.8%, which reflects the fine agreement between FEM and the developed mathematical model results under this condition. Also, the stator current for case 3 is depicted in Figure 4.32. It can be noticed that slight effects of SE are observed on lighter loads. For higher loads, the values of the correlation are slightly decreasing.

Table 4.6: The Correlation and NMSE of simulated cases

Case Number	Load N.m	δ_s %	Correlation%	NMSE%
Case 1	0	0	82.3	0.8
Case 2		16	83.1	0.7
Case 3	1.5	0	81.5	2.1
Case 4		16	83.7	2.0
Case 5		22	80.3	2.3
Case 6	2	0	81.6	2.4
Case 7		16	80.0	2.4
Case 8	2.1	0	76.0	2.6
Case 9		13	76.3	3.1
Case 10		19	75.0	3.5
Case 11		30	76.2	3.2
Case 12	2.2	0	77.4	3.2
Case 13		13	76.8	3.1
Case 14		16	70.0	3.8
Case 15	2.3	0	80.1	3.2
Case 16		18	74.1	4.1
Case 17		30	79.0	3.4
Case 18		33	77.1	3.7
Case 19	2.4	0	75.0	3.5
Case 20		16	70.0	4.1
Case 21		33	75.0	3.2

$$\%NMSE = \frac{\sum_{i=1}^{N}\left(\left(\frac{X_i}{Max(x)}\right) - \left(\frac{X_i'}{Max(x')}\right)\right)^2}{N} \times 100\ \% \tag{4.89}$$

Where $\frac{X_i}{Max(x)}$ and $\frac{X_i'}{Max(x')}$ are the JMAG^{TM} and MATLAB^{TM} stator current time variation values divided by the maximum value of each time series, respectively. N is the number of samples per each series.

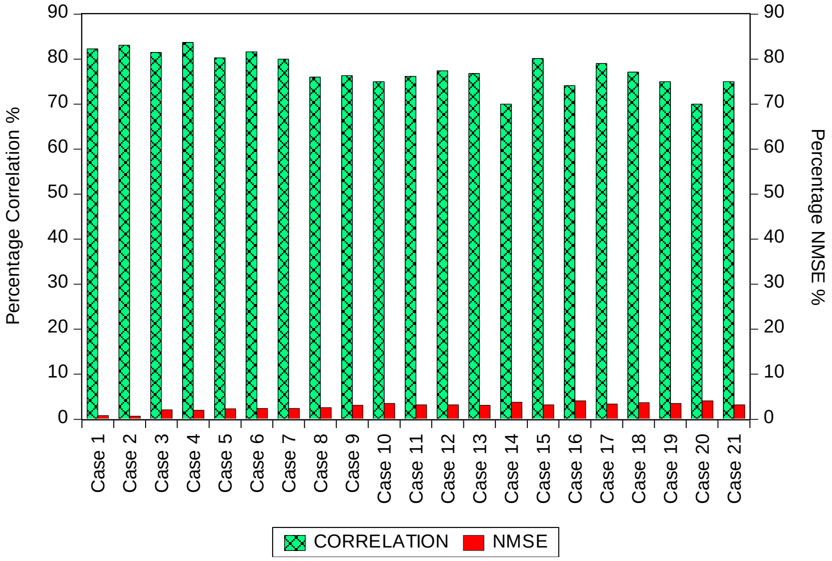

Figure 4.31: The correlation and NMSE of the simulated cases.

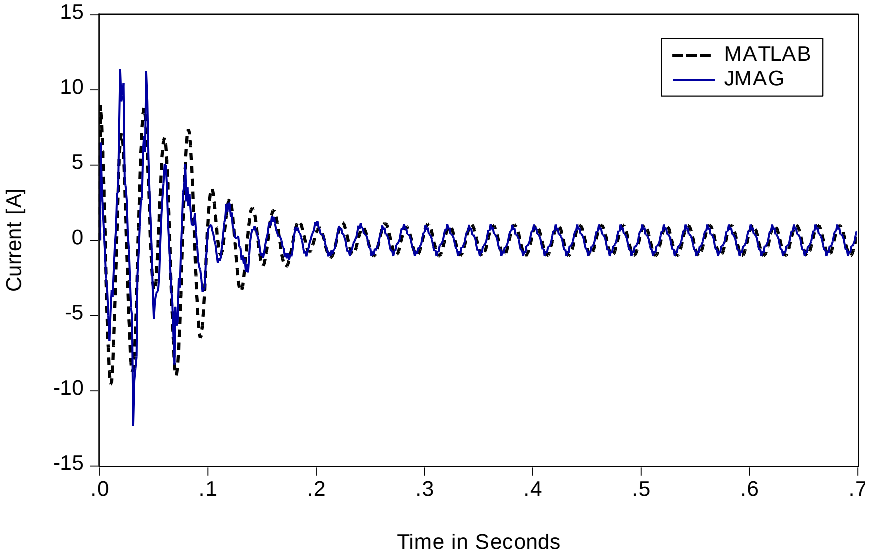

:

Figure 4.32: Stator current under 16%SE (1.5 N.m)

Consequently, Figure 4.33 presents case 21 for the stator current with a correlation of 75 % and NMSE of 3.2 %. In general, Table 4.6 shows a very similar behavior between JMAG^{TM} and MATLAB^{TM} simulation results. The average value of the NMSE and correlation over the 21 cases are 2.87% and 78%, respectively. In the previous discussion, Case 10 was selected for comparison purposes, and has nearly the same average value of the indicators.

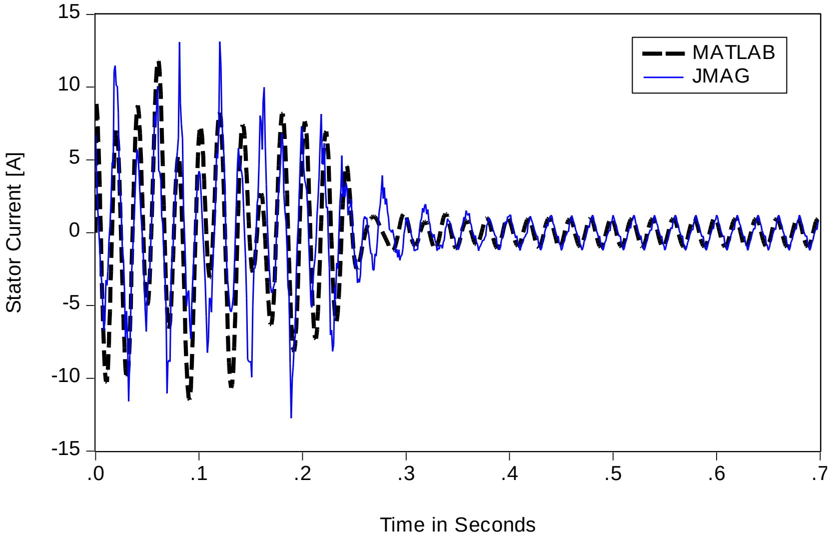

Figure 4.33: Stator current under 33%SE (2.4 N.m).

Previous simulated cases are performed while considering the initial angle of the static eccentricity vector equal to zero (θ_0=0). However, Figure 4.34 compares the results obtained from the developed model and FEM simulation by considering an arbitrary angle $\theta_0 = 45^o$ for a load of 2.1 N.m. It is obvious that the synchronization time, in this case, is longer than the healthy state and smaller than the faulty condition when θ_0=0. This indicates that the synchronization time under this fault is a function of the static eccentricity degree, as well as, the angle of the static eccentricity vector. To verify this observation,

Figure 4.35 shows the time variations of stator current for the same level of static eccentricity and under different angles for static eccentricity vector. The slight difference occurs for higher angles and the effects became clearer as the angle decreases. The synchronization time is increased with higher peaks in the stator current.

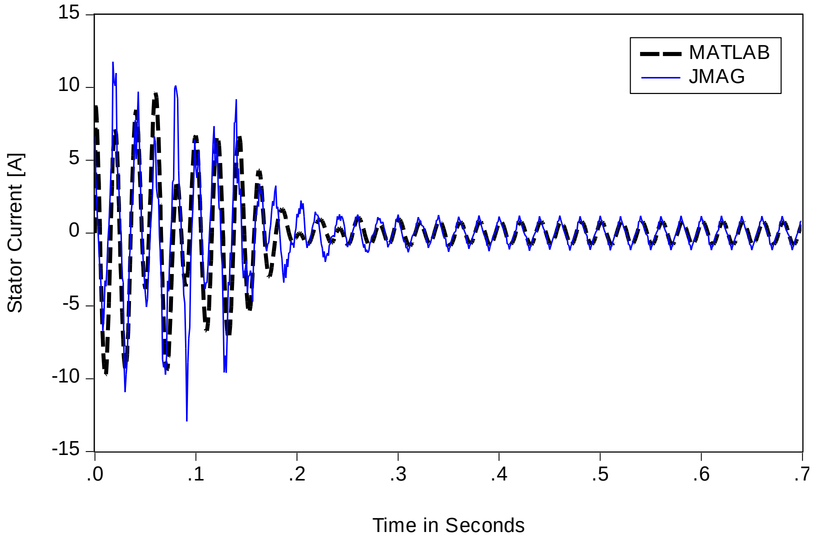

Figure 4.34: Stator Current under faulty condition for $\theta_0 = 45^o$.

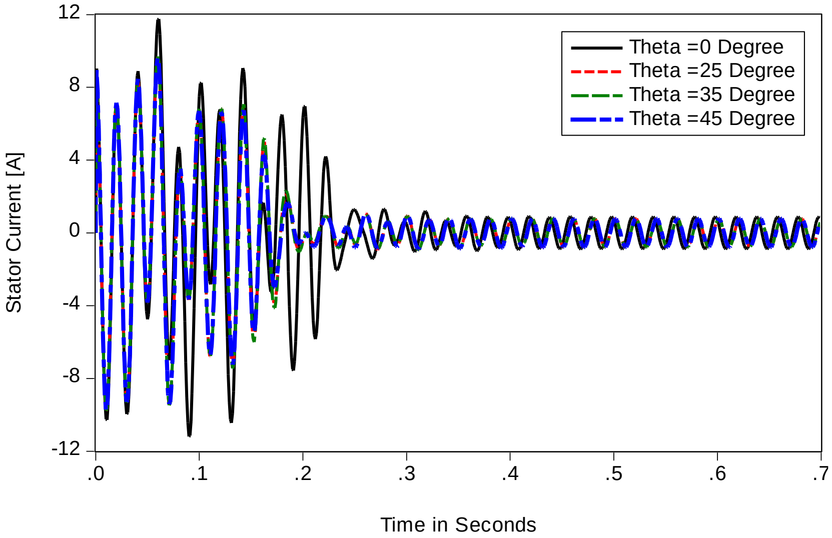

Figure 4.35: Stator Current under faulty condition for different values of θ_0

4.5 Discussion and Conclusion

In conclusion, the results obtained in this chapter for the developed mathematical model under static eccentricity conditions follow the same trend as the FEM simulation results. However, some deviations are noticed between JMAG^{TM} and MATLAB^{TM} in the stator current, torque, and speed characteristics over the transient period. There are many attributes for this behavior: firstly, unlike the MWFM, FEM analysis pays more attention to the material effects on each motor part, such as the material of the stator and rotor cores, laminations, permanent magnets and so on. This will essentially include the nonlinear behavior of these materials. In addition, the operating point of rotor permanent magnets is assumed to have a fixed value. However, this operating point is a function of the load as reported in [73]. Besides, the moment of inertia is assumed to have a constant value. It was observed from the FEM simulation that the moment of inertia changes for each degree of static eccentricity, since the motor geometry has been changed under the eccentricity condition. Finally, the mathematical model assumes an approximation of three phase distribution of the rotor circuit, which will have some effects on the electromagnetic torque and speed characteristics in the transient region, with no effect on the steady state operation.

CHAPTER FIVE

NEURAL NETWORK BASED STATIC ECCENTRICITY DETECTION ALGORITHM

5.1 Introduction

The process of protecting motors against faults has become more essential, especially in industrial sectors with high power ratings, in addition to the higher operating costs of these motors. Digital signal processing and the revolution in artificial intelligence have allowed advances in motor protection. Fault diagnostics can be implemented in an online monitoring system by utilizing sensors that will offer the monitoring signal to the motor controller, and a decision about the fault occurrence can be made.

The process of continuous monitoring, in addition to accessibility, are the main challenges in fault diagnosis, especially for critical motor applications such as huge oil pumps or nuclear cooling pump motors. Accessibility is a hard task, under those circumstances, so an efficient method for fault diagnostics has become more essential. Line current analysis is one of the best fault diagnostic methods which enhance the accessibility, and can be used in online monitoring systems [27].

In the case of a static eccentricity fault, the air gap distance is nonuniform. This will inject harmonics in the line current. Thus, this will affect the time variation of the stator current and the synchronization process of the LSPMS motor, as shown in the previous chapter. Moreover, these variations can be detected and used as patterns to reveal the fault occurrence. Artificial neural networks are able to learn these patterns and decide the motor state.

5.2 Artificial Neural Networks

Artificial Neural networks (ANNs) are inspired based on biological networks in the human body. The development of this method came from the desire of producing artificial systems which perform intelligent functions in the same way as a human brain. A neural network differs from computational analysis, as computers have some sort of learning algorithms and training rules, with a capability of extending results beyond the trained data. In addition, there is no need for an explicit description of the problem being processed. In the training process, the neural network adapts itself to map the desired output to the input data. This method has a lot of applications, which include mainly classification and function approximation problems [74].

The biological neuron consists of terminal buttons which are connected to a huge number of other neurons across a gap called a synapse. The neuron has many dendritic trees; each tree will sum the weighted information being received from other neurons.

Mathematically, the neuron is implemented with simple algebraic equations [74]. Figure 5.1 represents an elementary neuron with input vector X and output Y. Each input is weighted by an appropriate weight w. In addition, a bias B will be added to the total sum, while an activation function F is used to generate the output.

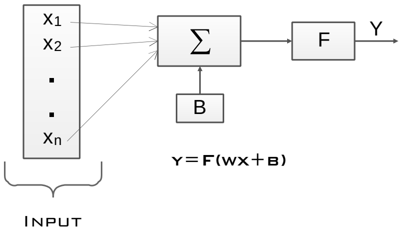

Figure 5.1: Basic structure of neuron.

Consequently, a series of N neurons will create a single layer in the network. Figure 5.2 presents the detailed layer topology and its equivalent notation.

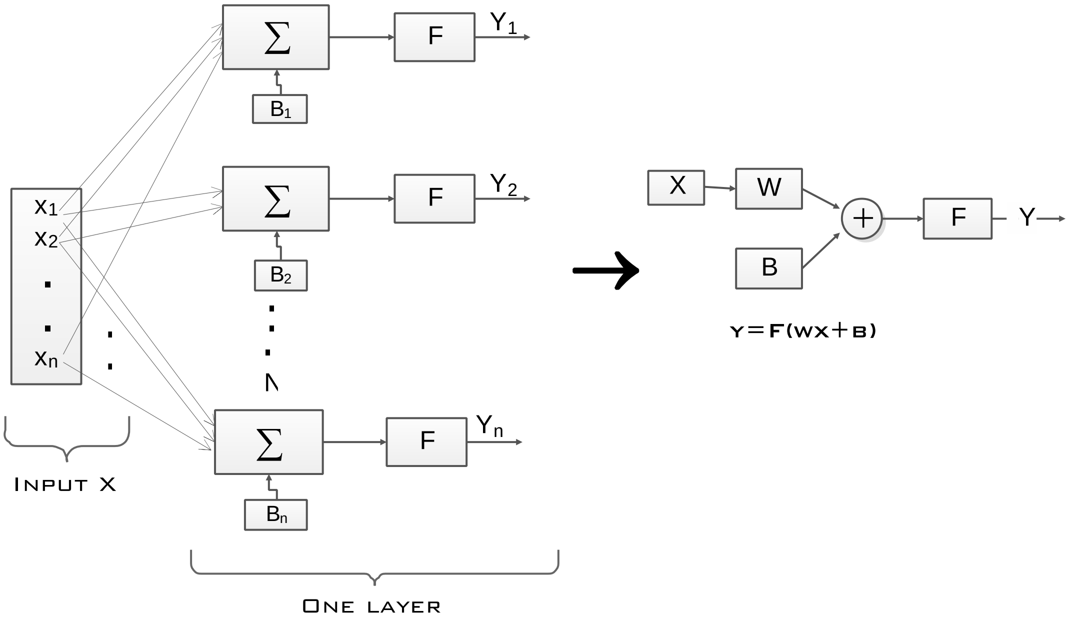

Figure 5.2: A single layer in neural networks.

5.2.1 Multilayer Feedforward Neural Networks

The feedforward neural networks (FFNNs) are used for any input-output mapping problem. As shown in Figure 5.3, it consists of a series of layers. The first one will receive the input vector X, while the output layer will produce the network's output. There are some special FFNNs developed for specific applications such as patterns recognition and function approximation [75].

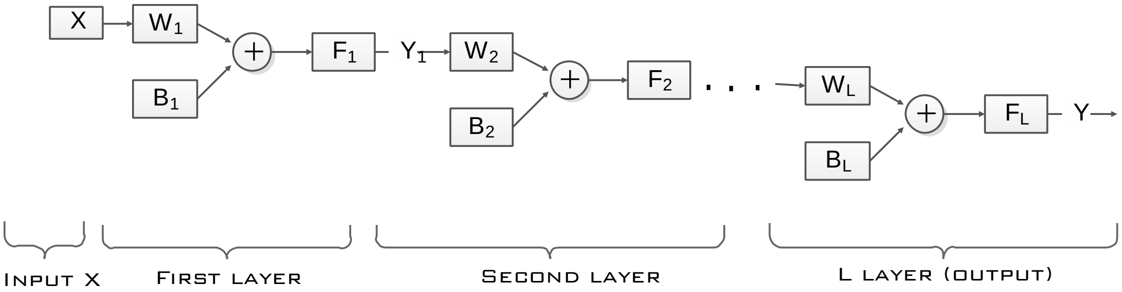

Figure 5.3: Multilayer neural network.

5.2.2 Learning Methods

The supervised and the unsupervised methods are the general learning algorithms in neural networks. In the unsupervised learning, only the inputs are presented in the training process. However, in the supervised method, as shown in Figure 5.4, the input X and the desired output y are presented. The generated output y' is compared to the desired output to calculate the error and propagate it back through the network. Moreover, the weights are adjusted to increase the accuracy. An example of this method is the multilayer feedforward neural network with backpropagation [74].

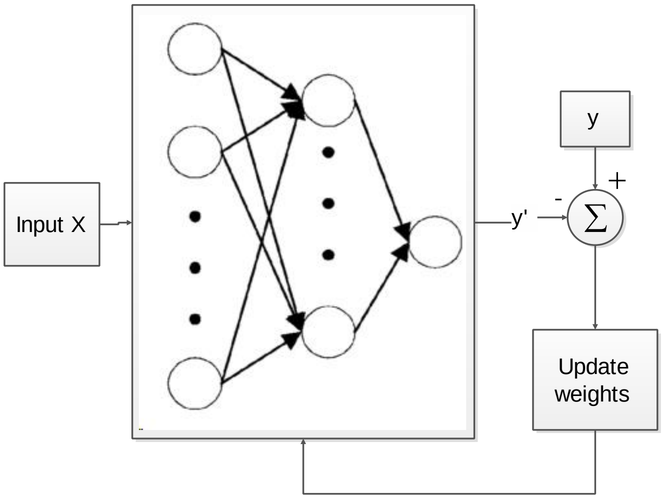

Figure 5.4: Structure of neural network training process.

To train a multilayer FFNN, any standard numerical optimization algorithm can be used to optimize the performance function. However, some algorithms show an excellent performance for NN. These algorithms use either the gradient of the network performance or the Jacobian of the network errors. The gradient and the Jacobian are calculated using a technique called the backpropagation algorithm, which involves performing computations backward through the network.

5.3 Fault Detection Scheme

The ANN can adapt itself to learn a different type of complicated linear and nonlinear function. Therefore, it can learn a different type of motor faults, which results in an accurate prediction of fault occurrence and its severity. This type of detection scheme is inexpensive and noninvasive. This thesis aims to develop ANN detection scheme which overcomes cost problems, complexity, and applies different motor sizes. In conventional detection schemes, a detailed mathematical model is required, and many features are needed to be extracted, which results in a costly instrument for measurement purposes [65].

However, the method used in this thesis will use only the captured stator current data to extract the most important features. If these features are selected as the inputs to the ANN, then the detection of the static eccentricity fault condition can be implemented. Besides, this scheme will be simple, economical, and reliable. Figure 5.5 depicts the detection scheme of static eccentricity using ANN. Stator current is captured using a proper data acquisition system. In this thesis, the stator current is captured at a frequency rate of 10 kHz for a total time duration of 750 ms. Next, some important statistical parameters are calculated; this process is called feature extraction. For the selected features, the neural network is initialized with small weights to calculate the resultant error, as explained in Figure 5.4. The calculated error will propagate backward into the network to update the weights and reduce the output error. This process is repeated until reaching a specified global minimum of error. The neural network should be trained and tested carefully in a healthy and faulty state, under different loading conditions. The neural network can be trained on the data obtained from the finite element analysis or from the mathematical model developed in chapter 3, since their results are in fine agreement.

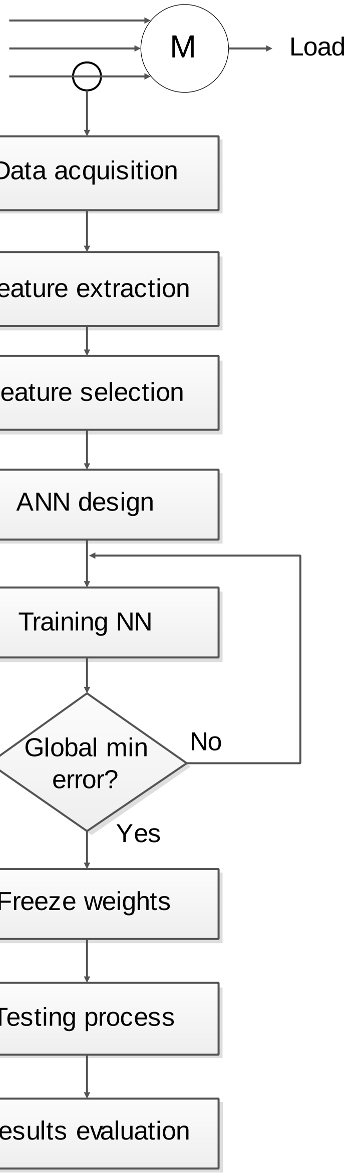

Figure 5.5: Detection scheme using ANN.

5.3.1 Features Extraction

In the process of fault detection using ANNs, two problems are faced: the selection of neural network inputs, and specifying the network parameters. In the LSPMS motor, the spectrum components of static eccentricity in the line current are not fully specified. The authors in [22] specify the frequency components at which this fault can be detected. However, the authors state that these frequencies are highly affected by any change in motor parameters. Furthermore, the stator current spectrum contains not only the fault components but also additional harmonics that are usually presented, such as slotting, supply voltage, and air gap space harmonics. To overcome these drawbacks, the feature extraction process will be made on stator current data.

5.3.2 Features Selection

The features selection algorithms determine the most superior input variable, which maximizes the performance of the detection process. The suitable predictor variable depends on the relationship between the input data. The selection process is not straightforward due to [76]:

1. Large set of the available input variables.
2. Correlation between input variables which create redundancy.
3. Input variables which have no predictive power.

Modelers of ANNs realize that the input variable selection (IVS) algorithms should be utilized to maximize the network performance. The key considerations of IVS can be summarized as [76]:

1. Relevance: The input variables should be informative, which covers the behavior of the operating conditions.
2. Computational efforts: Small number of input variables will increase the speed of training process and decrease the network size.

3. Training difficulty: The difficulty in training increases as the number of redundant and irrelative input variables increases. Inputs that are more redundant result in more local minima under the training process. This may lead to convergence to local minima with poor generalization. In addition, the relationship between redundant variables and performance error is hard to map.
4. Input dimensions: This problem can be handled through the preprocessing of data to minimize the number of network inputs.

The last discussion suggests that the desired input variables are informative, that is, with predictive ability, and less redundant, that is, independent or dissimilar. This thesis will use some simple statistical features as input to the ANN. In this case, the filter method will be used for IVS [76],[77]. Furthermore, principal component analysis (PCA) will be utilized as another alternative in dimensional reduction and variable selection of the input data [65]. These methods will be discussed in the following sections. Although the idea of PCA is different from IVS, they are closely related, as many dimensional reduction methods are used as IVS techniques.

5.3.3 Principal Component Analysis

It is observed that many features need to be extracted that require significant computational efforts to calculate. Therefore, a method is needed to assist features selection and extraction.

The concept of PCA can be used to select the most superior feature to detect fault conditions. This method analyzes the input table data and extracts the most important information represented by a new set of orthogonal vectors called principal components

(PCs). A vector of data represents each principal component (PC). In mathematics, this is defined as a linear transformation of orthogonal vectors which map the data into a new space, such that the great variance from the data is in the first dimension indicated as (F1), which is called the first PC. The second greatest variance located in the second dimension (F2) and so on [78],[65].

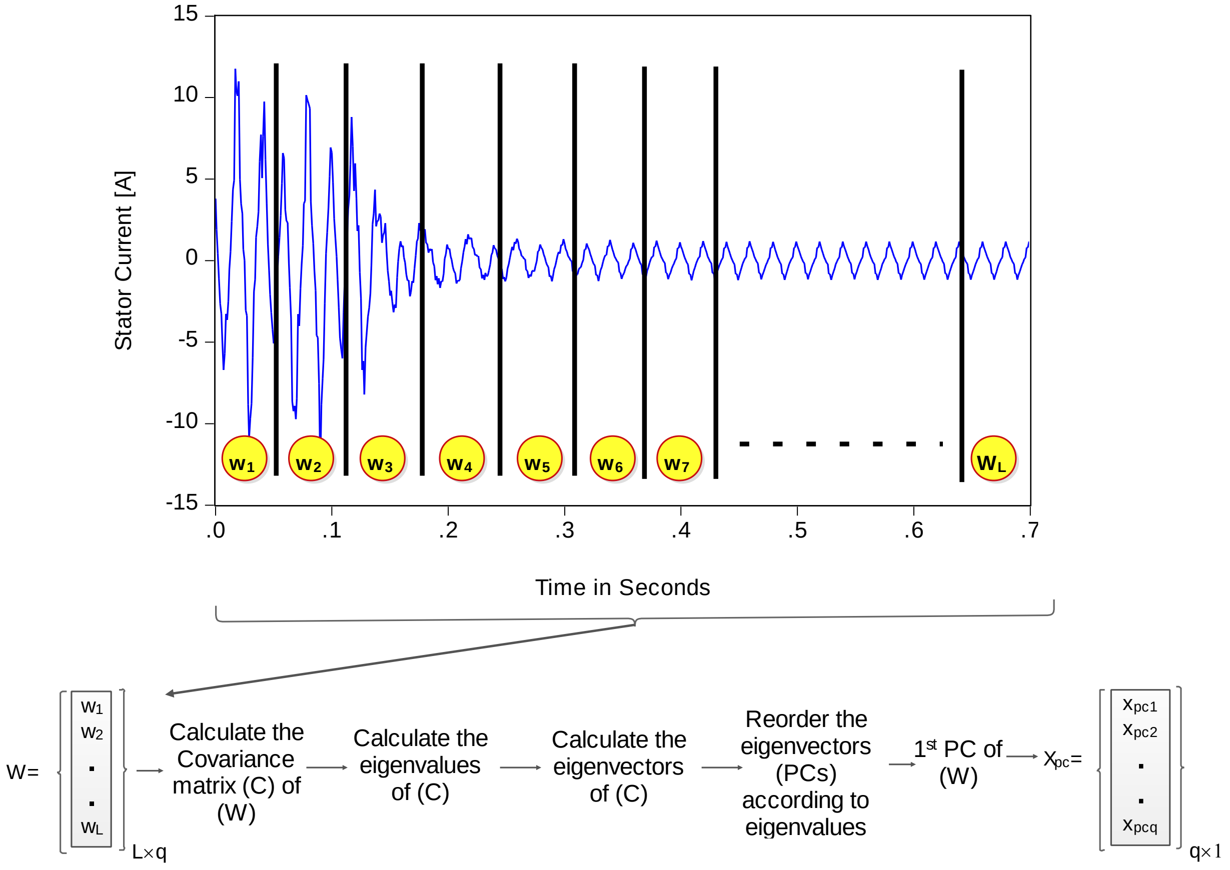

Figure 5.6: Feature extraction using PCA

Figure 5.6 describes the process of applying the PCA to the stator current. First, the input row data (stator current) is divided into partitions, while each partition represents a window. As the total number of windows and points per input are known, the window size is specified. Consider the row input data $X = [X_1\ X_2\ \ldots X_j]$, where j is the number of points per input, the resulted input matrix will have the following form $W = [W_1\ W_2\ \ldots W_L]^T$ where L is the number of windows. The size of each window (q) is equal to the number of points per input divided by the total number of windows. Therefore, the windows matrix dimension is $L\times q$. Secondly, the covariance matrix (C) for the windows matrix (W) is calculated. The eigenvalues and eigenvectors are determined for the matrix (C). The eigenvectors are reordered according to the value of the eigenvalues in descending order. The first PC vector (X_{pc}) will be used as the feature vector, which has a dimension of $q\times 1$.

For example, performing PCA on the stator current with a window matrix dimension of 500 by 15, yields the following eigenvalues and variability of projection, as shown in Table 5.1. The variability describes how much information is carried by the first eigenvector or PC. It is obvious that the first component carries 93.9% of the total information in the input signal, with the largest eigenvalue of 28.1. The second axis carries only 5.9% of the total projected data. Both axes implement 99.85% of the total data as shown in Figure 5.8. The variability of data projection on the second and third axis is small with 5.94% for the second axis and 0.14% for the third axis. It can be concluded that the first PC can be used with higher accuracy as the input variable to ANN with 93.9% of the variability.

Table 5.1: Eigenvalues variability of projection

	F1	F2	F3	F4	F5	F6	F7
Eigenvalue	28.174	1.781	0.043	0.001	0.000	0.000	0.000
Variability (%)	93.914	5.938	0.143	0.004	0.000	0.000	0.000
Cumulative %	93.914	99.852	99.996	100.000	100.000	100.000	100.000

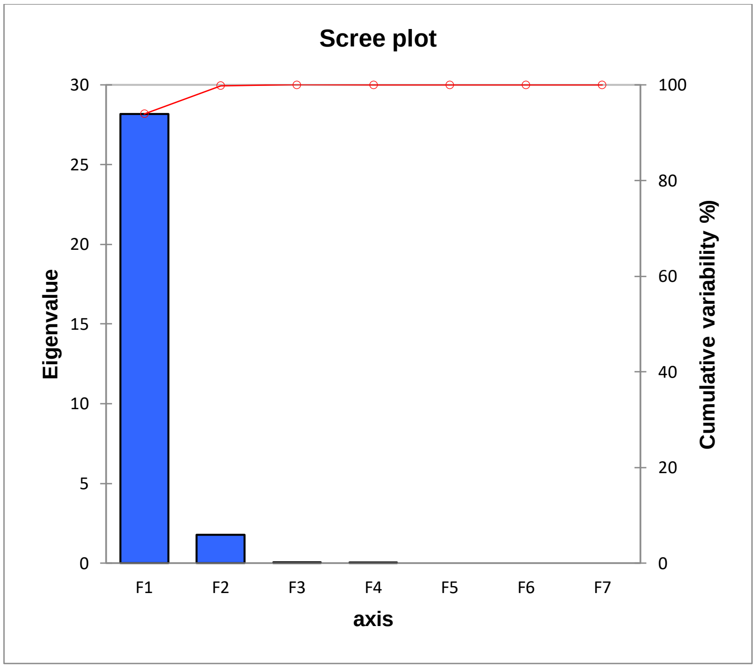

Figure 5.7: Eigenvalues and cumulative variability over projection axes.

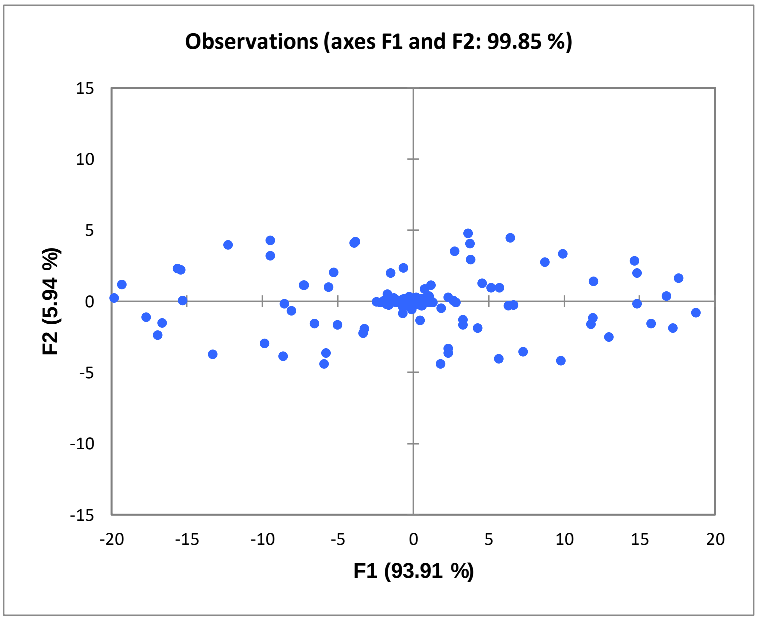

Figure 5.8: Scatter plot of input data on projection axes for the first two PCs.

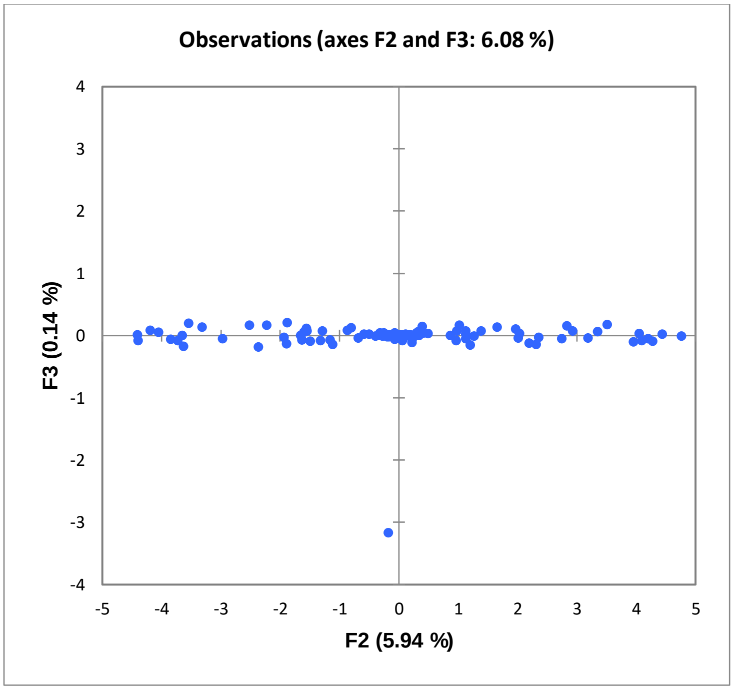

Figure 5.9: Scatter plot of input data on projection axes for the second and third PCs.

5.3.4 Simple statistical variables

As discussed before, a common selection method of the input variables is the filter method [76],[77]. This method separates the selection process from the training procedure of ANN, as shown in Figure 5.10. It is based on measuring the relevance between individual variables in a group of inputs. This function is performed using a search algorithm, such as the correlation. The selection criteria of this method depend on [76]:

1. The maximum relevance (MR) which selects the most informative variables.
2. The minimum redundancy (mR) which selects variables with unique features.
3. The minimum redundancy–maximum relevance (mR-MR) which combine the first and second points above.

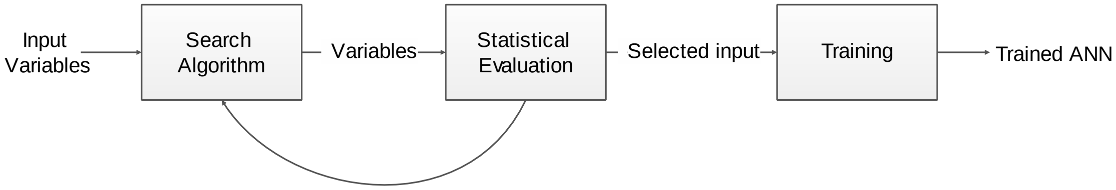

Figure 5.10: Filter method algorithm.

Using a minimum collection set of dimensional and non-dimensional statistical features to generate the input variables [79], the correlation-based filter method can be utilized. The calculated statistical features for the input row data X (stator current) are shown in equation (5.1) to (5.7). This process is described in Figure 5.11 and it is similar to the calculations of PCs. Consider the row input data $X = [X_1\ X_2 \ldots X_j]$, where j is the number of points per input, the windows matrix (W) will have the following form $W = [W_1\ W_2 \ldots W_L]^T$ where L is the number of windows. The size of each window (q) is equal to the number of points per input divided by the total number of windows. Therefore, the windows matrix dimension is $L{\times}q$. The statistical features are calculated for the matrix W, and the feature vector X_{sv} is obtained which has a dimension of $L{\times}1$. The last features are calculated under healthy and static eccentricity fault conditions, which include a wide combination of static eccentricity and load values.

Sum:

$$X_{sum} = \sum X_i \tag{5.1}$$

Mean:

$$X_{mean} = \frac{\sum X_i}{N} \tag{5.2}$$

Root mean square (RMS):

$$X_{RMS} = \sqrt{\frac{\sum X_i^2}{N}} \tag{5.3}$$

RSSQ:

$$X_{RSSQ} = \sqrt{\sum |X_i^2|} \tag{5.4}$$

Energy:

$$X_{En} = \sum X_i^2 \tag{5.5}$$

Variance:

$$X_v = \frac{\sum |X_i - X_{mean}|^2}{N - 1} \tag{5.6}$$

Kurtosis:

$$X_k = \frac{1}{N} \frac{\sum (X_i - X_{mean})^4}{\alpha} \tag{5.7}$$

Where N is the number of samples, and α is the standard deviation which defined as:

$$\alpha = \sqrt{\frac{\sum(X_i - X_{mean})^2}{N}} \tag{5.8}$$

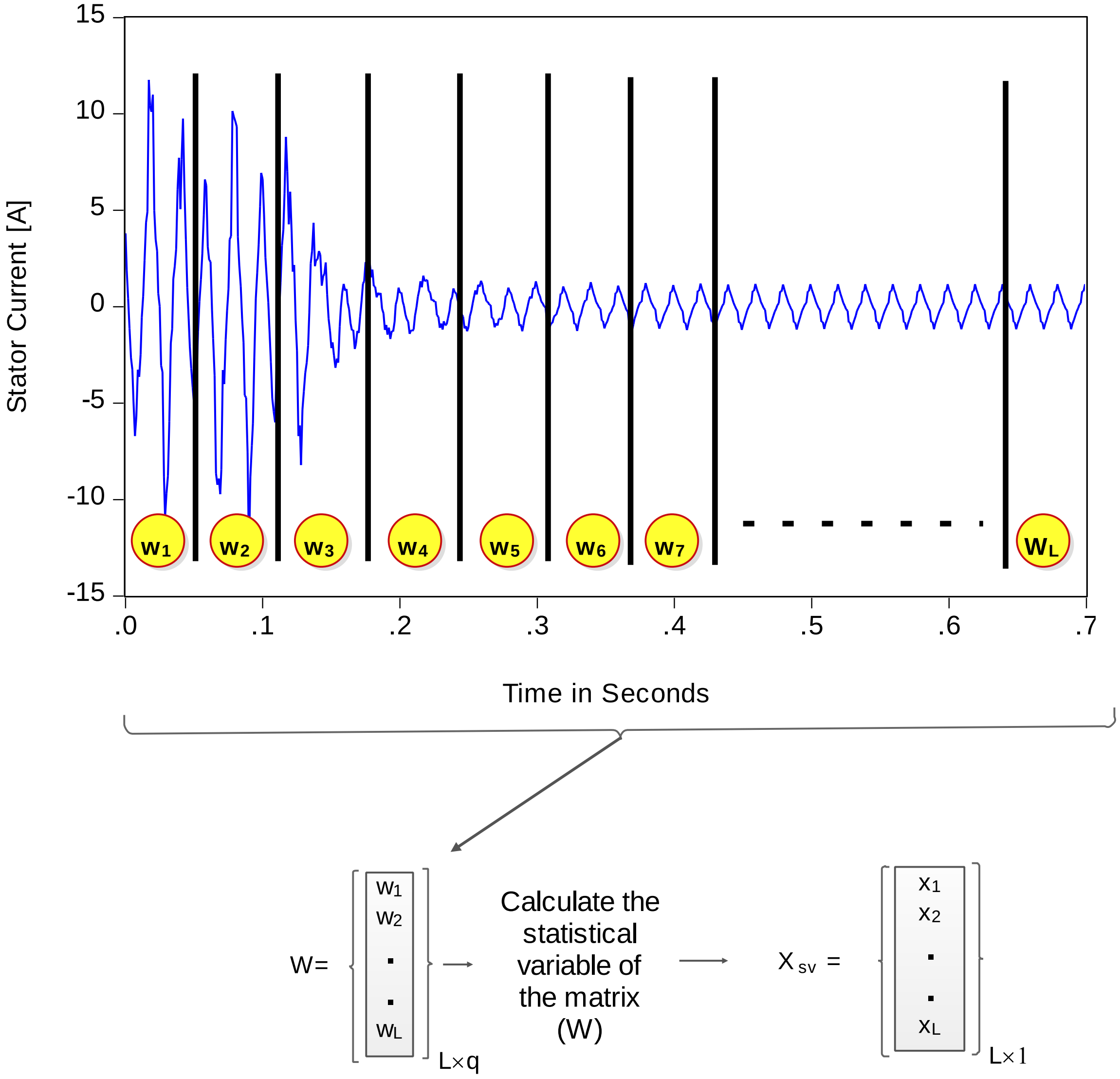

Figure 5.11: Feature extraction using statistical variables

The calculation of the correlation is conducted using Excel^{TM} between the input variables introduced in equation (5.1) to (5.8). The obtained correlation matrix is depicted in Table 5.2. The minimum redundancy criteria suggest the mean or the sum as the qualified input to the ANN with a minimum correlation to other variables. Furthermore, the PCA can be used to assist the process of selecting the inputs. If these statistical measurements of stator current are the inputs in PCA, they can be projected on the orthogonal axes. Figure 5.12 presents the correlation circle for the input variables projected on the first two PCs. It is obvious that RMS, variance, energy, and RSSQ are strongly correlated to each other and redundant. In addition, kurtosis is negatively correlated with the first set of variables. Some unique features are carried by the sum and mean features. In conclusion, the filter IVS method and PCA suggest one of these variables as the input for the ANNs. The mean feature will be selected as a statistical feature input to the neural network.

Table 5.2: Correlation matrix of selected input variables.

Variables	Mean	RMS	RSSQ	Energy	Variance	Kurtosis	sum
Mean	**1**	**-0.802**	**-0.802**	**-0.787**	**-0.787**	**0.791**	**1.000**
RMS	**-0.802**	1	1.000	0.999	0.999	-0.989	-0.802
RSSQ	**-0.802**	1.000	1	0.999	0.999	-0.989	-0.802
Energy	**-0.787**	0.999	0.999	1	1.000	-0.982	-0.787
Variance	**-0.787**	0.999	0.999	1.000	1	-0.982	-0.787
Kurtosis	**0.791**	-0.989	-0.989	-0.982	-0.982	1	0.791
sum	**1.000**	**-0.802**	**-0.802**	**-0.787**	**-0.787**	**0.791**	**1**

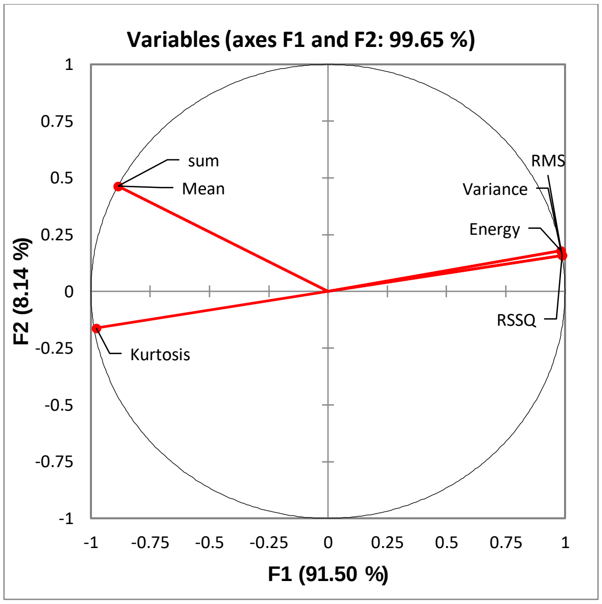

Figure 5.12: Correlation circle of input variables.

5.4 Simulation Results

This section will present the results of training and testing process of ANN which designed to detect static eccentricity fault for the LSPMS motor under different operating conditions. The network is trained to specify the degree of static eccentricity for each tested condition. The performance criteria are based on the percentage error and the accuracy. The percentage error is obtained between the actual value of static eccentricity and the predicted one as shown in equation (5.2). If the error is less than or equal to a predefined value, then the accuracy can be determined. The accuracy is defined as the percentage of the total amount of correct predicted outputs S over the total tested samples N, which subjected to the error condition in equation (5.2). This thesis will assume a predefined percentage error value between the actual value of static eccentricity and the predicted one to be are 10 %, 15 %, and 20 %. Besides, the mean square error (MSE) is obtained for each simulation case as a performance indicator. However, smaller MSE isn't an indication of higher accuracy since a model with more inputs tends to be biased due to overfitting. The following formulas are used for accuracy, percentage error, and MSE:

$$Accuracy = \frac{S}{N} \times 100\ \% \tag{5.9}$$

$$\mathrm{Error} = \left| \frac{\delta_s - \delta_s'}{\delta_s} \right| \times 100\ \% \tag{5.10}$$

$$\mathrm{MSE} = \frac{\sum_{i=1}^{N} \left(\delta_{s_i} - \delta_{s_i}' \right)^2}{N} \tag{5.11}$$

Where δ_s, δ_s', and N are the actual output of SE, predicted output of SE by NN, and the number of observations, respectively.

As shown in Figure 5.13, two separate inputs are considered for the training and testing process of the ANN which are the 1st PC and the mean feature. When the 1st PC is the input to the neural network, the input vector has a dimension of $q \times 1$. In this case, the window size (q) is equal to the number of inputs to the ANN. Therefore, the number of windows is increased to reduce the window size. In other words, as the number of windows increases, the number of inputs will decrease. However, in the case of having the mean feature as the input to the neural network, the number of inputs will be equal to the number of windows (L).

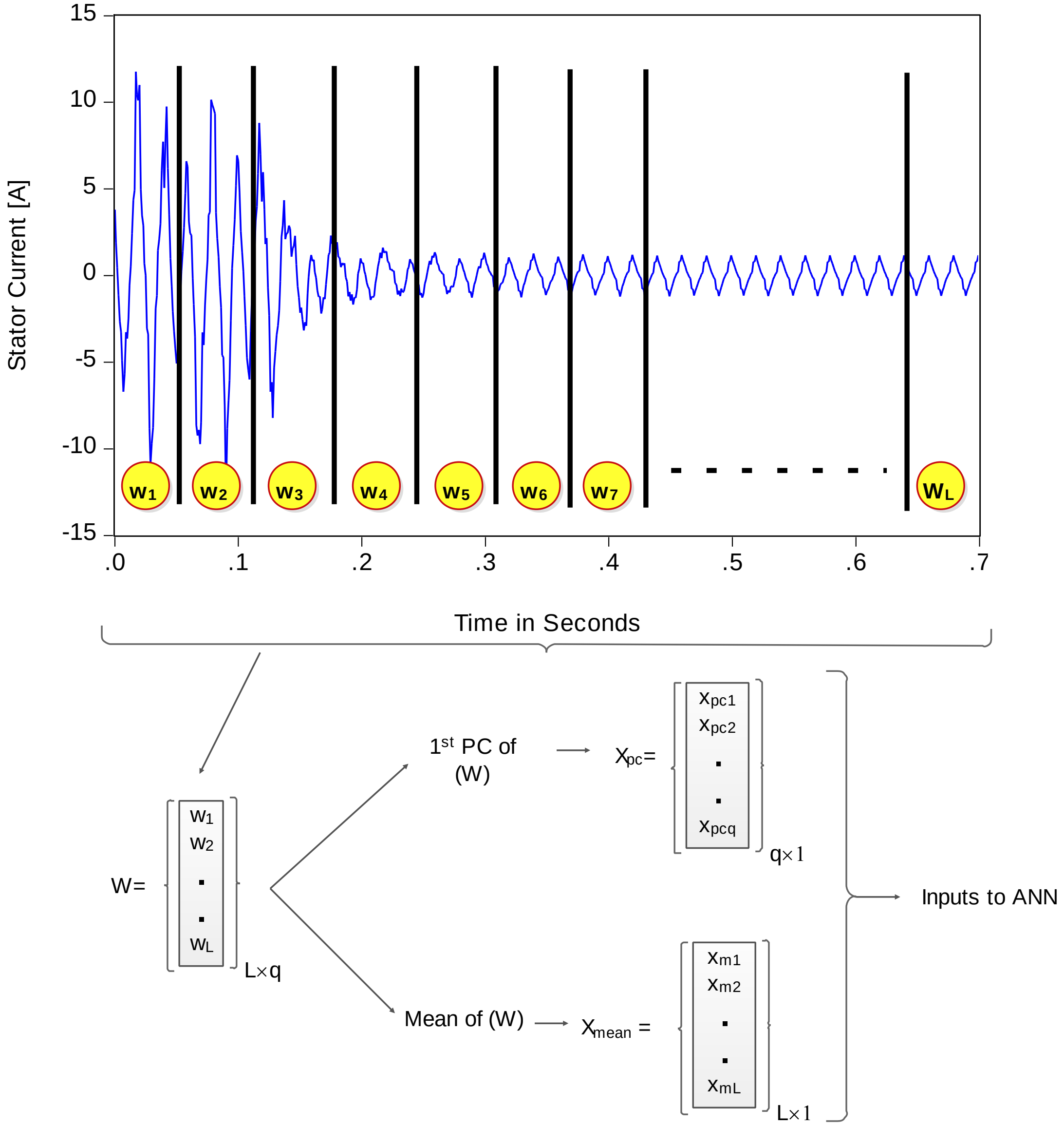

Figure 5.13: The input features to the ANN

Several experimentations are performed to select the FFNN parameters, and the best results are obtained with the following specifications:

- Number of hidden layers: 2

- Number of neurons in the hidden layers: 10
- Learning rule: Levenberg-Marquardt
- Stopping condition - epochs :10000
- Stopping condition - MSE: 1×10^{-8}

The network has been trained and tested on a wide range of operating conditions. The tested and trained samples are 160 and 320 different combinations of static eccentricity and load values, respectively. In addition, the tested samples are completely different from the trained samples. The trained degrees of static eccentricity and the input loads are shown in Table 5.3 and Table 5.4, respectively. Each degree of static eccentricity is trained for the total load values; this will result in 320 different operating conditions used in the training process.

Table 5.3: Degrees of static eccentricity used in training process

Percentage of static eccentricity degrees for training process (δ_s)							
6%	8%	10%	11%	13%	15%	17%	19%
21%	23%	25%	27%	29%	30.5%	32%	33%

Table 5.4: Input load values used in training process

Input load values for training process (N.m)									
0	0.1	0.2	0.3	0.4	0.5	0.6	0.7	1	1.1
1.3	1.6	1.8	1.9	2	2.1	2.2	2.3	2.4	2.5

Table 5.5 presents the simulation results while considering the first PC as the input to the neural network. Gradually, the number of inputs is decreased, and the network performance is observed carefully, concerning accuracy and percentage of error. It is evident that case 5 results in a higher accuracy with 98.75 % under 20 % error, 97.5 % under 15 % error, and 95.6 % under 10 % error. Figure 5.14 summarizes these results.

Table 5.5: Results summary considering the first PC as input to NN.

Case	Number of Window	Number of Inputs	Accuracy %			
			Error20%	Error15%	Error10%	MSE
1	100	75	93.75	89.375	79.375	5.65E-07
2	150	50	97.5	95.625	94.375	4.46E-07
3	250	30	95.625	94.375	90.625	5.11E-07
4	300	25	93.75	92.5	89.375	1.71E-08
5	**500**	**15**	**98.75**	**97.5**	**95.6**	**1.05E-05**
6	750	10	90	86.25	81.875	6.21E-08
7	1250	6	97.5	96.25	94.375	7.93E-07
8	1500	5	98.125	95.625	92.5	1.37E-06

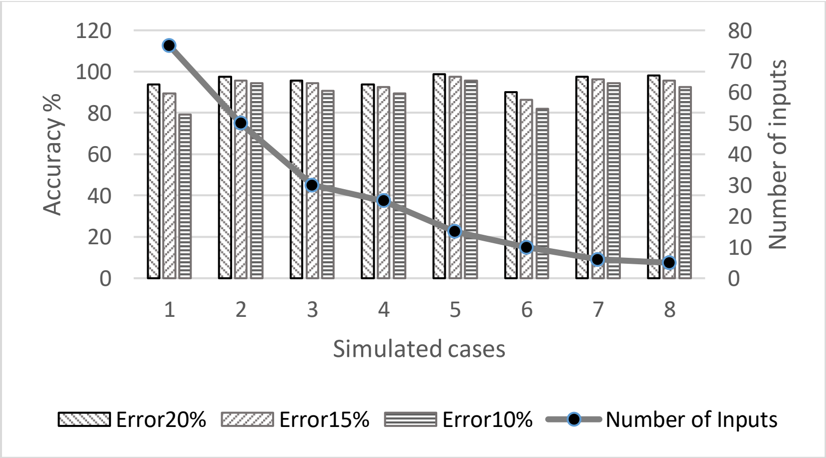

Figure 5.14: Accuracy, error percentage, and number of inputs (PCA).

Considering the first PC as input for the neural network, the output results for the tested samples are presented in Table 5.6. The hatched cells indicate that the NN fails to predict the actual output under a 10 % error limit.

Table 5.6: ANN results using the first PC as input to the ANN with error limit of 10 % (case 5 in Table 5.5).

Exact percentage of SE (δ_s) and the predicted value (δ'_s) correspond to each load (L- N.m)										
δ'_s-L δ_s	δ'_s **0 N.m**	δ'_s **0.25N.m**	δ'_s **0.65N.m**	δ'_s **1.65N.m**	δ'_s **1.65N.m**	δ'_s **1.70N.m**	δ'_s **1.95N.m**	δ'_s **2.25N.m**	δ'_s **2.35N.m**	δ'_s **2.45N.m**
7.0	7.31	6.97	6.98	7.01	7.7	7.47	7.05	7.68	7.11	**5.34**
9.0	8.94	8.8	8.82	8.78	9.3	9.14	8.85	9.16	8.12	**7.1**
10.0	9.84	9.8	9.82	9.75	10.19	10.06	9.83	10	**8.52**	**8.61**
12.0	11.76	11.89	11.93	11.8	12.08	12.02	11.91	11.84	**9.62**	11.18
14.0	13.77	14.02	14.07	13.91	14.08	14.08	14.05	13.83	**11.82**	13.35
16.0	15.83	16.13	16.17	16.01	16.12	16.15	16.16	15.91	14.81	15.5
18.0	17.9	18.17	18.2	18.08	18.16	18.2	18.19	18.03	17.74	17.68
20.0	19.96	20.15	20.15	20.09	20.17	20.21	20.13	20.11	20.2	19.96
22.0	22.02	22.09	22.06	22.07	22.15	22.17	22.01	22.13	22.21	22.34
24.0	24.07	24.03	23.98	24.04	24.13	24.11	23.89	24.12	24.01	22.57
26.0	26.11	25.98	25.94	26.03	26.13	26.07	25.86	26.11	25.82	28.53
28.0	28.13	27.95	27.95	28.03	28.19	28.11	27.96	28.13	27.75	28.45
30.0	30.1	29.91	29.99	30.04	30.31	30.25	30.15	30.12	29.73	29.45
31.0	31.07	30.88	30.99	31.03	31.37	31.35	31.22	31.08	30.66	31.15
32.5	32.44	32.29	32.46	32.48	32.86	33	32.58	32.57	32.04	34.77
33.5	33.23	33.2	33.4	33.41	33.73	34.03	33.17	33.83	33.21	**37.61**

Consequently, Table 5.7 depicts the results, considering the mean feature as the input to the ANN. Case 3 and 4 seem to be comparable to case 5 in Table 5.5. The accuracy of case 5 in Table 5.5 under 20 % error is 98.75 %, which is slightly higher than the accuracy of case 4 and 5 in Table 5.4, which is 98.125 %. However, when comparing the accuracy under 10 % error in both tables, the accuracy rate is higher for case 3 and 4 in Table 5.4. In addition, the number of inputs decreases to 10 as shown in case 3 instead of 15 as presented in case 5 of Table 5.5. Figure 5.12 summarizes these findings.

Table 5.7: Results summary considering the mean feature as input to NN.

Case	Number of Window	Number of Inputs	Accuracy %			
			Error20%	Error15%	Error10%	MSE
1	5	5	80.625	75.625	63.125	3.07E-06
2	6	6	96.875	95	93.75	7.82E-08
3	**10**	**10**	**98.125**	**97.5**	**96.875**	**3.28E-12**
4	**15**	**15**	**98.125**	**98.125**	**96.875**	**2.50E-08**
5	25	25	90.625	90.625	90.625	2.16E-10
6	30	30	80.625	78.75	74.375	1.53E-09
7	50	50	92.5	90.625	89.375	8.24E-11
8	75	75	96.875	95.625	93.125	2.23E-09

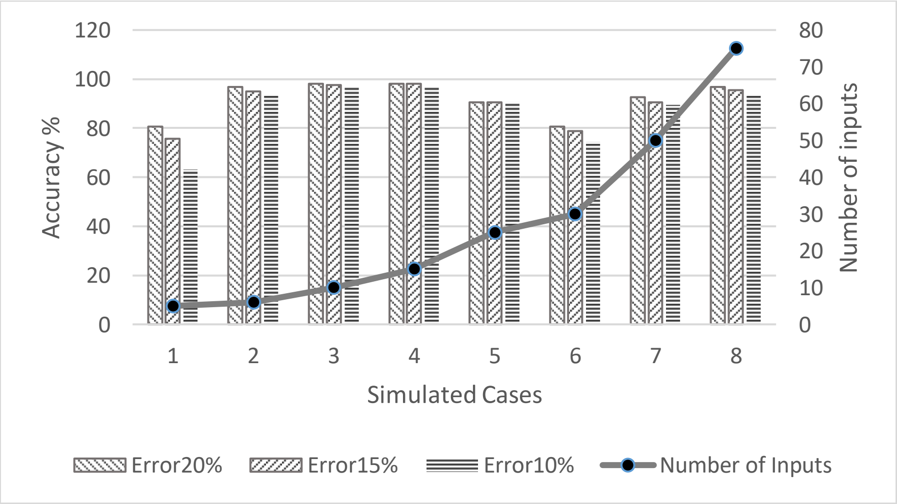

Figure 5.15: Accuracy, error percentage, and number of inputs (mean).

The output results of the tested samples for case 3 and 4 in Table 5.7 are presented in Table 5.8, and Table 5.9, respectively. The hatched cells indicate that the NN fails to predict the actual output under 10 % error limit.

Table 5.8: ANN results using mean as input to the ANN with error limit of 10 % (case 4 in Table 5.7)

Exact percentage of SE (δ_s) and the predicted value (δ'_s) correspond to each load (L- N.m)										
δ'_s-L δ_s	δ'_s **0 N.m**	δ'_s **0.25N.m**	δ'_s **0.65N.m**	δ'_s **1.65N.m**	δ'_s **1.65N.m**	δ'_s **1.70N.m**	δ'_s **1.95N.m**	δ'_s **2.25N.m**	δ'_s **2.35N.m**	δ'_s **2.45N.m**
7.0	6.98	6.99	6.99	6.99	6.88	6.9	6.99	6.93	**15.57**	6.83
9.0	9	9	9	9	8.78	8.87	9	8.99	8.7	8.19
10.0	10	10	10.01	10	9.75	9.87	10	10.01	**8.8**	9.01
12.0	12.01	12	12	12	11.72	11.84	12	12.01	**10.64**	10.95
14.0	14	13.99	14	14	13.73	13.83	13.99	14.01	13.41	13.2
16.0	16	15.99	16	16	15.81	15.84	16	16.01	16.08	15.57
18.0	18	18	18	18	17.94	17.9	18	18.01	18.12	17.9
20.0	20	20	20	20	20.07	19.98	20.01	20.01	20.03	**26.33**
22.0	22	21.99	22	22	22.11	22.08	22	22	21.99	**163.15**
24.0	24	23.99	24	24	24.02	24.15	24	24	23.98	24.42
26.0	26	25.98	26	25.99	25.9	26.13	26	26	25.98	26.72
28.0	28	27.97	28	28	27.83	28.01	28	28	27.99	27.88
30.0	30	29.97	30.01	30	29.76	29.94	30	30	30	30.1
31.0	30.99	30.98	31.01	31	30.8	30.97	31.01	31	31	31.2
32.5	32.53	32.51	32.51	32.5	32.61	32.47	32.51	32.5	32.49	32.72
33.5	33.08	33.55	33.5	33.49	33.94	33.39	33.51	33.51	33.5	33.7

Table 5.9: ANN results using mean as input to the ANN with error limit of 10 % (case 3 in Table 5.7)

Exact percentage of SE (δ_s) and the predicted value (δ'_s) correspond to each load (L- N.m)										
δ'_s-L δ_s	δ'_s 0 N.m	δ'_s 0.25N.m	δ'_s 0.65N.m	δ'_s 1.65N.m	δ'_s- 1.65N.m	δ'_s 1.70N.m	δ'_s 1.95N.m	δ'_s 2.25N.m	δ'_s 2.35N.m	δ'_s 2.45N.m
7.0	6.99	7.23	7.04	6.96	6.55	6.61	6.98	7.17	**8.63**	6.55
9.0	9	9.31	9.04	8.98	8.7	8.76	9	9.06	**8.05**	9.03
10.0	10	10.35	10.03	9.99	9.77	9.82	10	10.04	**8.04**	10.15
12.0	12	12.43	11.98	12	11.87	11.89	12	12.03	**9.68**	12.21
14.0	14	14.52	13.95	14.01	13.94	13.94	14	14.03	13.42	14.17
16.0	16	16.61	15.93	16.01	15.99	15.97	16	16.02	15.76	16.14
18.0	18	18.67	17.92	18	18.03	18	18	18.01	17.89	18.09
20.0	20	20.68	19.9	19.99	20.06	20.03	20	20	19.95	20.1
22.0	21.99	22.61	21.89	21.99	22.09	22.05	22	21.99	21.97	20.86
24.0	24.02	24.48	23.88	24	24.11	24.06	24	23.99	23.98	23.94
26.0	25.97	26.3	25.89	26.01	26.13	26.08	26.01	26	25.99	26.18
28.0	28.02	28.13	27.9	28.02	28.17	28.1	28.01	28	28	28.09
30.0	30	30.07	29.92	30.02	30.23	30.14	30.01	30	30	30.02
31.0	30.71	31.14	30.93	31.01	31.25	31.16	31	31	31	31
32.5	33.3	32.93	32.43	32.5	32.79	32.69	32.5	32.5	32.5	32.49
33.5	**41.22**	34.32	33.43	33.47	33.79	33.72	33.49	33.5	33.5	33.5

The failing process is not enough to describe and compare the resulted output of NN. The percentage of error should be obtained over the tested operating conditions. Figure 5.16 depicts the percentage error over the tested range considering the first PC with 15 inputs and the mean feature with 10 inputs. The average value of the error over the tested cases is 2.059 % using the first PC with 15 inputs and 1.482 % for the mean feature with 10 inputs. The maximum error value is 23 %, which corresponds to one case at no load. The PCs and mean features perform efficiently at lower loads, while the margin of error increases at higher loads.

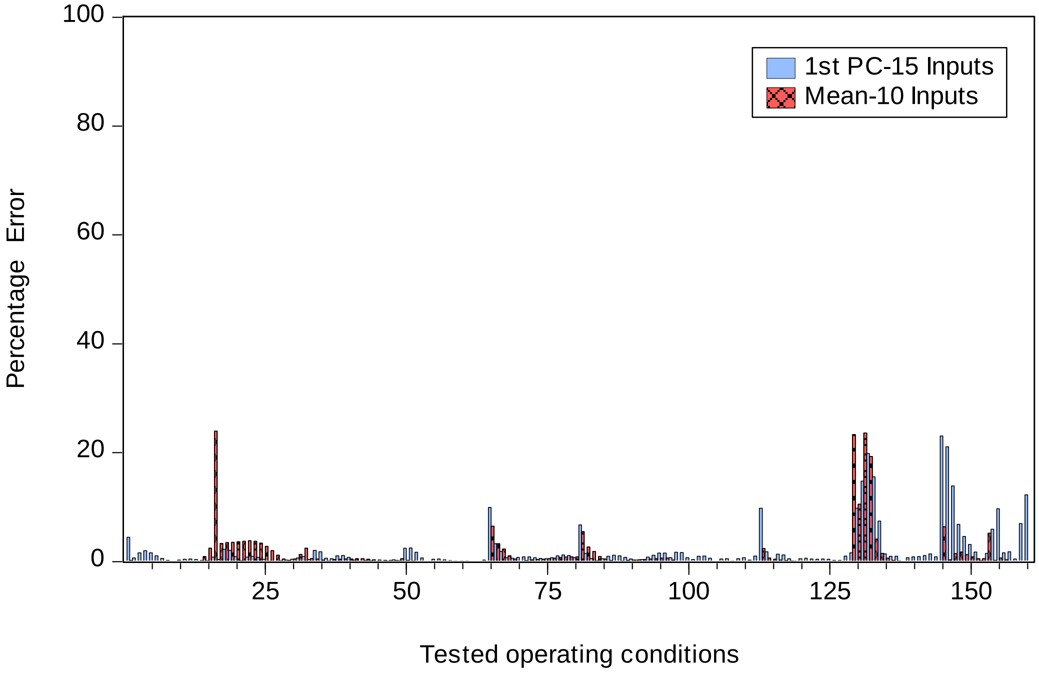

Figure 5.16 Percentage error comparison under different number of inputs.

Finally, the accuracy should be discussed as a function of the inputs to the ANN. Figure 5.17 compares the accuracy under 10 % error of both features. It can be noticed that the mean feature is highly sensitive to any change in input numbers. However, it is obvious that the accuracy of the mean feature is superior when using 10 inputs.

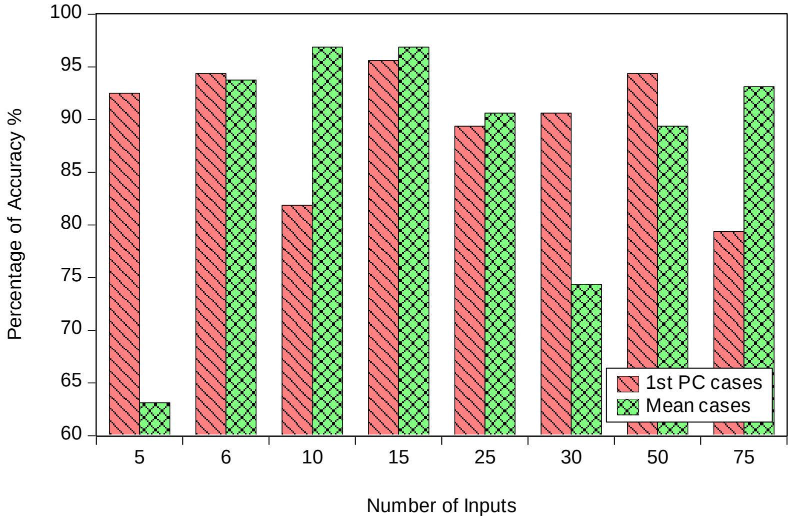

Figure 5.17: Accuracy as a function of inputs for 10% error limit.

5.5 Discussion and Conclusion

In conclusion, this chapter proposed a detection method for the static eccentricity fault in LSPMS motors. The detection technique is based on the motor current signature analysis and the artificial neural networks. The mean feature and the first PC have been selected as the inputs for the ANN. Results show that the mean feature is superior regarding accuracy, average output error, and the number of inputs to the ANN. Table 5.10 summarizes these findings.

Table 5.10: Summary of the simulation results

Feature	**Number of inputs**	**Average error over tested samples**	**Accuracy**
1st PC	15	2.059 %	95.6 %
Mean	10	1.4829 %	96.87 %

CHAPTER SIX

CONCLUSIONS AND RECOMMENDATIONS

6.1 Conclusions

To the best knowledge of the researcher, this is the first reported work on the mathematical modeling of the static eccentricity fault condition in LSPMS motors, under different loading conditions. The mathematical model is justified under healthy and static eccentricity fault conditions using FEM. Furthermore, this work proposes a neural based detection technique of this fault. The following thesis findings and conclusions can be summarized as follows:

- A comprehensive literature review has been accomplished on the eccentricity fault, covering both induction and synchronous motors. The investigations on the static eccentricity fault in LSPMS motor are still premature.
- The mathematical models are developed, including both healthy and static eccentricity fault conditions. The fault condition is modeled based on the modified winding function method and coupled magnetic circuit approach. The simulation is performed using MATLAB SIMULINK^{TM}.
- To verify the developed mathematical model, a finite element model is created using JMAG^{TM} software. The model considers all the geometric complexities provided in the motor datasheets. A comparison between the FEM and the mathematical model results has been conducted.

- Under different operating loads, the effect of static eccentricity is evaluated on the motor line current, electromagnetic torque, and speed characteristics. The degrees of static eccentricity considered in the simulation vary from 13% to 33%, in order to obtain more practical results.
- The simulation results of the FEM and the mathematical model are compared. Results show that the time variation of the stator current using MATLAB^{TM} follows the same time variation of the FEM simulation. In addition, the speed and torque characteristics follow the same trend in the transient period. Moreover, the steady-state results are congruent.
- A comparison between the time variations of stator current, torque, and speed, under healthy and faulty conditions, shows that the synchronization time of the LSPMS motor increases as the degree of static eccentricity is increased. More peaks are shown in the transient period during the starting process.
- A neural-based detection method of static eccentricity is proposed utilizing the motor stator current. The PCA along with some statistical features of the stator current are calculated and used as the input variables to the neural network. Results show that the mean feature is the superior input variable if statistical variables are used. In this method, the sub-optimal number of inputs is found to be 10, with a detection accuracy of 98.75% under 20% error and 96.87% under 10% error. If the PCs are the input variables, the number of inputs increases to 15 with the same level of accuracy.

- As the number of the neural network inputs is larger than 15, the accuracy of the detection scheme is improved using PCA. On the other hand, the accuracy deteriorates for the mean feature.

6.2 Recommendations for Future Work

Finally, as is the case for any computational-based research, there is a scope for further enhancement of the study. The problem of the eccentricity fault in LSPMS motors is far from being completed by only relying on a limited number of case studies and software packages. Therefore, to comprehensively study the problem, some recommendations may be addressed as well:

- The static eccentricity fault could be happening along with dynamic eccentricity. The analysis should be extended to include the dynamic and mixed eccentricity fault conditions.
- Experimental setups can be done by referring to the part in the literate review, to confirm the simulation results.
- The mathematical model can be further improved by changing the rotor model to accommodate the rotor bars effect instead of using a three-phase equivalent model. In addition, under eccentricity fault, the motor inertia constant, as well as the magnetic operating point, are not fixed. An extensive study should be made to represent these effects.

- The fault detection process can be further improved by utilizing some optimization algorithms to assist selecting the optimal input variables, as well as the number of inputs, which will improve the accuracy of the detection system.

REFERENCES

[1] R. Saidur, “A review on electrical motors energy use and energy savings,” *ELSEVIER, Renewable and Sustainable Energy Reviews*, vol. 14, no. 3, pp. 877–898, 2010.

[2] W. Fei, P. Luk, J. Ma, J. Shen, and G. Yang, “A high-performance line-start permanent magnet synchronous motor amended from a small industrial three-phase induction motor,” *IEEE Transactions on Magnetics*, vol. 45, no. 10, pp. 4724–4727, 2009.

[3] A. Hassanpour Isfahani and S. Vaez-Zadeh, “Line start permanent magnet synchronous motors: Challenges and opportunities,” *ELSEVIER, Energy*, vol. 34, no. 11, pp. 1755–1763, 2009.

[4] N. W. Frank, “Analysis of the concentric planetary magnetic gear,” Phd Thesis, Texas A&M University, 2011.

[5] H. A. Toliyat, S. Nandi, S. Choi, and H. Meshgin-kelk, *Electric machines - modeling condition monitoring and fault diagnosis*. CRC Press Taylor & Francis Group, 2013.

[6] S. Nandi, H. A. Toliyat, and X. Li, “Condition monitoring and fault diagnosis of electrical motors - A review,” *IEEE Transactions on Energy Conversion*, vol. 20, no. 4, pp. 719–729, Dec. 2005.

[7] A. Siddique, G. S. Yadava, and B. Singh, “A Review of stator fault monitoring techniques of induction motors,” *IEEE Transactions on Energy Conversion*, vol. 20, no. 1, pp. 106–114, Mar. 2005.

[8] M. H. Soreshjani and A. Sadoughi, “Conceptual comparison of line-start permanent magnet synchronous,” *JWEET*, vol. 3, no. 1, pp. 26–36, 2014.

[9] M. G. Kahrisangi, A. H. Isfahani, S. Vaez-Zadeh, and M. R. Sebdani, “Line-start permanent magnet synchronous motors versus induction motors: A comparative study,” *Higher Edu. Press and Springer-Verlag Ber. Heid.*, vol. 7, no. 4, pp. 459–466, 2012.

[10] H. Behbahanifard and A. Sadoughi, “Line start permanent magnet synchronous motor performance and design ; a Review,” *JWEET*, pp. 58–66, 2015.

[11] S. Kahourzade, A. Mahmoudi, and W. P. Hew, “Performance improvement of a line-start permanent-magnet synchronous motor,” *IEEE Transactions on Industrial Electronics*, pp. 1–1, 2014.

[12] X. Xu, Y. Cui, X. Wang, H. Feng, and J. Si, “Performance analysis of line-start permanent magnet synchronous motor with novel rotor structure,” *International Journal of Digital Content Technology and its Applications(JDCTA)*, vol. 7, no. 6, pp. 291–295, 2013.

[13] D. Stoia, M. Cernat, and A. Jimoh, “Analytical design and analysis of line-start permanent magnet synchronous motors,” in *IEEE AFRICON*, 2009, no. September, pp. 1–7.

[14] T. J. E. Miller, M. Popescu, C. Cossar, M. McGilp, G. Strappazzon, N. Trivillin, and R. Santarossa, “Line-start permanent-magnet motor single-phase steady-state performance analysis,” *IEEE Transactions on Industry Applications*, vol. 40, no. 2, pp. 516–525, 2004.

[15] M. A. Rahman, A. M. Osheiba, K. Kurihara, M. A. Jabbar, H. W. Ping, K. Wang, and H. M. Zubayer, "Advances on single-phase line-start high efficiency interior permanent magnet motors," *IEEE Transactions on Industrial Electronics*, vol. 59, no. 3, pp. 1333–1345, 2012.

[16] J. Liu, W. Wang, F. Golnaraghi, and K. Liu, "Wavelet spectrum analysis for bearing fault diagnostics," *Measurement Science and Technology*, vol. 19, no. 1, pp. 230–242, Jan. 2008.

[17] "Association for maintenance professionals (AMP)," 2007. [Online]. Available: http://www.maintenance.org/topic/rotor-bar-problem-3. [Accessed: 20-Jun-2011].

[18] P. Zalas, T. Zawilak, and J. Zawilak, "Synchronization process of permanent magnet synchronous motor from over synchronous speed," in *IEEE Conf. Selected Problems of Electrical Engineering and Electronics (WZEE)*, 2015, pp. 1–4.

[19] W. Lu, H. Zhao, and S. Liu, "Demagnetization conditions comparison for line-start permanent magnet synchronous motors," in *17th International Conference on Electrical Machines and Systems*, 2014, pp. 48–52.

[20] X. Tang and X. Wang, "Research of the demagnetization mechanism of line-start permanent magnet synchronous motor under operating condition of sudden reversal," in *17th International Conference on Electrical Machines and Systems (ICEMS)*, 2014, pp. 1981–1984.

[21] H. A. Toliyat, M. S. Arefeen, and A. G. Parlos, "A method for dynamic simulation of air-gap eccentricity in induction machines," *IEEE Transactions on Industry Applications*, vol. 32, no. 4, pp. 910–918, 1996.

[22] M. Karami, N. Mariun, M. Rezazadeh Mehrjou, M. Z. A. Ab Kadir, N. Misron, and M. A. Mohd Radzi, “Static eccentricity fault recognition in three-phase line start permanent magnet synchronous motor using finite element method,” *Mathematical Problems in Engineering*, vol. 2014, 2014.

[23] M. Karami, N. Mariun, M. R. Mehrjou, M. Z. A. Ab Kadir, N. Misron, and M. A. Mohd Radzi, “Diagnosis of static eccentricity fault in line start permanent magnet synchronous motor,” in *IEEE International Conference on Power and Energy, PECon*, 2014, pp. 83–86.

[24] M. Moustafa and M. Sedky, “Diagnosis of static , dynamic and mixed eccentricity in line start permanent magnet synchronous motor by using FEM,” *International Journal of Electrical, Robotics, Electronics and Communications Engineering*, vol. 8, no. 1, pp. 29–34, 2014.

[25] T. A. Liop, *Analysis of Synchronous Machines*. CRC Press, 2012.

[26] B. M. Ebrahimi, J. Faiz, M. Javan-Roshtkhari, and A. Zargham Nejhad, “Static eccentricity fault diagnosis in permanent magnet synchronous motor using time stepping finite element method,” *IEEE Transactions on Magnetics*, vol. 44, no. 11, pp. 4297–4300, 2008.

[27] B. M. Ebrahimi, J. Faiz, and M. J. Roshtkhari, “Static-, dynamic-, and mixed-eccentricity fault diagnoses in permanent-magnet synchronous motors,” *IEEE Transactions on Industrial Electronics*, vol. 56, no. 11, pp. 4727–4739, 2009.

[28] J. Faiz, B. M. Ebrahim, B. Akin, and H. A. Toliyat, “Finite-element transient analysis of induction motors under mixed eccentricity fault,” *IEEE Transactions on*

Magnetics, vol. 44, no. 1, pp. 66–74, 2008.

[29] T. Goktas, M. Zafarani, and B. Akin, “Discernment of broken magnet and static eccentricity faults in permanent magnet synchronous motors,” *IEEE Transactions on Energy Conversion*, pp. 1–10, 2016.

[30] T. Lubin, T. Hamiti, H. Razik, and A. Rezzoug, “Comparison between finite-element analysis and winding function theory for inductances and torque calculation of a synchronous reluctance machine,” *IEEE Transactions on Magnetics*, vol. 43, no. 8, pp. 3406–3410, 2007.

[31] J. Faiz and I. Tabatabaei, “Extension of winding function theory for nonuniform air gap in electric machinery,” *IEEE Transactions on Magnetics*, vol. 38, no. 6, pp. 3654–3657, 2002.

[32] I. Biomedica and E. D. Telecomu-, “Cririical review of the modified winding function theory,” *Progress In Electromagnetics Research*, vol. 133, no. 1, pp. 53–89, 2013.

[33] H. A. Toliyat, S. Bhattacharya, M. M. Rahimian, and T. A. Lipo, “Transient analysis of induction machines under internal faluts using winding functions,” in *3rd Int. Conf. Electrical Rotating Machines-ELROMA*, 1992.

[34] H. A. Toliyat and T. A. Lip, “Transient analysis of cage induction machines under stator, rotor bar and end ring faults,” *IEEE Transactions on Energy Conversion*, vol. 10, no. 2, pp. 241–247, 1995.

[35] S. Nandi, S. Ahmed, and H. A. Toliyat, “Detection of rotor slot and other

eccentricity related harmonics in a three phase induction motor with different rotor cages," *IEEE Transactions on Energy Conversion*, vol. 16, no. 3, pp. 253–260, 2001.

[36] S. Hamdani, O. Touhami, R. Ibtiouen, and M. Hasni, "Analytical evaluation of inductances for induction machine with dynamic eccentricity using MWFA and FE methods," in *IEEE International Symposium on Diagnostics for Electric Machines, Power Electronics and Drives (SDEMPED)*, 2013, pp. 420–427.

[37] G. Bossio, C. De Angelo, J. Solsona, G. O. Garca, and M. I. Valla, "A model for induction motors with non-uniform air-gap," *Latin American Applied Research*, vol. 35, no. 2, pp. 77–82, 2005.

[38] G. Joksimovic, "Dynamic simulation of cage induction machine with air gap eccentricity," in *IEE Proceedings-Electric Power Applications*, 2005.

[39] M. Sahraoui, A. Ghoggal, S. E. Zouzou, and M. E. Benbouzid, "Dynamic eccentricity in squirrel cage induction motors - Simulation and analytical study of its spectral signatures on stator currents," *ELSEVIER, Simulation Modelling Practice and Theory*, vol. 16, no. 9, pp. 1503–1513, 2008.

[40] S. Nandi, R. M. Bharadwaj, and H. A. Toliyat, "Mixed eccentricity in three phase induction machines: analysis, simulation and experiments," in *IEEE Conference Record of the Industry Applications*, 2002, no. 3, pp. 1525–1532.

[41] E. Ghazvini, J. Faiz, I. Tabatabaei-Ardekani, and A. Shirani, "Modeling and dynamic simulation of induction machine under mixed eccentricity conditions using winding function," in *CIGRÉ Session*, 2004.

[42] H. Hooshmandi, M. Ebrahimi, A. Davoudi, and A. Pouramin, "Analytical derivation of induction motors inductances under eccentricity conditions," *Progress In Electromagnetics Research B*, vol. 60, no. May, pp. 95–110, 2014.

[43] L. W. L. Wu, T. G. Habetler, and R. G. Harley, "Separating load torque oscillation and rotor faults in stator current based-induction motor condition monitoring," in *IEEE International Conference on Electric Machines and Drives*, 2005, no. May, pp. 1889–1894.

[44] V. M. Sundaram and H. A. Toliyat, "Diagnosis and isolation of air-gap eccentricities in closed-loop controlled doubly-fed induction generators," in *IEEE International Electric Machines and Drives Conference, IEMDC*, 2011, pp. 1064–1069.

[45] G. M. Joksimović, M. D. Durović, J. Penman, and N. Arthur, "Dynamic simulation of dynamic eccentricity in induction machines - winding function approach," *IEEE Transactions on Energy Conversion*, vol. 15, no. 2, pp. 143–148, 2000.

[46] H. Akbari, "An analytical method for computation of induction machine inductance under rotor misalignment fault," *Canadian Journal of Pure and Applied Sciences*, vol. 9, no. 1, pp. 3325–3332, 2015.

[47] X. Li and N. Subhasis, "Performance analysis of a 3-phase induction machine with inclined static eccentricity," in *IEEE International Conference on Electric Machines and Drives*, 2005, pp. 1606–1613.

[48] H. R. Akbari, S. Sadeghi, and A. H. Isfahani, "Calculation of inductances of induction machines under axial non-uniformity conditions," *Journal of Electrical Engineering*, vol. 60, no. 3, pp. 149–154, 2009.

[49] Q. Lv, X. Bao, Y. He, Y. Fang, and X. Cheng, “Inductances evaluation of a squirrel-Cage induction motor with curved dynamic Eccentricity,” *Journal of Electrical Engineering Technology*, vol. 9, no. 5, pp. 1623–1631, 2014.

[50] A. Ghoggal, S. E. Zouzou, H. Razik, M. Sahraoui, and A. Khezzar, “An improved model of induction motors for diagnosis purposes - Slot skewing effect and air-gap eccentricity faults,” *ELSEVIER, Energy Conversion and Management*, vol. 50, no. 5, pp. 1336–1347, 2009.

[51] M. Drif and A. J. M. Cardoso, “Airgap-eccentricity fault diagnosis, in three-phase induction motors, by the complex apparent power signature analysis,” *IEEE Transactions on Industrial Electronics*, vol. 55, no. 3, pp. 1404–1410, 2008.

[52] A. Ibrahim and M. Marei, “Modeling of induction motor based on winding function theory to study motor under stator/rotor internal faults,” in *IEEE proceedings, MEPCON*, 2010, no. 1, pp. 494–500.

[53] M. Jannati, T. Sutikno, N. Idris, and M. Abdul-Aziz, “Modeling of balanced and unbalanced three-phase induction motor under balanced and unbalanced supply based on winding function method,” *International Journal of Electrical and Computer Engineering (IJECE)*, vol. 5, no. 4, pp. 644–655, 2015.

[54] B. M. Ebrahimi, M. Etemadrezaei, and J. Faiz, “Dynamic eccentricity fault diagnosis in round rotor synchronous motors,” *ELSEVIER, Energy Conversion and Management*, vol. 52, no. 5, pp. 2092–2097, 2011.

[55] B. Ebrahimi, F. Jawad, E. Mohammad, and B. Mojtaba, “Eccentricity fault identification in round rotor synchronous motors considering load variation,” no. 5,

pp. 288–292, 2011.

[56] N. a. Al-Nuaim and H. Toliyat, “A novel method for modeling dynamic air-gap eccentricity in synchronous machines based on modified winding function theory,” *IEEE Transactions on Energy Conversion*, vol. 13, no. 2, pp. 156–162, 1998.

[57] W. le Roux, R. G. Harley, and T. G. Habetler, “Detecting rotor faults in low power permanent magnet synchronous machines,” *IEEE Transactions on Power Electronics*, vol. 22, no. 1, pp. 322–328, Jan. 2007.

[58] B. Wymeersch, F. De Belie, C. B. Rasmussen, F. Jensen, and L. Vandevelde, “Mutual-inductance modelling in line-start permanent-magnet synchronous machines based on winding-function theory,” in *IEEE International Electric Machines and Drives Conference, IEMDC*, 2013, pp. 607–611.

[59] A. Tessarolo, “Accurate computation of multiphase synchronous machine inductances based on winding function theory,” *IEEE Transactions on Energy Conversion*, vol. 27, no. 4, pp. 895–904, 2012.

[60] J. Hong, S. Bin Lee, C. Kral, and A. Haumer, “Detection of airgap eccentricity for permanent magnet synchronous motors based on the d -axis inductance,” *IEEE transaction on Power Electronics*, vol. 27, no. 5, pp. 2605–2612, 2012.

[61] J. Hong, S. Park, D. Hyun, T. J. Kang, S. Bin Lee, C. Kral, and A. Haumer, “Detection and classification of rotor demagnetization and eccentricity faults for PM synchronous motors,” *IEEE Transactions on Industry Applications*, vol. 48, no. 3, pp. 923–932, 2012.

[62] P. Huang, S. Mao, and M. Tsai, “Investigation of inductance variation with rotor eccentricity for permanent magnet motors,” in *IEEE, International Conference on ICEMS*, 2010.

[63] A. Macdonald and G. M. Burt, “Magnetic equivalent circuit modeling for interior permanent magnet synchronous machine under eccentricity fault,” in *nternational Universities' Power Engineering Conference (UPEC)*, 2013, pp. 1–6.

[64] S. Nandi, T. C. Ilamparithi, S. Bin Lee, and D. Hyun, “Detection of eccentricity faults in induction machines based on nameplate parameters,” *IEEE Transactions on Industrial Electronics,* vol. 58, no. 5, pp. 1673–1683, 2011.

[65] V. N. Ghate and S. V. Dudul, “Cascade neural-network-based fault classifier for three-phase induction motor,” *IEEE Transactions on Industrial Electronics,* vol. 58, no. 5, pp. 1555–1563, 2011.

[66] X. Huang, T. G. Habetler, and R. G. Harley, “Detection of rotor eccentricity faults in a closed-loop drive-connected induction motor using an artificial neural network,” *IEEE Transactions on Power Electronics*, vol. 22, no. 4, pp. 1552–1559, 2007.

[67] M. Seera and C. P. Lim, “Online motor fault detection and diagnosis using a hybrid FMM-CART model,” *IEEE Transactions on Neural Networks and Learning Systems,* vol. 25, no. 4, pp. 806–812, 2014.

[68] M. Seera, C. P. Lim, D. Ishak, and H. Singh, “Fault Detection and Diagnosis of Induction Motors Using Motor Current Signature Analysis and a Hybrid FMM – CART Model,” *IEEE Transaction on Neural Networks and Learning Systems,* vol.

23, no. 1, pp. 97–108, 2012.

[69] C. Ong, *Dynamic simulation of electric machinery using matlab-simulink,* 1st ed. Prentice Hall PTR, 1998.

[70] P. C. Krause, O. Wasynczuk, and S. D. Sundhoff, *Analysis of electrical machinery and drive systems,* 2nd ed. Wily-IEEE Press, 2002.

[71] I. Tabatabaei, J. Faiz, and H. Lesani, "Modeling and Simulation of a Salient-Pole Using Modified Winding Function Theory," *IEEE Transactions on Magnetics*, vol. 40, no. 3, pp. 1550–1555, 2004.

[72] J. Faiz, B. M. Ebrahimi, M. Valavi, and H. A. Toliyat, "Mixed eccentricity fault diagnosis in salient-pole synchronous generator using modified winding function method," *Progress In Electromagnetics Research B*, vol. 11, pp. 155–172, 2009.

[73] X. Tang and X. Wang, "Calculation of magnets ' Average operating point during the starting process of line-start permanent magnet synchronous motor," pp. 2147–2150, 2014.

[74] R. ul Rojas, *Neural networks, a systematic introduction*. Springer, 1996.

[75] B. Krose and P. Van Der Smagt, *Introduction to neural networks*. University of Amsterdam, 1996.

[76] R. May, G. Dandy, and H. Maier, "Review of input variable selection methods for artificial neural networks," *Artificial Neural Networks - Methodological Advances and Biomedical Applications*, vol. 2, no. August 2016, pp. 362–376, 2011.

[77] B. Chebel-Morello, S. Malinowski, and H. Senoussi, "Feature selection for fault

detection systems: application to the Tennessee Eastman process," *Applied Intelligence, Springer Verlag (Germany)*, vol. 44, no. 1, pp. 111–122, 2016.

[78] G. P. Zhang, "Neural networks for classification: a survey," *IEEE Transactions on Systems, Man and Cybernetics*, vol. 30, no. 4, pp. 451–462, 2000.

[79] M. R. Mehrjou, N. Mariun, N. Misron, and M. A. M. Radzi, "Analysis of statistical features based on start-up current envelope for broken rotor bar fault detection in line start permanent magnet synchronous motor," *Electrical Engineering*, 2016.

APPENDIX : MOTOR PARAMETERS

A.1 Dimensions of LSPMS Motor

The detailed geometry model of the LSPMS motor and the winding diagram are shown below:

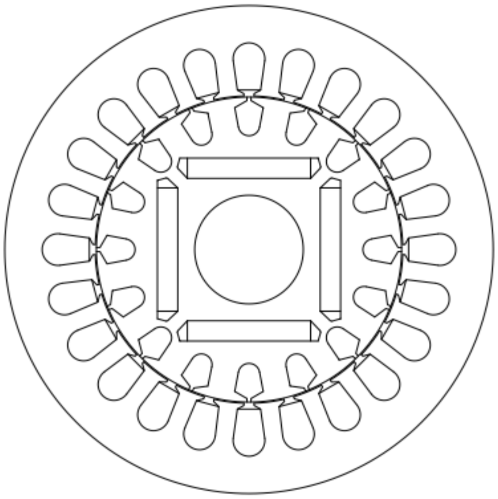

Figure A. 1: Geometry model of LSPMS motor.

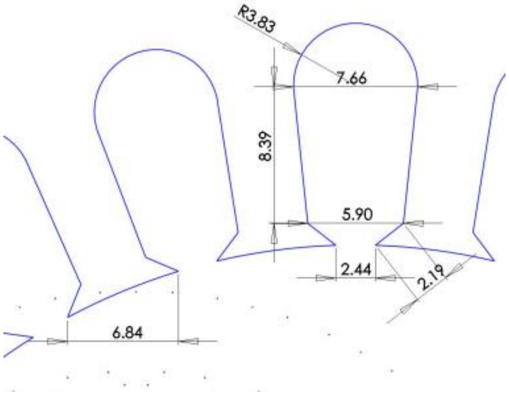

Figure A. 2: Dimensions of the stator slot.

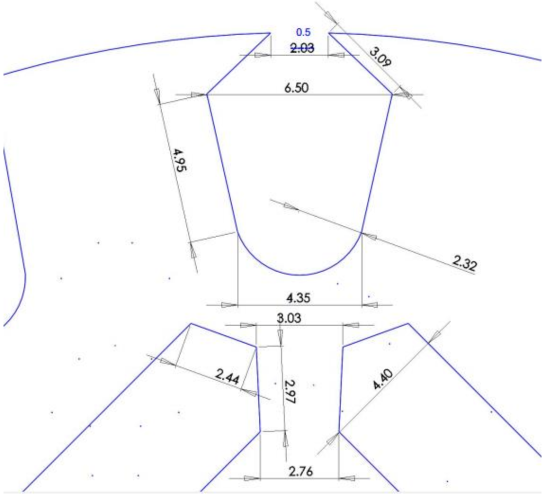

Figure A. 3: Dimensions of the rotor slot

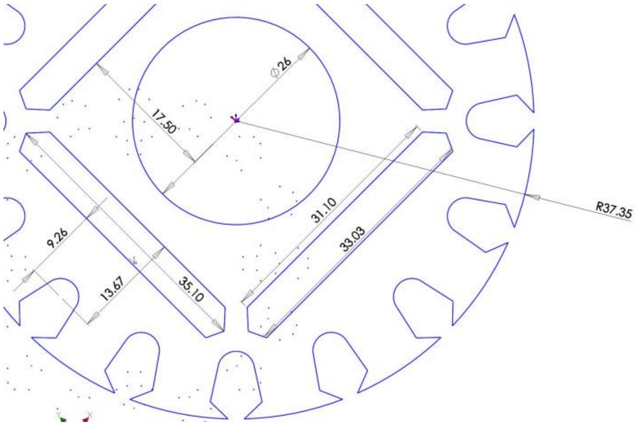

Figure A. 4: Dimensions of the rotor and the magnets.

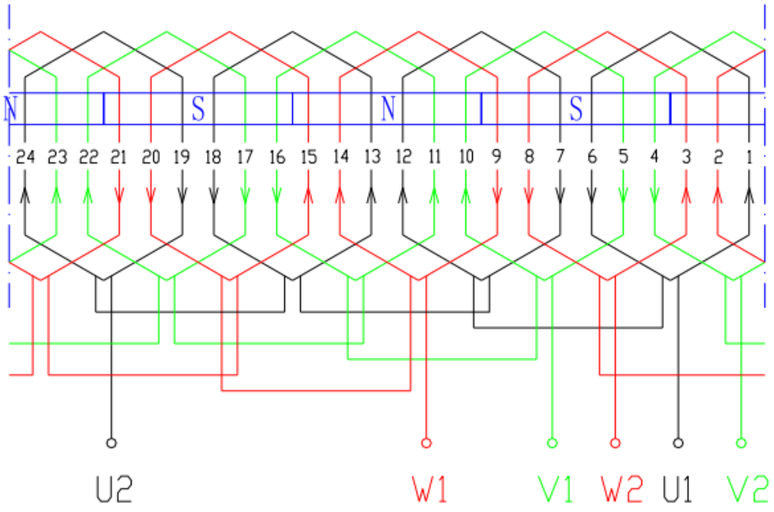

Figure A. 5: Stator winding diagram.

A.2 Magnets Datasheet

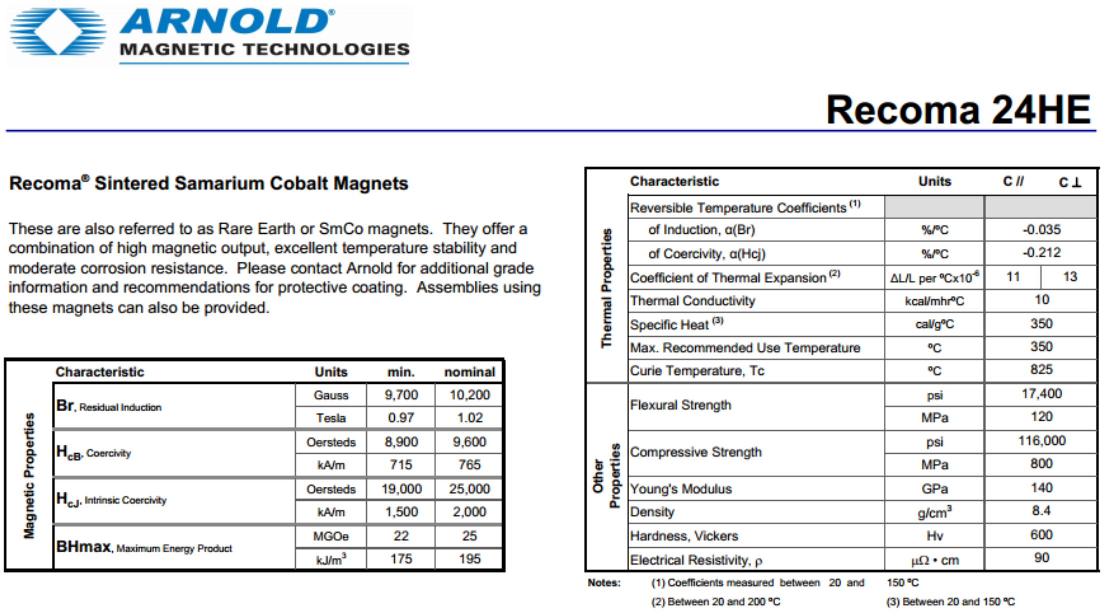

ARNOLD
MAGNETIC TECHNOLOGIES

Recoma 24HE

Recoma® Sintered Samarium Cobalt Magnets

These are also referred to as Rare Earth or SmCo magnets. They offer a combination of high magnetic output, excellent temperature stability and moderate corrosion resistance. Please contact Arnold for additional grade information and recommendations for protective coating. Assemblies using these magnets can also be provided.

	Characteristic	Units	min.	nominal
Magnetic Properties	**Br**, Residual Induction	Gauss	9,700	10,200
		Tesla	0.97	1.02
	H_{cB}, Coercivity	Oersteds	8,900	9,600
		kA/m	715	765
	H_{cJ}, Intrinsic Coercivity	Oersteds	19,000	25,000
		kA/m	1,500	2,000
	BHmax, Maximum Energy Product	MGOe	22	25
		kJ/m³	175	195

	Characteristic	Units	C //	C ⊥
Thermal Properties	Reversible Temperature Coefficients (1)			
	of Induction, α(Br)	%/°C	-0.035	
	of Coercivity, α(Hcj)	%/°C	-0.212	
	Coefficient of Thermal Expansion (2)	ΔL/L per °Cx10⁻⁶	11	13
	Thermal Conductivity	kcal/mhr°C	10	
	Specific Heat (3)	cal/g°C	350	
	Max. Recommended Use Temperature	°C	350	
	Curie Temperature, Tc	°C	825	
Other Properties	Flexural Strength	psi	17,400	
		MPa	120	
	Compressive Strength	psi	116,000	
		MPa	800	
	Young's Modulus	GPa	140	
	Density	g/cm³	8.4	
	Hardness, Vickers	Hv	600	
	Electrical Resistivity, ρ	μΩ • cm	90	

Notes: (1) Coefficients measured between 20 and 150 °C
(2) Between 20 and 200 °C
(3) Between 20 and 150 °C

A.3 Motor Parameters

Table A.1: LSPMS motor parameters.

Parameter	**Value**
Rated power (W)	750
Rated Voltage (V)	415
Stator phase resistance (Ohm)	19.15
Stator leakage inductance (mH)	0.001
Number of poles	4
Frequency (Hz)	50
Air-gap length (mm)	0.3
Outer/inner stator diameter (mm)	120/75
Number of stator/rotor slots	24/16
Axial length of stator core (mm)	72
Number of turns per slot	139
Height of stator yoke (mm)	45
Height of stator/rotor slots (mm)	13/9.5
Magnet material	Recoma-24HE
Remanent of magnet (T)	1.02
Equivalent rotor resistance (ohm)	1.3295e-3
Inertia constant	0.094

A.4 JMAG Conditions

Several conditions should be assigned in JMAG^{TM}, such as motion rotation, rotation periodic boundary, torque, FEM coil, step control, full model conversion, circuit settings, nonlinear calculations, and rational motion. The motion and FEM conditions will be discussed here.

The motion condition will specify how the motor will rotate. In an actual motor, the rotor rotates by excitation. However, in JMAG^{TM}, the motion condition should be specified to rotate the rotor. There are many rotation conditions that could be used; in our model, the rotation setting is ruled by equation of motion as the one discussed in the mathematical model. By considering this option, the following data is assigned as shown in Table A.1. The torque multiplier is equal to one, which means that the original torque has no scaled value. In addition, the friction is ignored to accelerate the computational calculation. The motor inertia will be calculated automatically at the beginning of the simulation from the motor geometry.

Table A.2: The rotational motion conditions.

Parameter	Value
Torque multiplier	1
Friction coefficient	0
Motor inertia	Automatic

The FEM condition is set to link the FEM coils from the geometry model and the FEM coils in the circuit model. The FEM coil condition is set for each phase in the three-phase system. Also, the current flow direction is set for each coil. An example is shown below:

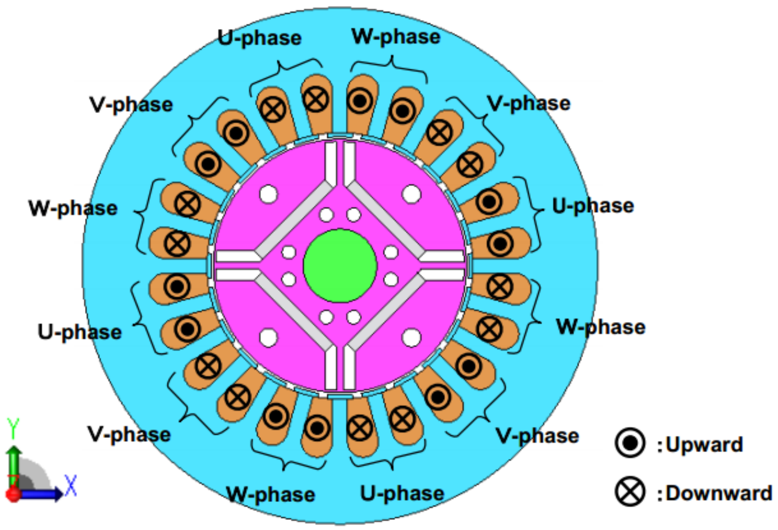

Figure A. 6: Current directions of the FEM coils

VITAE

Name: Ibrahem Mahmoud Hussein

Date of Birth: 6 Jun 1990

Nationality: Palestinian

Email: imhusseein@gmail.com

Address 1: Old-city, Jerusalem, Palestine, T.L: +972 526574084, P.O.BOX: 66554

Address 2: KFUPM, Al-Khobar, KSA, T.L: +966 501366314

Academic Background:

- Bachelor of Science in Electrical Engineering from Birzeit University, Jan 2013.
- Receive a scholarship from King Fahd University of Petroleum and Minerals (KFUPM) in 2014 to study the MS degree in Electrical Engineering.
- Master of Science in Electrical Engineering from KFUPM, Jan 2017.

Work Experience:

- **Electrical Engineer at All Control Company (ACC)**

May 2014 - Aug 2014
Electrical Engineer
The company is responsible to the main water pump stations located in West-bank and some in Jerusalem. Among the tasks which we are performing: Regular electrical maintenance of pump stations (Transformers, switchgears, motor drives, pumps, etc.) and assuring the reliability of water transmission.

- **Electrical Engineer at Safety Technology**

December 2013 – May 2014
Technical Support Electrical Engineer
- Design and Installation of fire alarm systems (Secutron and Telefire Brands).

- Design and Installation of burglar alarm systems (Hunter pro and Crow Brands).
- Design and Installation of CCTV systems (Hikvision and Honeywell Brands).
- Design and Installation of General network systems (Cisco, HP and 3M Brands).
- Design and Installation for general low voltage systems such as: Access control systems, access management's, public address and evacuation systems, FACP's programming. Website: www.safetytech.ps

- **Technical Engineer at Afcon Control and Automation.Ltd**

March 2013 - December 2013

Fire Alarm Systems Installation and Maintenance Engineer.

In this period, I carried out duties on designing and planning for installing fire alarm systems (Simplex Brand).

- **Power Engineer at JDECO**

July 2012 - September 2012

Trainee Electrical Power Engineer,

Jerusalem District Electricity Company (JDECO), Jerusalem - Main office.

In this period, I carried out duties on:

Electrical power systems distribution process and systems control, power systems protection, Scada system interface, electrical inspectorate, participated in several industrial visits with local students and engineers (I had the opportunities to know more about electrical systems and methods of generation), analyst and making decisions, consumer services and electrical cost estimation process.